UNIVERSITÉ DE GENÈVE
Département de physique nucléaire et corpusculaire

FACULTÉ DES SCIENCES
Professeur Allan G. Clark

Search for WW and WZ production in lepton, neutrino plus jets final states at CDF Run II

and

Silicon Module Production and Detector Control System for the ATLAS SemiConductor Tracker

THÈSE

présentée à la Faculté des sciences de l'Université de Genève
pour obtenir le grade de Docteur ès sciences, mention physique

par

Anna Sfyrla

de Grèce

Thèse N° 3956

GENÈVE
Atelier de reproduction de la Section de physique
2008

UNIVERSITÉ DE GENÈVE

FACULTÉ DES SCIENCES

Doctorat ès sciences
mention physique

Thèse de *Madame Anna SFYRLA*

intitulée :

"Search for *WW* and *WZ* Production in Lepton, Neutrino Plus Jets Final States at CDF Run II
and
Silicon Module Production and Detector Control System for the ATLAS SemiConductor Tracker"

La Faculté des sciences, sur le préavis de Messieurs A. G. CLARK, professeur ordinaire et directeur de thèse (Département de physique nucléaire et corpusculaire), M. POHL, professeur ordinaire (Département de physique nucléaire et corpusculaire), P. RENTON, professeur (University of Oxford, Department of Physics, Oxford, United Kingdom), autorise l'impression de la présente thèse, sans exprimer d'opinion sur les propositions qui y sont énoncées.

Genève, le 10 mars 2008

Thèse - 3956 -

Le Doyen, Jean-Marc TRISCONE

N.B.- La thèse doit porter la déclaration précédente et remplir les conditions énumérées dans les "Informations relatives aux thèses de doctorat à l'Université de Genève".

Nombre d'exemplaires à livrer par colis séparé à la Faculté : - 7 -

Abstract

In the first part of this work, we present a search for WW and WZ production in charged lepton, neutrino plus jets final states produced in $p\bar{p}$ collisions with $\sqrt{s} = 1.96$ TeV at the Fermilab Tevatron, using 1.2 fb^{-1} of data accumulated with the CDF II detector. This channel is yet to be observed in hadron colliders due to the large single W plus jets background. However, this decay mode has a much larger branching fraction than the cleaner fully leptonic mode making it more sensitive to anomalous triple gauge couplings that manifest themselves at higher transverse W momentum. Because the final state is topologically similar to associated production of a $Higgs$ boson with a W, the techniques developed in this analysis are also applicable in that search.

An Artificial Neural Network has been used for the event selection optimization. The theoretical prediction for the cross section is

$$\sigma^{theory}_{WW/WZ} \times Br(W \to \ell\nu; W/Z \to jj) = 2.09 \pm 0.14 \text{ pb}$$

We measured

$$N_{Signal} = 410 \pm 212(stat) \pm 102(sys) \text{ signal events}$$

that correspond to a cross section

$$\sigma_{WW/WZ} \times Br(W \to \ell\nu; W/Z \to jj) = 1.47 \pm 0.77(stat) \pm 0.38(sys) \text{ pb}$$

The 95% CL upper limit to the cross section is estimated to be

$$\sigma \times Br(W \to \ell\nu; W/Z \to jj) < 2.88 \text{ pb}$$

The second part of the present work is technical and concerns the ATLAS SemiConductor Tracker (SCT) assembly phase. Although technical, the work in the SCT assembly phase is of prime importance for the good performance of the detector during data taking.

The production at the University of Geneva of approximately one third of the silicon microstrip end-cap modules is presented. This collaborative effort of the university of Geneva group that lasted two years, resulted in 655 produced modules, 97% of which were good modules, constructed within the mechanical and electrical specifications and delivered in the SCT collaboration for assembly on the end-cap disks.

The SCT end-caps and barrels consist of 4088 silicon modules, with a total of 6.3 million readout channels. The coherent and safe operation of the SCT during commissioning and subsequent operation is the essential task of the Detector Control System (DCS). The main building blocks of the DCS are the cooling system, the power supplies and the environmental system. The DCS has been initially developed for the SCT assembly phase and this system is described in the present work. Particular emphasis is given in the environmental hardware and software components, that were my major contributions. Results from the DCS testing during the assembly phase are also reported.

Résumé

Ce travail de thèse est composé de deux parties. La première présente un travail de recherche sur la production de paires de bosons WW et WZ, menée à l'expérience CDF II. La seconde est de nature plus technique et concerne la phase d'assemblage du trajectographe à semi-conducteur (SCT, Semi-Conductor Tracker) de l'expérience ATLAS.

Les paires WW et WZ sont recherchés dans les états finaux de lepton, neutrino et jets. Les données sont récoltées avec le détecteur CDF II au Tevatron de Fermilab, un collisionneur proton-antiproton avec une énergie au centre de masse de $\sqrt{s} = 1.96$ TeV. L'ensemble des données correspond à une luminosité intégrée de 1.2 fb^{-1}. Ce canal n'a pas encore été observé dans un collisionneur hadronique en raison du bruit de fond très important de la production de W+jets. Cepedant pour la production de paires de bosons, le taux de branchement vers les états finaux semi-leptoniques ($\ell + \nu$+jets) est beaucoup plus important que celui vers les états finaux purement leptoniques et par là ce canal est plus sensible aux triples couplages de jauge, qui se manifestent à des impulsions transversales importantes du W. Enfin, cet état final a une topologie similaire à la production associée du boson de Higgs avec un W et on peut donc utiliser les techniques conçues pour cette analyse au cas présent.

Un réseau neuronal artificiel est utilisé pour la sélection des données. La prédiction théorique pour la section efficace est de

$$\sigma^{théorie}_{WW/WZ} \times Br(W \to \ell\nu; W/Z \to jj) = 2.09 \pm 0.14 \text{ pb}$$

Dans les données, le nombre d'événements retenus est de

$$N_{Signal} = 410 \pm 212(stat) \pm 102(sys)$$

qui correspondent à une section efficace mesurée à

$$\sigma_{WW/WZ} \times Br(W \to \ell\nu; W/Z \to jj) = 1.47 \pm 0.77(stat) \pm 0.38(sys) \text{ pb}$$

Ce résultat fixe une limite supérieure à la section efficace (95% CL) de

$$\sigma \times Br(W \to \ell\nu; W/Z \to jj) < 2.88 \text{ pb}$$

Le travail effectué pendant la phase d'assemblage du SCT revêt une importance capitale dans la performance du détecteur pendant la prise de données. Cette deuxième partie de la thèse présente la production, à l'Université de Genève, d'environ un tiers des modules à micropistes en silicium destinés aux bouchons du SCT. Cette contribution à la collaboration a duré deux ans et conduit à la production de 655 modules, dont 97% construits selon les spécifications électriques et mécaniques. Ces modules ont été livrés au groupe SCT pour l'assemblage.

Les bouchons et les tonneaux du SCT sont composés de 4088 modules en silicium, pour un total de 6.3 millions de canaux. L'assurance d'un fonctionnement cohérent et sûr du SCT pendant la mise en service et l'activité subséquente est la tâche essentielle du système de contrôle du détecteur (Detector Control System, DCS). Le DCS comprend les systèmes de refroidissement, d'alimentation électrique et de contrôle environnemental. Le DCS a initialement été développé pour la phase d'assemblage du SCT, et c'est cette version du système qui est décrite dans cette thèse. L'accent est mis sur le système de contrôle environnemental, à la fois dans les aspects matériels et logiciels, qui a fait l'objet de mes contributions majeures. Les résultats des test du DCS conduits pendant l'assemblage du SCT sont également présentés.

Contents

Chapter 1

Introduction

The Standard Model, the theory that describes the known particles and the way they interact, has proven very successful. It has been stringently tested experimentally, and its predictions involving the fundamental building blocks of matter, the quarks, the leptons, and the vector bosons, have been confirmed. However, some basic questions of the Standard Model have yet to be answered: What is the origin of the fundamental particles?; Why are there so many kinds of particles?; How do the particles get their masses?; etc. According to the Standard Model, all particles acquire their masses through their interaction with the so-called Higgs field. The existence of this field implies the existence of a new particle, the Higgs boson, but its mass is not predicted by the theory. This particle has not yet been detected experimentally, and its discovery would confirm a very important prediction of the Standard Model.

The fundamental principles of nature can be studied using a powerful tool that can probe the tiny particles and test the forces that affect them: the particle accelerator. Modern accelerators are many kilometers in length or circumference, and accelerate protons and electrons, and their antiparticles, leading them to collisions. The collisions produce new particles that are studied by surrounding the collision points with detectors, large devices that record what traverses them.

The current highest energy accelerator, the Tevatron in the USA, is colliding protons and antiprotons at a center of mass energy of 1.96 TeV. The collision products are detected by two experiments (CDF and DØ) installed in the two collision points of the 6 km circumference of the Tevatron accelerator. They provide invaluable information for the deeper understanding of the particles and their interactions, and they are seeking the Higgs boson signature.

In 2008, the Large Hadron Collider (LHC), an accelerator at CERN, in Switzerland, will commence in collisions of protons at unprecedented energies. Its results will either support or refute the Standard Model's prediction of the existence of the Higgs boson and will possibly give hints for new physics, beyond the Standard Model predictions. The ATLAS detector at the LHC is the largest of the detectors that will record the details of the proton collisions.

In the picture of an accelerator currently colliding particles and producing interesting data, and another that is getting ready to operate soon, the present work is divided in two parts.

In the first part, a search for WW and WZ production in charged lepton, neutrino plus jets final states is presented. Data produced in $p\bar{p}$ collisions with $\sqrt{s} = 1.96$ TeV at the Fermilab Tevatron and accumulated with the CDF II detector are analyzed. This channel is yet to be observed in hadron colliders due to the large single W plus jets background. However, this decay mode has a much larger branching fraction than the cleaner fully leptonic mode making it more sensitive to anomalous triple gauge couplings that manifest themselves at higher transverse W momentum. Because the final state is topologically similar to associated production of a $Higgs$ boson with a W, the techniques developed in this analysis are also applicable in that search. In order to optimized the event selection for this search, an Artificial Neural Network has been used.

The theoretical motivations for this search and a summary of the current knowledge are given in Chapter 2. In Chapter 3, the Fermilab accelerator complex and the CDF detector are briefly described, with emphasis given in the components of particular interest for this analysis. The data are collected by a data acquisition and trigger system, which are also described in Chapter 3. The sophisticated algorithms used to translate the data into the physical objects and the event selection of the signatures of interest are summarized in Chapter 4. The event selection is controlled using Monte Carlo and the data to Monte Carlo agreement is verified in control regions, as explained in Chapter 5. In order to optimize the event selection, an Artificial Neural Network is used. The invariant mass of the events that pass a Neural Network cut is parameterized and fed into a likehood fitter where the signal fraction is a free parameter. The analysis methodology is given in detail in Chapter 6. In Chapter 7, the analysis results using 1.2 fb^{-1} are presented, together with the

statistical and systematic uncertainties. The future perspectives of this analysis are finally given in Chapter 8.

The second part of the present work is technical and concerns the ATLAS Semi-Conductor Tracker (SCT) assembly phase. Although technical, the work in the SCT assembly phase is of prime importance for the good performance of the detector during data taking.

The ATLAS detector is initially briefly described in Chapter 9. A more detailed description of the SCT, together with the properties of the silicon modules, the SCT building blocks, are reported and the end-cap silicon module production at the University of Geneva is summarized in Chapter 10. Finally, in Chapter 11, the Detector Control System (DCS) for the SCT assembly phase is described, with emphasis given in the environmental software and hardware components and the DCS testing during the assembly phase.

Part I

Search for WW and WZ production in lepton, neutrino plus jets final states at CDF

Chapter 2

Theoretical Overview and Motivations

2.1 The Standard Model of Particle Physics

Towards the birth of the Standard Model

One of the biggest questions that humans posed to themselves is how the world has been created and what it is made of.

The first half of the twentieth century was marked by revolutionary theories and experimental observations that resulted in a deeper understanding of what the matter is made of. A new view of nature was given by the quantum mechanics and the theory of relativity. While the reconciliation of special relativity and quantum mechanics kept on being a central issue for several decades, experimental observations led to significant discoveries that boosted the theoretical evolution. The uncertainty principle is formulated; the neutrino is introduced; positively charged particles are introduced (with the positron being the first one); the weak interaction, the first theory to explicitly use neutrinos, is introduced; the neutron, the muon, the pion, the kaon are discovered. When the Brookhaven Cosmotron, a 1.3 GeV proton accelator started operating, in 1952, a particle explosion came to enlarge the list of known particles (mesons and baryons). The charged heavy bosons W^+ and W^- were introduced as the mediators of the weak interaction and a few years later, a new class of theories, called *gauge theories*, was developed and the unification of the weak and the electromagnetic interactions was proposed.

By the mid-1960's, physicists realized that their previous understanding, where

all matter is composed of protons, neutrons and electrons, was insufficient to explain the myriad new particles being discovered. The revolutionary idea of quarks, introduced by *Gell-Mann* and *Zweig*, solves the problem. Initially three quarks are suggested, however in order for the leptonic pattern to be followed, a fourth quark has been added. Quarks and leptons are now seen as the elementary particles of matter, formulated in two generations. The quark model is accepted very slowly given that there is no experimental observation till the end of 1960's, when the first indication for quarks comes from an electron scattering experiment at SLAC. These studies also showed that the quarks only carried a fraction of the nucleon momentum and the rest was carried by what we call gluons. The Standard Model is now starting to get formulated, with the quarks and gluons being a part of it. A quantum field theory of the strong interactions is introduced and is called *Quantum ChromoDynamics* (QCD), similarly to the *Quantum ElectroDynamics* (QED). The view of physics now called *Standard Model* was for the first time presented in a single report in 1974. Since then, the Standard Model has been extended, and all (but one, the Higgs boson) of the particles that the Standard Model predicts have thus far been discovered experimentally [1].

The forces and the particles

The Standard Model describes the interplay of three forces[1], electromagnetic, weak and strong, and 12 elementary particles and their corresponding antiparticles. Each of the three forces is mediated by the exchange of particles (the photon, for the electromagnetic force, the W or Z boson for the weak and the gluon for the strong) (Table 2.1).

Force	Particle	Mass (GeV/c^2)
Electromagnetic	photon	0
Weak	W^+,W^-	80.403 ± 0.029 [2]
	Z^0	91.1876 ± 0.0021 [2]
Strong	gluon	0

Table 2.1: The gauge bosons of the Standard Model.

The elementary particles, leptons and quarks, are lined up into three *generations*, according to their mass hierarchy (Table 2.2):

[1]The gravity is not included in the Standard Model, but its effects are negligible at present energies.

$$leptons: \begin{pmatrix} e^- \\ \nu_e \end{pmatrix} \begin{pmatrix} \mu^- \\ \nu_\mu \end{pmatrix} \begin{pmatrix} \tau^- \\ \nu_\tau \end{pmatrix}$$

$$quarks: \begin{pmatrix} u \\ d \end{pmatrix} \begin{pmatrix} c \\ s \end{pmatrix} \begin{pmatrix} t \\ b \end{pmatrix} \begin{bmatrix} Q = 2/3 \\ Q = -1/3 \end{bmatrix}$$

Leptons	Mass (MeV/c^2)
e^-	$0.51099892 \pm 0.00000004$
ν_e	$< 2 \cdot 10^{-3}$ $(tritium\ decay)$
μ^-	105.658369 ± 0.000009
ν_μ	$< 0.19\ at\ 90\%CL$
τ^-	$1776.99^{+0.29}_{-0.26}$
ν_τ	$< 18.2\ at\ 95\%CL$
Quarks	**Mass (GeV/c^2)**
u	$1.5\ to\ 3.0 \cdot 10^{-3}$
d	$3\ to\ 7 \cdot 10^{-3}$
s	$95 \pm 25 \cdot 10^{-3}$
c	1.25 ± 0.09
b	4.70 ± 0.7
t	174.2 ± 3.3

Table 2.2: The masses of the elementary particles in the Standard Model. The measurements are reported from Reference [2]. Why these are the masses of the fermions and why the mass of the top quark is so different from the other five quarks are two of the questions that the Standard Model leaves unanswered.

Matter particles have antimatter equivalents, with opposite charge. The quarks carry an additional charge to the electric charge that is called *color charge*. There are three colors, and the corresponding anticolors. Collections of quarks and antiquarks form composite particles, known as *hadrons*. The hadrons are colorless and are divided into mesons (quark-antiquark states) and baryons (three quark states).

2.2 The Electroweak Sector

Within the Standard Model, all the particles and the forces between them are described by a set of principles and equations[2]. The electromagnetic and weak interactions are combined into a unified theory, the Electroweak theory, specified by the $SU(2)_L \times U(1)_Y$ gauge symmetry. In this symmetry the lepton and quark doublets have left-handed *weak isospin* T and *weak hypercharge* Y that relates the electric charge Q to the third component of T, T_3 by

$$Q = T_3 + Y/2$$

The $SU(2)_L \times U(1)_Y$ gauge symmetry introduces 4 fields; three connected with the weak isospin $(W^1_\mu, W^2_\mu, W^3_\mu)$ and one connected with the weak hypercharge (B_μ). Linear combinations of these fields produce the physical photon (A_μ) and the weak bosons:

$$W^\pm_\mu = \frac{1}{\sqrt{2}}(W^1_\mu \pm W^2_\mu)$$

$$\begin{pmatrix} A_\mu \\ Z_\mu \end{pmatrix} = \begin{pmatrix} \cos\theta_W & \sin\theta_W \\ -\sin\theta_W & \cos\theta_W \end{pmatrix} \begin{pmatrix} B_\mu \\ W^3_\mu \end{pmatrix}$$

The weak mixing angle θ_W connects the coupling constants of the $SU(2)_L$ and $U(1)_Y$ interactions (g and g' respectively) to the electric charge:

$$g = \frac{e}{\sin\theta_W} \quad and \quad g' = \frac{e}{\cos\theta_W}$$

In the Standard Model, the field A_μ (photon) has to be massless; in the QED Lagrangian the addition of a mass term $(\frac{1}{2}m^2 A_\mu A^\mu)$ is prohibited by gauge invariance. Gauge invariance of $SU(2)_L \times U(1)_Y$ similarly implies massless weak bosons. In order for the bosons to take masses, the $SU(2)_L \times U(1)_Y$ symmetry can not be invariant and has to be broken. The spontaneous breaking of the symmetry (ElectroWeak Symmetry Breaking, EWSB) not only gives masses to the particles, but it also introduces a new scalar boson, the *Higgs boson*, that has not yet been observed experimentally. It is in fact, the Higgs boson, the only particle that the Standard Model predicts, that has remained unobserved.

[2]The work presented in this thesis is focused on the Electroweak sector of the Standard Model, so this will be discussed further in this chapter. Extensive discussions of the Electroweak theory can be found in textbooks. The ones used for this chapter are References [3] and [4].

Gauge boson masses

When breaking the $SU(2)_L \times U(1)_Y$ symmetry we require that a residual $U(1)$ symmetry remains for the electromagnetic interaction and this symmetry gives a massless boson. The remaining three gauge bosons must acquire mass in this process. This is achieved by introducing four independent scalar fields that transform as an $SU(2)$ doublet:

$$\begin{pmatrix} \phi^+ \\ \phi^0 \end{pmatrix} = \frac{1}{\sqrt{2}} \begin{pmatrix} 0 \\ \upsilon + h \end{pmatrix}$$

where υ represents the vacuum expectation value of the field ϕ and h (the Higgs field) excitations above this minimum. This process keeps the photon massless, while the weak bosons acquire masses determined by the vacuum expectation value and the coupling constants of $SU(2)$ and $U(1)$:

$$M_W = \frac{g\upsilon}{2} \quad and \quad M_Z = \sqrt{(g^2 + g'^2)}\frac{\upsilon}{2}$$

The relation (at tree level) between the boson masses is given using the weak mixing angle:

$$\cos^2 \theta_W = \frac{M_W^2}{M_Z^2}$$

Gauge boson self-interactions

The full $SU(2)_L \times U(1)_Y$ Lagrangian in the unitary gauge is obtained by collecting together the component terms of the Lagrangian density for the fermion, scalar and gauge fields, and the couplings of the fermion fields to the scalar and gauge fields. The gauge field Lagrangian defines the kinetic energy and self couplings of the gauge fields $W_{\mu\nu} \equiv \partial_\mu W_\nu - \partial_\nu W_\mu - gW_\mu \times W_\nu$ and $B_{\mu\nu} \equiv \partial_\mu B_\nu - \partial_\nu B_\mu$ and, consequently, of the electroweak bosons $W^\pm, Z^0$ and γ:

$$\mathcal{L}_{gauge} = -\frac{1}{4} W_{\mu\nu} \cdot W^{\mu\nu} - \frac{1}{4} B_{\mu\nu} B^{\mu\nu}$$

Taking into account that

$$\begin{aligned} W_\mu^1 &= (W_\mu^+ + W_\mu^-)/\sqrt{2} \\ W_\mu^2 &= (W_\mu^+ - W_\mu^-)/\sqrt{2} \\ W_\mu^3 &= \cos\theta_W Z_\mu + \sin\theta_W A_\mu \\ B_\mu &= -\sin\theta_W Z_\mu + \cos\theta_W A_\mu \end{aligned}$$

we get from the first term of the Lagrangian up to quartic interaction vertices between charged bosons or charged and neutral bosons (W^+W^-Z, $W^+W^-\gamma$, W^+W^-ZZ, $W^+W^-Z\gamma$, $W^+W^-\gamma\gamma$ and $W^+W^-W^+W^-$). The second term of the Lagrangian, that includes only neutral bosons, involves in a vertex no more than two bosons. Triple or quartic interaction vertices of only neutral bosons (e.g. ZZZ, $ZZ\gamma$, $Z\gamma\gamma$) are absent in the Standard Model.

2.3 WW and WZ Production

Gauge boson pair production is studied in this thesis; more specifically the WW and WZ production, and this is where the focus will be in this section. The contributing tree-level Feynman diagrams are shown in Figure 2.1. The studies are performed with data generated at the Fermilab's Tevatron, a $p\bar{p}$ collider at $\sqrt{s} = 1.96\ TeV$ (described in Chapter 3).

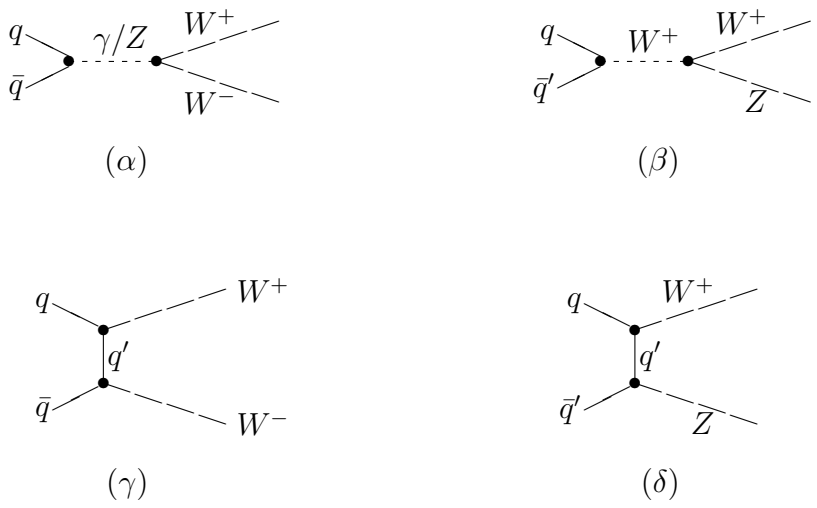

Figure 2.1: WW and WZ production Feynman diagrams

Direct WW and WZ production and boson triple gauge couplings occur in the $s-$channel as shown in (α) and (β). $t-$channel production is also present ((γ) and (δ)). Cancellations in the $s-$ and $t-$ channel diagrams result in low cross sections in the Standard Model. The *Next to Leading Order (NLO)* theoretical cross sections for the WW and WZ production at $\sqrt{s} = 1.96\ TeV$ are [5]:

$$\sigma_{WW} = 12.4 \pm 0.8 \text{ pb}$$

$$\sigma_{WZ} = 4.0 \pm 0.3 \text{ pb}$$

Possible experimental deviations of the WW and WZ cross-sections from the Standard Model theoretical predictions are indications of non-standard direct production, that is non-standard triple $WW(Z/\gamma)$ couplings. These are called *anomalous Triple Gauge Couplings (aTGCs).*

Discussion of aTGCs

Conventionally, the effective leading order Lagrangian that involves triple gauge vertices WWV $(V = Z, \gamma)$ is expressed as follows [6]:

$$\mathcal{L}_{WWV} = ig_{WWV}(g_1^V(W^+_{\mu\nu}W^{-\mu} - W^{+\mu}W^-_{\mu\nu})V^\nu + \kappa_V W^+_\mu W^-_\nu V^{\mu\nu} + \frac{\lambda_V}{m_W^2}W^{+\nu}_\mu W^{-\rho}_\nu V^\mu_\rho)$$

The overall coupling constants are defined as $g_{WW\gamma} = -e$ and $g_{WWZ} = -e\cot\theta_W$. From this form of the Lagrangian, the C, P and CP odd terms are missing (they vanish within the Standard Model). Within the Standard Model, the couplings are given by $g_1^Z = g_1^\gamma = \kappa_Z = \kappa_\gamma = 1$ and $\lambda_Z = \lambda_\gamma = 0$. We define $\Delta\kappa_V \equiv \kappa_V - 1$ and $\Delta g_1^V \equiv g_1^V - 1$, which are both zero in the Standard Model.

The $WW\gamma$ coupling parameters are related to the magnetic dipole moment μ_W and electric quadrupole moment Q_W ([7]):

$$\mu_W = \frac{e}{2M_W}(1 + \kappa_\gamma + \lambda_\gamma)$$

$$Q_W = -\frac{e}{2M_W^2}(\kappa_\gamma - \lambda_\gamma)$$

The value of g_1^γ is fixed to 1 by electromagnetic gauge invariance. The rest of the parameters have not been measured yet with good precision, therefore it is possible that signals for new physics beyond the SM exhibit themselves in this sector[3].

The Tevatron is favorable for such measurements, compared to LEP. LEP was

[3]When considering the effecting Lagrangian described here, we avoided choosing any one specific theory. Our only assumption is that the new physics is not observed directly - that is, the *scale of new physics*, Λ, lies above the energy available to the experiments. If this condition is violated, the approach we used fails. In fact, the parameters λ and $\Delta\kappa$ are expressed as form factors

$$\lambda(\hat{s}) = \frac{\lambda}{(1 + \hat{s}/\Lambda^2)^2},\ \Delta\kappa(\hat{s}) = \frac{\Delta\kappa}{(1 + \hat{s}/\Lambda^2)^2}$$

In order to preserve unitarity at the energies reached by the Tevatron, the parameter Λ has to be set to 1.5-2.0 TeV. [7]

an e^+e^- collider therefore the WWZ coupling could not be studied exclusively; in fact, the WZ production is allowed at the Tevatron ($p\bar{p} \rightarrow W^{(*)} \rightarrow WZ$) but was not allowed at LEP, given that the process $e^+e^- \rightarrow W$ is forbidden, by charge conservation. Furthermore, the Tevatron explores a higher energy range with respect to LEP, because of the higher center of mass energy and the more extended parton center-of-mass energy ($\sqrt{\hat{s}}$) spectrum, that results in a larger range of parton-parton collision energies.

2.3.1 WW and WZ Decay Modes

To observe gauge boson pair production signals, the decay products of W's and/or Z's have to be observed above particle backgrounds. The decay modes of W's, Z's and their pair production are listed in Table 2.3.

The leptonic decay mode

Diboson production in the fully leptonic decay channel is rare because of low branching ratios. However it provides essentially background free signals. This is in fact the channel in which the WW and WZ production has been observed at hadron colliders, and the Standard Model predictions for the cross section have been verified [8]. Because of the very small branching ratios, this channel is not very promising for aTGC studies. Another limitation of this decay mode is that the partons center-of-mass energy can not be reconstructed because of the missing transverse energy ambiguity[4].

The semi-leptonic decay mode

The WW and WZ production in the charged lepton, neutrino plus jets decay channel will be studied in this thesis. The Feynman diagrams for this decay mode are shown in Figure 2.2. The hadronically decaying W ($W \rightarrow jj$) can not be differentiated from a hadronically decaying Z ($Z \rightarrow jj$) due to the limited jet energy resolution[5]. We therefore study the WW and WZ production together.

This is a decay mode never observed at hadron colliders due to the large $W+jets$ background. The cross section of $W + jets$ production at $\sqrt{s} = 1.96$ TeV is of the

[4]The event in the detector can be fully reconstructed in the transverse plane. In this plane, the missing energy represents particles that do not leave signals in the detector (neutrinos). More on the missing transverse energy will be follow in Chapter 4.

[5]When the quarks hadronize inside the detector, a collimated flow of high energy hadrons is generated. This is defined as a *jet*. More on jets will follow in Chapter 4.

$W^{\pm}$ decay modes	Branching Ratio (%) ([2])
$\ell^{\pm}\nu_{\ell}$	32.40 ± 0.27
$hadrons$	67.60 ± 0.27
Z^0 decay modes	Branching Ratio (%) ([2])
$\ell^{+}\ell^{-}$	10.0974 ± 0.0069
$invisible$	20.00 ± 0.06
$hadrons$	69.91 ± 0.06

$W^{+}W^{-}$ decay modes	Branching Ratio (%)
$\ell^{+}\nu_{\ell}\ell'^{+}\nu_{\ell'}$	10.5
$\ell^{+}\nu_{\ell} + hadrons$	43.8
$hadrons$	45.7
$W^{\pm}Z^0$ decay modes	Branching Ratio (%)
$\ell^{\pm}\nu_{\ell}\ell'^{+}\ell'^{-}$	3.3
$\ell^{\pm}\nu_{\ell}\ \nu\nu$	6.5
$\ell^{\pm}\nu_{\ell} + hadrons$	22.6
$hadrons + \ell'^{+}\ell'^{-}$	6.8
$hadrons + \nu\nu$	13.5
$hadrons$	47.3

Table 2.3: The $W^{\pm}$, Z^0 and WW and WZ decay modes and branching ratios. The boson branching ratios are known with good precision, we therefore consider the precision in the diboson branching ratios negligible. In this table, ℓ stands for a lepton, an electron, a muon or a tau. Experimentally, taus are hard to reconstruct. Only electrons or muons will be discussed further in this thesis. The decays of Z^0 to neutrinos (invisible Z^0) will not be considered.

order of 300 pb, resulting in a signal over background ratio that is smaller than 1%, making therefore the signal very difficult to observe. However, the branching ratio for this decay mode is very significant, making this channel favorable for aTGC studies.

Given that the signal over background is initially very small, sophisticated statistical techniques need to be used in an attempt to observe this decay mode. This decay mode is topologically similar to associate production of a Higgs boson with a W (e.g. Figure 2.3) therefore techniques that are developed for the WW/WZ searches are also applicable in Higgs searches. The event topology is common in many other interesting process (e.g. SUSY signatures and single top), and the WW

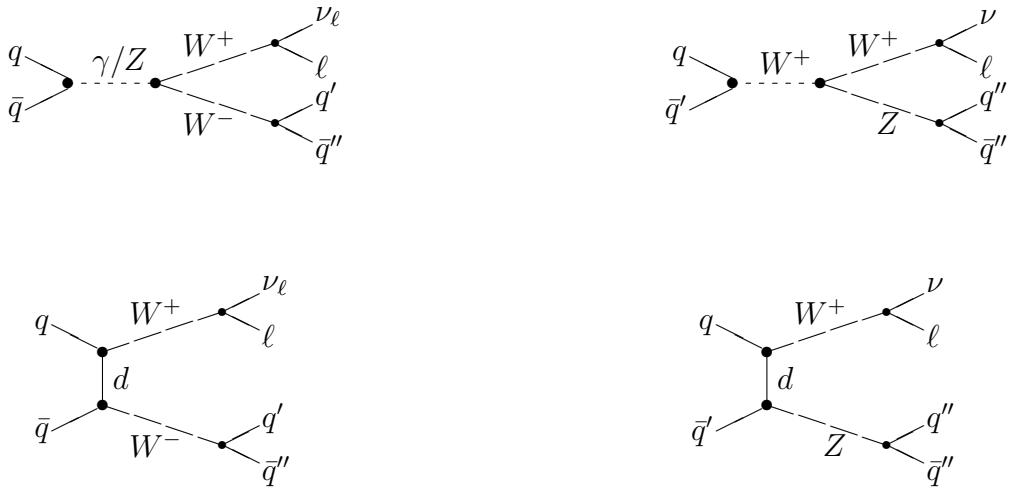

Figure 2.2: Feynman diagrams for WW and WZ production in the semi-leptonic decay channel; there are similar diagrams for $W^- \to \ell\nu$ and $W^+ \to q\bar{q}$

and WZ are backgrounds for such processes. It is therefore clear that better understanding of the diboson production helps in eliminating significant backgrounds in various other searches.

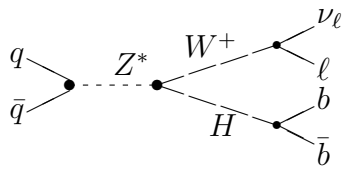

Figure 2.3: A Higgs produced in association with a W (Higgs-Strahlung). This is a process topologically similar to the WW production in the semi-leptonic decay channel.

The hadronic decay mode

Purely hadronic decays of gauge bosons are dominated by large four-jet QCD background, they are therefore practically unobservable at hadron colliders.

2.4 Current Knowledge

The tools that high energy physicists use to explore the hidden details of nature are the particle colliders. The history of particle colliders is short but the results achieved are astonishing.

The W and Z bosons were observed experimentally in 1983 by the $UA1$ and $UA2$ collaborations at the *Super Proton Synchrotron (SPS)* collider, at CERN[6]. However, the diboson production needed the *Large Electron-Positron (LEP)* collider's clean leptonic environment to be extensively studied. Currently, at the Tevatron accelerator, located in the Fermi National Laboratory (FNAL) in the USA, two experiments, CDF and DØ, collect data from $p\bar{p}$ collisions that are used to stringently constrain the diboson system properties. The *Large Hadron Collider (LHC)*, where two multi-purpose experiments have been built, will start $proton - proton$ collisions at unprecedented energies within 2008, opening a new era for high energy physics.

Results from the LEP and the Tevatron experiments are presented in this section.

2.4.1 Previous Results from LEP

WW measurements

All four experiments measured the WW cross section with good precision using the total accumulated data of $\approx$3 fb^{-1} integrated luminosity, in all decay channels. The advantage of LEP is its clean leptonic environment, resulting in all the e^+e^- energy going into the hard scattering processes and making possible the observation of hadronically decaying W's, and also the semi-leptonic decays of WW production. The WW production cross section measured at LEP agrees well with the Standard Model predictions (Figure 2.4). The WZ production is not available at LEP, as already mentioned.

TGC measurements

The four LEP experiments measured the charged TGC parameters at 68% CL and defined 95% CL intervals. The LEP measurements are summarized in Table 2.4. The results agree with the SM predictions for TGCs ($g_1^Z = \kappa_\gamma = 1,\ \lambda_\gamma = 0$).

[6]The SPS was at the time operated as a $p\bar{p}$ collider.

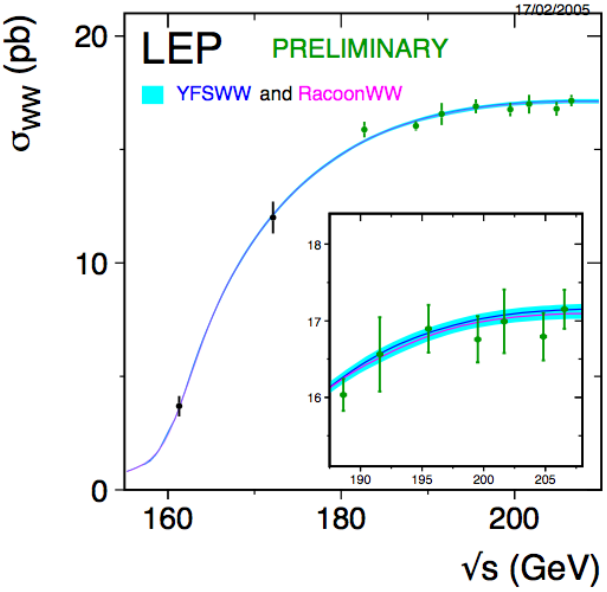

Figure 2.4: Measurements of the W-pair production cross-section, compared to the predictions of the Standard Model. The shaded area represents the uncertainty on the theoretical predictions, estimated to be ±2% for $\sqrt{s} < 170$ GeV and ranging from 0.7 to 0.4% above 170 GeV [12].

Parameter	68% CL	95% CL
g_1^Z	$0.991^{+0.022}_{-0.021}$	[0.949, 1,034]
κ_γ	$0.984^{+0.042}_{-0.047}$	[0.895, 1,069]
λ_γ	$-0.016^{+0.021}_{-0.023}$	[-0.059, 0.026]

Table 2.4: The combined 68% CL values and 95% CL intervals for TGCs, obtained by the four LEP experiments. In each case the parameter listed is varied while the other two are fixed to their Standard Model values. Both statistical and systematic errors are included. [12]

2.4.2 Results from Tevatron

At the Tevatron during the RUN I (1992-1996), with approximately 100 pb^{-1} of integrated luminosity accumulated in each experiment, the diboson physics program was very rich with both leptonic and semi-leptonic decay channels being studied and limits on the TGC values set. However, during the RUN II of Tevatron more than 10 times the RUN I integrated luminosity has been accumulated thus far, allowing more precise measurements and limits. The current status of the WW and WZ

production studies at the RUN II Tevatron experiments will be presented in this section.

WW and WZ in leptonic final states

The most precise measurements for the WW and WZ production come from CDF, which has a very intensive diboson program at RUN II.

The signature of the WW signal in the leptonic decay is two isolated high-E_T leptons with opposite charge and large missing transverse energy from the W neutrinos. After the selection cuts, the dominant backgrouds are form Drell-Yan, other diboson decays and $W + jets$ where a jet fakes an isolated lepton.

The study of the leptonic WZ production allows one to search for anomalous WWZ coupling independently of the $WW\gamma$ coupling, in contrast to WW production. The WZ production has been observed by CDF in October 2006 [8], using 1.1 fb^{-1}. CDF has an update to the first observation of WZ, using 1.9 fb^{-1} [9]. The WZ analysis uses a final state of 3 leptons (electrons or muons) and missing transverse energy. The dominant backgrounds are from $Z + X$, where X is a Z, γ, or jet faking a lepton. Figure 2.5 shows the missing transverse energy distribution for candidates both inside and outside the WZ signal region.

The measured cross sections for the two processes are summarized in Table 2.5. All results are compatible with the SM predictions.

Process	Measurement (pb)	NLO (pb)	$\int \mathcal{L}dt$
$\sigma(p\bar{p} \to WW)$	$13.6 \pm 2.3(stat) \pm 1.6(sys) \pm 1.2(lumi)$	12.4 ± 0.8	825 pb^{-1}
$\sigma(p\bar{p} \to WZ)$	$4.3^{+1.3}_{-1.0}(stat) \pm 0.2(sys) \pm 0.3(lumi)$	3.7 ± 0.3	1.9 fb^{-1}

Table 2.5: Double vector boson production in leptonic final states cross section measurements, as measured by the CDF Collaboration [8].

Based on the WZ production, both CDF and DØ collaborations have set limits in the WWZ TGCs. The limits are summarized in Table 2.6.

WW and WZ in semi-leptonic final states

At RUN II and prior to this thesis, the semi-leptonic decay production of WW and WZ has been studied only at CDF, using 350 pb^{-1} of integrated luminosity of data [11]. The measured cross section is $\sigma_{WW+WZ} = 11 \pm 11(stat) \pm 6(sys)$ pb. The measured 95% CL limit on the cross section is estimated to be $\sigma_{WW+WZ} < 36$ pb.

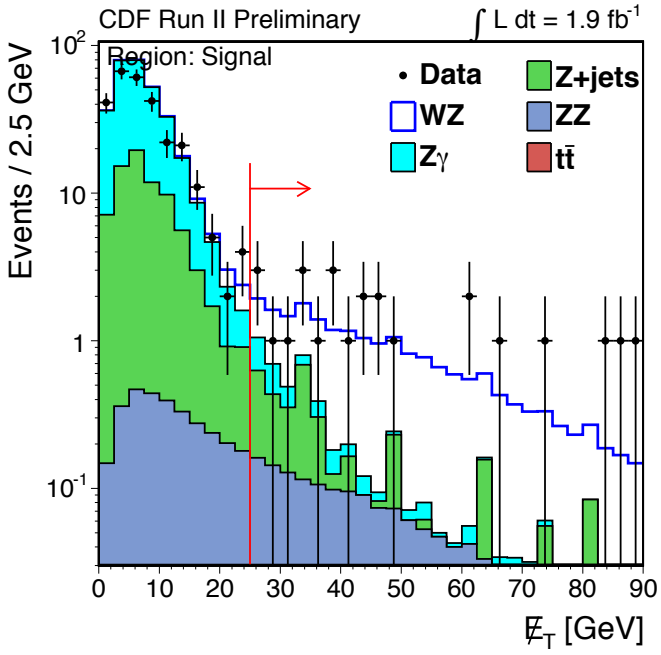

Figure 2.5: Missing E_T distribution, for the $WZ \to \ell\ell\ell\nu$ process. The signal region contains events with missing E_T >25 GeV.

CDF	
$\Lambda = 1.5$ TeV	$\Lambda = 2.0$ TeV
$-0.14 < \lambda_Z < 0.16$	$-0.13 < \lambda_Z < 0.13$
$-0.17 < \Delta g_1^Z < 0.27$	$-0.15 < \Delta g_1^Z < 0.24$
$-0.86 < \Delta\kappa_Z < 1.36$	$-0.82 < \Delta\kappa_Z < 1.27$
DØ	
$\Lambda = 1.5$ TeV	$\Lambda = 2.0$ TeV
$-0.18 < \lambda_Z < 0.22$	$-0.17 < \lambda_Z < 0.21$
$-0.15 < \Delta g_1^Z < 0.35$	$-0.14 < \Delta g_1^Z < 0.34$
$-0.14 < \Delta\kappa_Z = \Delta g_1^Z < 0.31$	$-0.12 < \Delta\kappa_Z = \Delta g_1^Z < 0.29$

Table 2.6: TGC limits from the Tevatron (95% CL).

Limits are set in the TGC parameters using $\Lambda = 1.5$ TeV and $\Delta g = 0$: $(\Delta\kappa, \lambda) = ([-0.51, 0.45], [-0.29, 0.29])$.

2.5 Experimental Roadmap

In this thesis, we present a search for WW and WZ production in lepton, neutrino plus jets final state. This channel has not yet been observed in hadron colliders due to the large $W + jets$ background.

In order to study this decay channel, we use data collected by the CDF detector. To translate the data into physical objects, a sophisticated trigger system and reconstruction algorithms are used. In the data we select electrons, missing transverse energy from the neutrinos that leave no signatures in the detectors, and jets in order to reconstruct the signature of interest.

Both the signal and the background are modeled using Monte Carlo and the quality of the modeling is verified with the data themselves. The signal we are searching for has a small cross section with respect to the background cross section, therefore the signal fraction is initially very small ($< 1\%$). A tool with large discriminative power is needed in order to separate the signal from the background; in this analysis, an Artificial Neural Network has been used. In the Neural Network output we apply a cut and reject all events below this cut.

For the events that pass the cut, the dijet invariant mass shape of the two leading jets of the event are plotted and parameterized. The parameterizations are fed into a likelihood fit where the signal fraction is a free parameter. The likelihood fit to the data invariant mass shape returns the signal fraction, that is the number of interest in this analysis. It is in fact interpreted as a number of signal events, and a cross section.

The significance of the measurement is estimated using the likelihood ratio as a test statistic. Using this test statistic, the probability that the background fluctuates and fakes the signal is evaluated and is interpreted as a significance. Finally, the systematic uncertainties - the uncertainties in various assumptions done in the process of the analysis procedure - are estimated. With the total error, statistical and systematic, a new final significance is evaluated.

All the various steps for the search for WW and WZ production in the semi-leptonic decay channel are presented in detail in this thesis.

2.6 Summary

The Standard Model is the theory that describes all the currently known particles and their interactions. This model leaves many crucial questions unanswered and

other theories suggest solutions. However experimentally, the Standard Model is in agreement with all data. Some of the standard model parameters have not been measured with good precision experimentally, beyond the Standard Model physics may be hidden there. Unknotting the hidden details of nature is one of the most pressing challenges awaiting particle physics.

One of the processes sensitive to new physics is the diboson production and the diboson production to the lepton, neutrino and jets final state is the search that will be presented in this thesis. Theoretical aspects of the diboson production and the current experimental results are presented in this chapter. A roadmap to the analysis is also given.

The experimental apparatus, the data acquisition and processing and the methodology of the analysis will follow in the next chapters. The results and the future perspectives are finally presented.

Chapter 3

Experimental Apparatus

The tools that particle physicists use to reveal the secrets of nature are the accelerators, a chain of machines used to produce, accelerate and store particles at high energies. The Tevatron is currently the world's highest-energy particle accelerator and hadron collider. It is the landmark particle accelerator of Fermilab (Fermi National Accelerator Laboratory), a U.S. Department of Energy national laboratory specializing in high-energy particle physics. In the Fermilab's Tevatron, protons and anti-protons are accelerated to a center of mass energy of 1.96 TeV and collide at two points inside the accelerators. In these two points, specialized devices such as CDF (Collider Detector at Fermilab) that record the products of the collisions, are placed. These devices, called *detectors*, consist of layers of material such that particles that transverse them leave their *signatures*. Very fast and sophisticated electronics transform these signatures into information that physicists can use to identify the nature of the collisions.

In this chapter, the Fermilab's accelerator chain and the CDF detector are described.

3.1 The Fermilab's Accelerator Chain

The Fermilab's accelerator chain is pictured in Figure 3.1. It consists of a number of different accelerator components: the Pre-Accelerator, Linac and Booster (collectively known as the Proton Source), the Debuncher and Accumulator (referred as the Antiproton Source), and the Main Injector and Tevatron [13], [14].

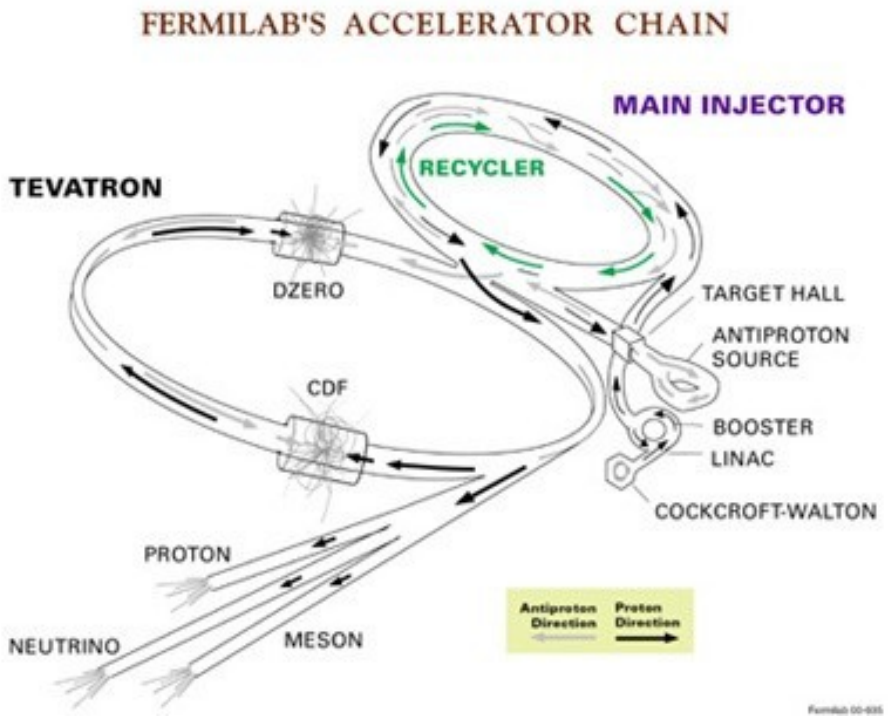

Figure 3.1: The Fermilab's accelerator chain.

The Proton Source

The first step in the accelerator chain is the *Cockroft-Waltron* electrostatic accelerator, which is a DC voltage source. A gas of hydrogen is ionized by addition of electrons and the resulting negative ions are accelerated electrostatically up to an energy of 750 keV. The hydrogen ions enter the *Linac* [15], a 130 m linear accelerator in which a series of radio-frequency (RF) cavities accelerate the ions to 400 MeV. At the end of the Linac, a series of carbon foils remove the electrons from the hydrogen ions. The resulting protons are further accelerated to 8 GeV by the *Booster* [16], a synchrotron accelerator with a circumference of 475 m and cycle time 1/15 sec. The protons are then transfered to the *Main Injector*.

The Main Injector

The Main Injector is a synchrotron with a circumference of 3.3 km and has two main functionalities: (1) it accelerates the particles from 8 GeV to 150 GeV and injects them into the Tevatron and (2) it accelerates the protons to 120 GeV and sends them to the *Target Station* for anti-proton production [17].

Anti-proton production

The 120 GeV protons that are directed towards the Target Station are directed onto a nickel target every 1.5 sec. The resulting particles, produced at different angles and momenta, are focused with a lithium lens and passed through a dipole magnet that selects the anti-protons with an average energy of 8 GeV. The anti-protons at this stage have a wide energy spectrum. To reduce the spread in energy, the anti-protons are sent into the *Debuncher*, a synchrotron that makes the beam easier to manipulate in the following acceleration steps. The anti-protons are stochastically cooled[1] and collected in the *Accumulator* ring where they are accelerated up to 8 GeV. They are stacked in 36 bunches of $\approx 3 \times 10^{10}$ particles each. About one anti-proton arrives at the Accumulator for every 10^5 protons that hit the proton target. The anti-protons are transfered in the *Recycler* until a sufficient stash of antiprotons is reached for the desired initial luminosity. The Recycler is a fixed energy (8 GeV) storage ring in the Main Injector tunnel. Keeping a large stash of anti-protons inside the Recycler has been one of the most significant engineering challenges and the excellent performance of the Recycler is an achievement of prime importance for the good operation of the accelerator [18].

The Tevatron

When sufficient antiprotons are collected in the Recycler, the beam is transfered into the Main Injector. The proton and anti-proton bunches[2] accelerated to 150 GeV are injected in the *Tevatron* ring, where they are accelerated to 980 GeV. The Tevatron is a synchrotron with a circumference of 6.1 km. It uses superconducting dipole magnets, each one producing a field of 4.2 T, to bend the beams around the ring. The beams are kept apart with electrostatic separators and arranged in 3 trains of 12 bunches with 396 ns separation. There are two low β (small beam size) points inside the Tevatron, where the electrostatic separators allow collisions. The CDF and D0 detectors are installed at these points.

[1] For the stochastic cooling, the average motion of the anti-protons is sampled and this information fires a kicker magnet, that corrects their trajectory.

[2] The protons are arranged in 36 bunches of $\approx 3.3 \times 10^{11}$ particles and the anti-protons in 36 bunches of $\approx 3.6 \times 10^{10}$ particles.

3.1.1 Luminosity

The *instantaneous luminosity* $\mathcal{L}$ is defined as the interaction rate per unit cross section of the colliding beams (collisions/(cm^{2}s)). It can be approximated by:

$$\mathcal{L} = \frac{f \cdot B \cdot N_p \cdot N_{\bar{p}} \cdot F}{2\pi(\sigma_p^2 + \sigma_{\bar{p}}^2)}$$

where f is the revolution frequency (*typically 47.7 kHz*), B the number of bunches in each beam (36 *bunches*), $N_p(N_{\bar{p}})$ is the number of protons (anti-protons) in a bunch (3.3×10^{11} *protons and* 3.6×10^{10} *anti-protons*) and $\sigma_p(\sigma_{\bar{p}})$ is the r.m.s. beam size at the collision points (*at CDF*, 20 μm). The beam width and its evolution around the accelerator can affect the collisions rate, and this dependence is expressed in the form factor F (*typically 0.72*). At CDF, the instantaneous luminosity at the beginning of the store typically exceeds 10^{32} collisions/(cm^{2}s) (Figure 3.2) with the peak initial luminosity being at 3×10^{32} collisions/(cm^{2}s).

For physics studies the *integrated luminosity*, $\int \mathcal{L}dt$, is the quantity of interest. For a specific process of cross-section σ, the number of events that are generated in a specific time interval are:

$$N = \sigma \times \int \mathcal{L}dt$$

The integrated luminosity is therefore expressed in units of *(cross-section)*$^{-1}$. At CDF[3], there have been so far (early 2008) more than 3 fb^{-1} of integrated luminosity delivered and more than about 2.7 fb^{-1} are already on tape (Figure 3.3). If the Tevatron keeps on running until 2009, approximately 6-8 fb^{-1} of data are expected to be delivered at CDF.

[3]CDF uses dedicated counters for luminosity measurements, that are described in a later section.

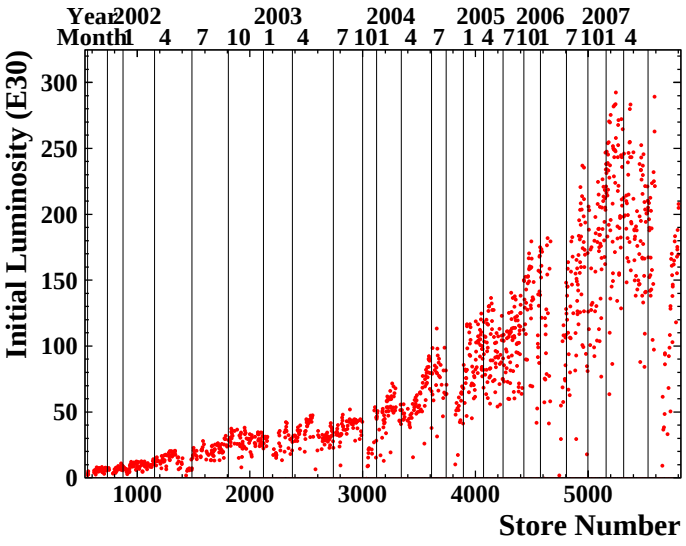

Figure 3.2: Initial instantaneous luminosity at CDF.

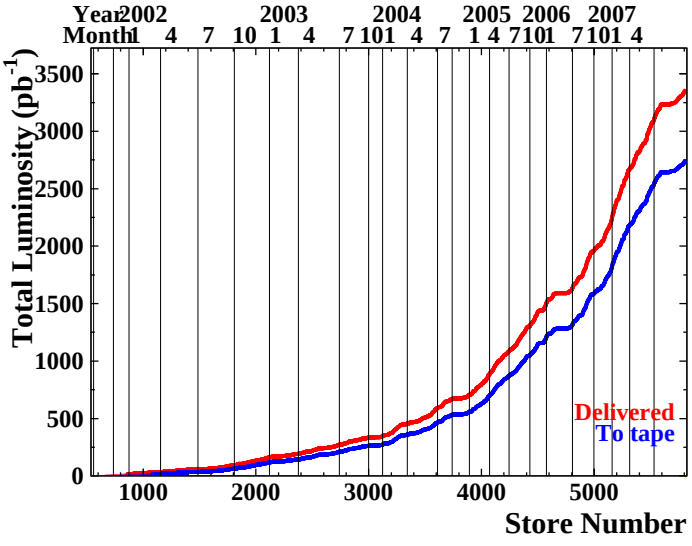

Figure 3.3: Integrated luminosity at CDF, delivered and on tape.

3.2 The CDF II Detector

The Run II CDF detector [19] is a general-purpose multilayered detector designed to study many aspects of particle physics. It combines precise tracking with fast calorimetry and muon detection. A sketch of the detector is shown in Figure 3.4. A tracking system is positioned closest to the beamline to provide accurate momentum determination of charged particles. The tracking system is immersed in a 1.4 T uniform magnetic field, aligned in the proton direction, produced by a superconducting solenoid. Calorimeters located outside the tracking volume provide energy measurement of electrons, photons and jets. The geometrical coverage of the calorimeters is maximized to measure the energy flow of all particles produced in a collision and indirectly to measure the missing transverse energy resulting from the presence of weakly interacting particles like neutrinos. Muon chambers are located on the outer part of the CDF detector. In the following sections we will briefly describe each of the subdetectors of CDF. The geometry of the detectors is shown in Figure 3.5. Emphasis in this chapter will be given in the detector components used for the analysis presented in this thesis (in brief, tracking, calorimetry and central muon detection).

3.2.1 CDF Coordinate System and Kinematic Definitions

CDF uses a right-handed coordinate system, with the origin at the center of the detector. It has the z axis along the beamline, in the direction of the protons. The x axis is in the same plane as the Tevatron ring and points outwards and the y axis points straight upwards. Based on a cartesian system defined by the x, y and z coordinates just described, one can define the cylindrical coordinates r, ϕ and θ, which are more commonly used[4].

A more natural unit of measurement in collider physics is the Lorentz invariant variable *rapidity,* y, that is defined as:

$$y = \frac{1}{2} \ln \frac{E + p_z}{E - p_z}$$

For highly relativistic particles, which is the case for CDF, the rapidity can be approximated by the *pseudorapidity,* η, defined as:

$$\eta = -\ln \tan (\theta/2)$$

[4]The azimuthal angle ϕ is defined in the $x - y$ plane, and is the angle with respect to the x axis. The polar angle θ is the angle with respect to the z axis.

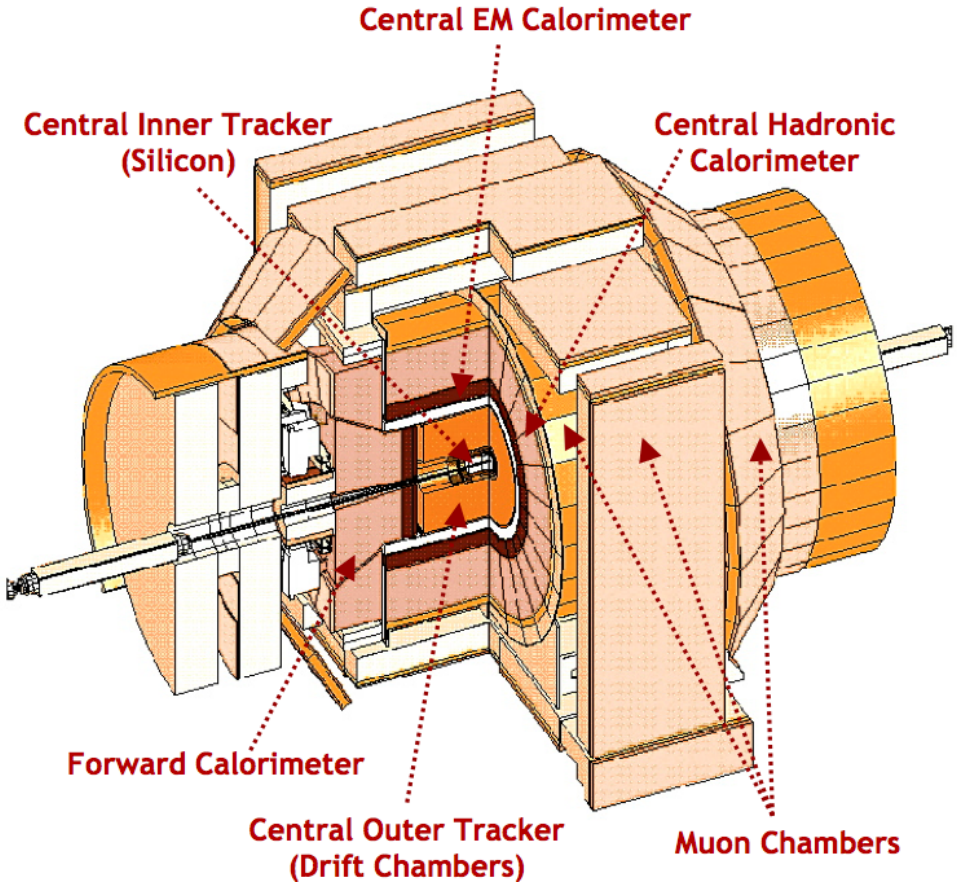

Figure 3.4: The CDF II Detector.

This variable is independent of the particle types and is simply related to the polar angle. It is widely used at CDF.

At CDF, an event can be fully reconstructed only in the $x-y$ plane (*transverse plane*), where the total energy flow should be zero. The z component of the total momentum cannot be used as a constraint in hadron colliders since we are unaware of the momentum of the initial state partons inside the colliding protons and antiprotons and we don't detect the beam fragments which stay close to the beamline. At the $x-y$ plane we define the *transverse momentum*

$$p_T = p \times \sin\theta$$

and the *transverse energy*

$$E_T = E \times \sin\theta$$

At high p_Ts, the transverse energy is approximated by $E_T \approx p_T$.

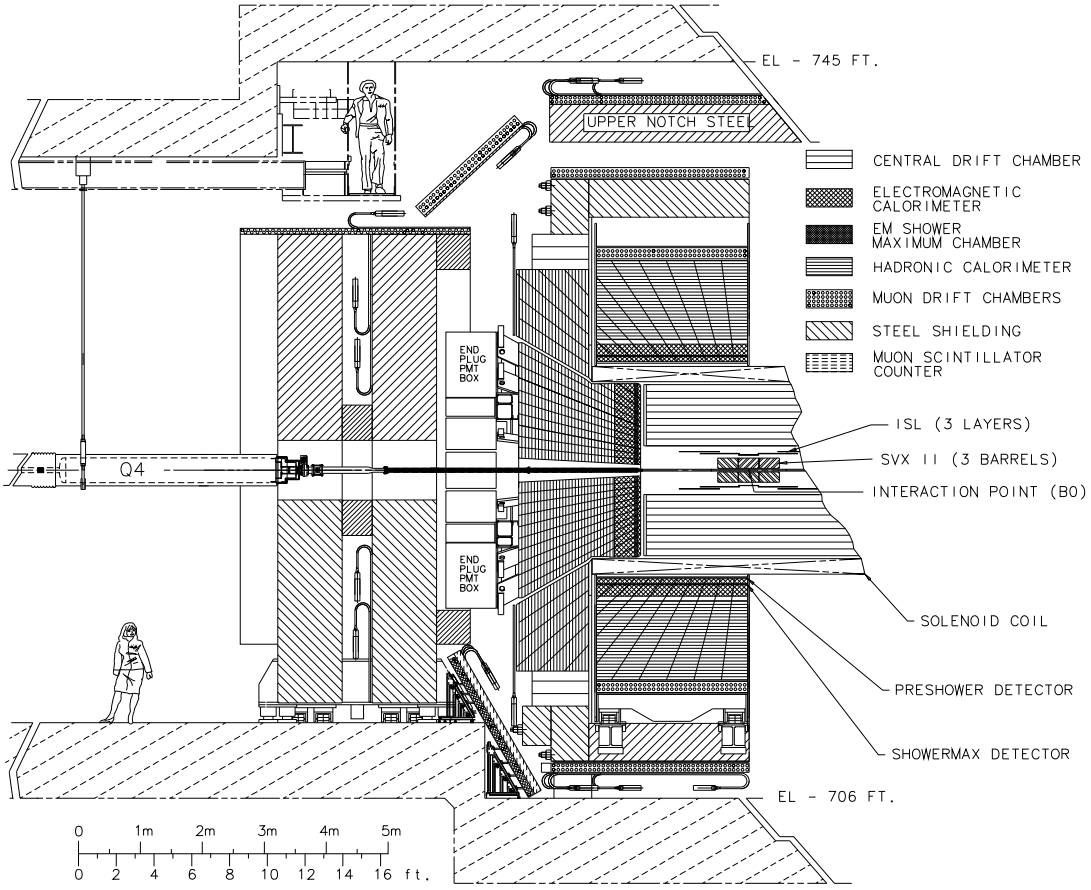

Figure 3.5: Elevation view of the CDF detector.

The neutrino does not leave any signature in the detector. It is reconstructed by the energy imbalance in the transverse detector plane. The presence of a neutrino creates a large apparent imbalance in the total transverse energy flow as measured by the calorimeters. The missing transverse energy ($\not\!\!E_T$) is defined as

$$\not\!\!E_T = |\sum_i E_{T,i}\hat{n}_{T,i}|$$

where the sum is over all the calorimeter towers (that will be explained in a later section) and $\hat{n}_{T,i}$ is the transverse component of the unit vector pointing from the interaction point to the calorimeter tower i.

Given that the $\not\!\!E_T$ can only be reconstructed in the transverse plane, a W decaying leptonically can be reconstructed only at this plane. A variable that

will be used in this thesis is the mass of a system in the transverse plane, called *Transverse Mass*, M_T. It is defined in the specific case of the leptonically decaying W as $M_T = \sqrt{(p_T^{\mu} + \not\!\!E_T)^2 - (\vec{p_T^{\mu}} + \vec{\not\!\!E_T})^2}$. Doing some algebra, the transverse mass can be written as a function of the lepton p_T, the $\not\!\!E_T$ and the ϕ angle between the two:

$$M_T = [2 \cdot p_T \cdot \not\!\!E_T \cdot (1 - \cos\Delta\phi(lepton, \not\!\!E_T)]^{1/2}$$

3.2.2 Tracking System

The tracking system provides measurement of track parameters and vertices of charged particles. It is located within a superconducting solenoid magnet that provides 1.4 T magnetic field oriented along the incident beam direction. A layout of the tracking system, that employs silicon detectors, closer to the beam pipe, and drift chambers in the outer part, is shown in Figure 3.6.

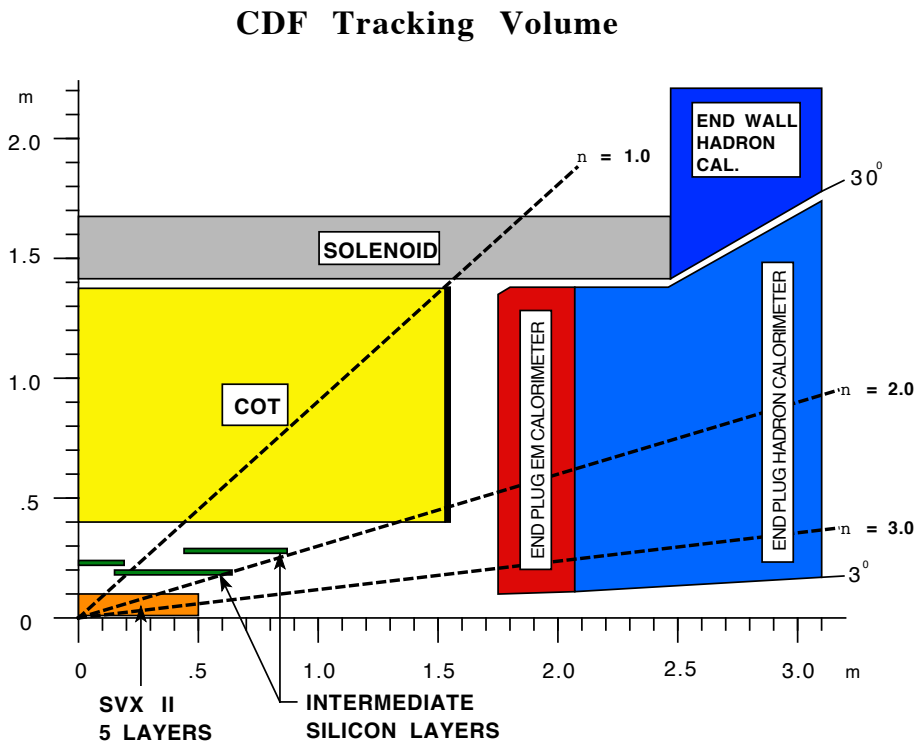

Figure 3.6: Longitudinal View of the CDF II Tracking System. The drawing includes a part of the calorimeter. The L00 is not visible in the scale of this drawing. The η coverage of the detectors is shown in the figure; L00 covers $|\eta| < 4$ while SVX and ISL cover $|\eta| < 2$. The COT provides a coverage up to $|\eta| = 1.0$.

Silicon Detectors

There are three sets of silicon detectors arranged coaxially; closest to the beampipe the *Layer 00 (L00)*, followed by the *Silicon Vertex Tracker (SVX)* and the *Intermidiate Silicon Layers (ISL)* in the outer part of the silicon system[5]. For the record, all silicon detectors were newly built for Run II of CDF. SVX was built as a replacement for the silicon detectors at Run I while L00 was a part of the beyond the baseline proposal for Run II.

The L00 consists of single-sided microstrip detectors that provide axial measurements. This layer is mounted directly on the beampipe (r=1.6 cm) to provide a measurement point as close as possible to the interaction point.

The SVX is made of 5 concentric layers of double-sided microstrip silicon detectors arranged in 3 barrels, 96 cm long and located at radii ranging from 2.4 to 10.7 cm. In three of the layers the stereo angle between the two sides of the strips is 90°, providing an axial measurement together with information in the z direction. The remaining two layers are arranged at a small stereo angle of 1.2°, providing an axial measurement together with information in the z and ϕ directions. The SVX detector resolution for an axial measurement point is ≈12 μm.

The ISL is made of three layers of double sided silicon detectors that are located at radii from 20 cm to 29 cm. One side of the silicon detectors contains axial strips while the other side contains stereo strips at an angle of 1.2°. The ISL measures the axial position of tracks with a resolution of ≈16 μm and provides one to two measurement points.

Central Outer Tracker (COT)

The COT is a general purpose tracker in the central regions of the detector, surrounding the silicon system. It is an open-cell drift chamber with argon-ethane gas in 50/50 mixture, located at radii between 40 cm and 132 cm. It provides 96 measurement points of each charged particle trajectory up to $|\eta| = 1.0$.

It is arranged in 8 superlayers, each containing 12 layers of sense wires strung in alternation with potential wires. The drift cells are arranged such that the wires are positioned in the middle of the two cathode planes that are separated by 2 cm. The wires in half of the superlayers are strung parallel to the beamline, providing axial measurements. For the other four stereo superlayers, the wires are strung at small

[5]None of the silicon detectors is used for the track reconstruction in the analysis presented in this thesis, therefore the description is brief.

stereo angles of $\pm 2^{\circ}$ with the beamline, therefore providing stereo information of a hit position. Axial and stereo layers alternate, starting with a stereo superlayer at the inner radius (Figures 3.7 and 3.8).

The COT single-hit resolution has been measured in situ to be 140 μm using Z boson decays into muon pairs. Hits are combined together to form a track, whose transverse momentum is calculated by measuring its helical trajectory inside the magnetic field provided by the solenoid. Using muon cosmic rays, the momentum resolution has been measured to be:

$$\frac{\delta_{p_T}}{p_T^2} \approx 1.5 \times 10^{-3} [GeV/c]^{-1}$$

The momentum calibration of the COT is achieved using J/ψ particles that have low p_T; the mass of the particles is compared to the world average mass, and the momentum scale of the tracking system is normalized accordingly.

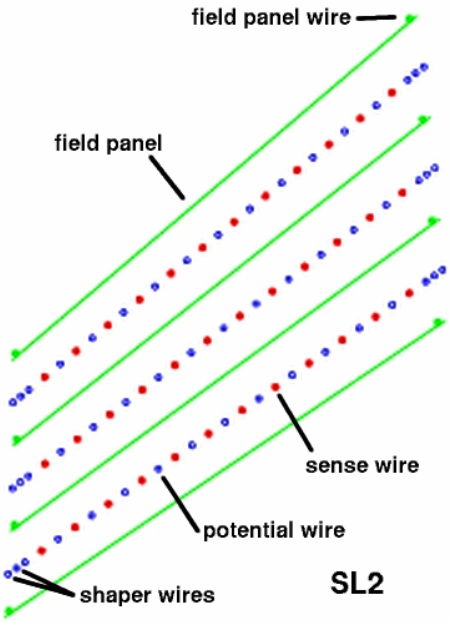

Figure 3.7: Cross-sectional view of COT cells.

3.2.3 Calorimetry

The primary purpose of the CDF calorimeters is to measure energy and position of the charged particles and neutral particles that escape the tracking region. The CDF calorimeters are organized in two subsystems, the inner calorimeters and the outer

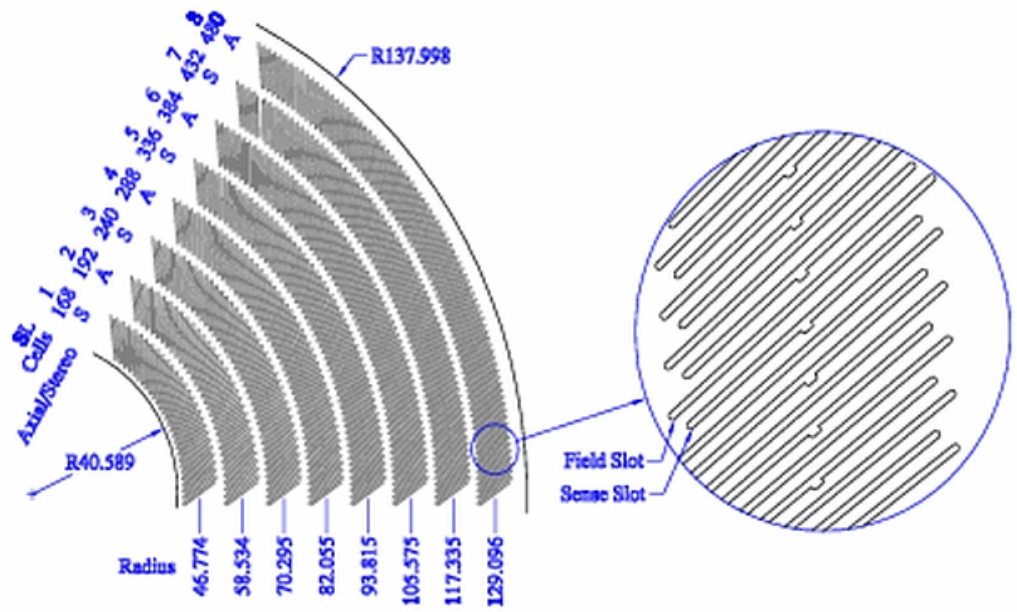

Figure 3.8: COT endplate (section). Slots for field plates and wire planes alternate.

calorimeter, optimized to better react respectively to electromagnatic and hadronic interacting particles. They instrument two regions with the central barrel calorimeter covering $|\eta_{det}| < 1$ and the plug calorimeters covering $1.1 < |\eta_{det}| < 3.6$, in a geometry shown in Figure 3.9. The calorimeters are segmented into towers that read out independently providing spatial information of the particle detection. Sampling calorimetry is used; layers of passive material (absorbers) favor the development of showers and alternate with scintillator tiles arranged in projective towers, where photons are produced and collected to measure the energy deposited in a given tower.

Central Calorimeter

The central calorimeter ($|\eta_{det}| < 1$) consists of the *Central Electromagnetic Calorimeter (CEM)*, the *Central Hadronic (CHA)* and the *Wall Hadronic (WHA)* calorimeters. Both electromagnetic and hadronic calorimeters are scintillator-lead calorimeters and they have the same geometry of towers, such that a comparison of the energy deposition in each element can be made for any individual tower. This helps to the discrimination between electrons and pions. The electron-photon separation is achieved using tracking information.

To increase the spatial resolution of the calorimeter, two proportional chambers

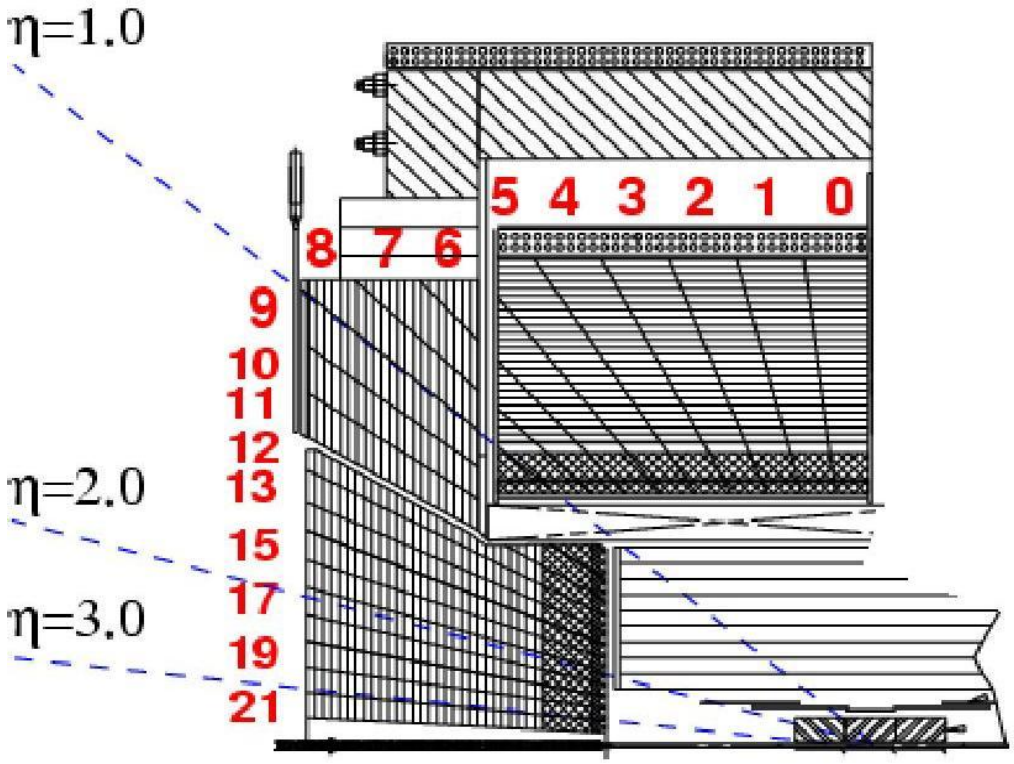

Figure 3.9: A schematic drawing of the calorimeter. The central region extends up to $\eta = 1$.

are embedded in each wedge of the CEM; the *Central Electromagnetic Strip chambers (CES)*, that consist of wires in the $r - \phi$ plane and cathode strips in the z direction. They measure charge deposition at the depth of the maximum electromagnetic shower development. Between the magnetic coil and the CEM, additional wire chambers and scintillator tiles are placed and act as shower pre-samplers, to improve photon identification.

All the calorimeters are segmented in pseudorapidity and azimuth, with a projective tower geometry pointing to the interaction point. A segmentation uniform in pseudorapidity instead of the polar angle is chosen, as in high energy collisions the number of charged particles per unit of rapidity is approximately constant in the central region. The towers cover 0.1 units of η by 15° in ϕ.

The CEM is composed of passive layers of 3.2 mm thick lead sheets alternating with active layers of 5 mm thick polystyrene scintillators (Figure 3.10). In each tower, the signals of all counters are added to give a single measurement. The

lateral profile of the shower is determined by the CES. The energy resolution[6] of the CEM is:

$$\frac{\sigma(E)_{CEM}}{E} = \frac{13.5\%}{\sqrt{E_T}} \oplus 1.7\%$$

and the position resolution is 0.2 cm in both the x and y axes.

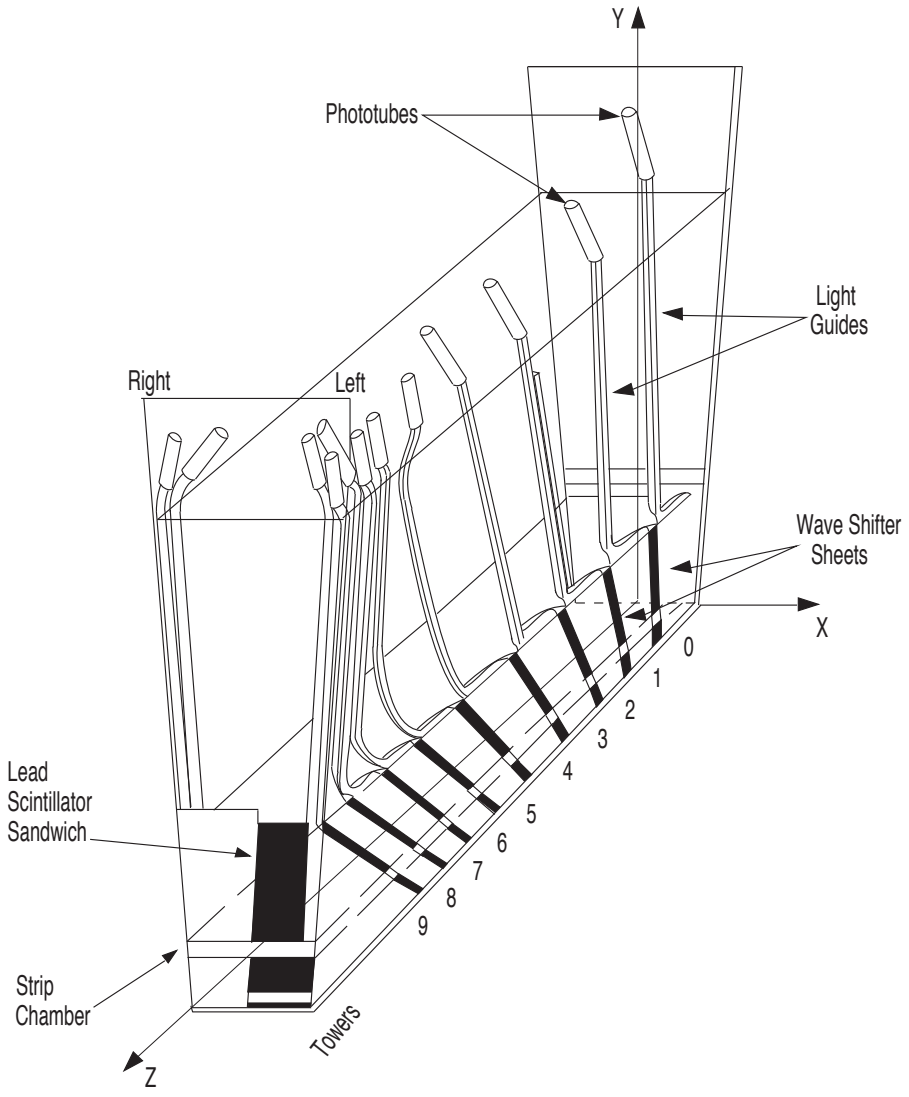

Figure 3.10: A wedge of the CEM and its components.

The hadronic calorimeters use steel plates as absorbing layers. The active detectors are plastic scintillators in the central region and the towers are read out in one

[6]In the energy resolution, the first term is the energy dependent term and the second is a constant term. They are added quadratically.

sample. The energy resolution of the hadronic calorimeters is:

$$\frac{\sigma(E)_{HAD}}{E} = \frac{75\%}{\sqrt{E_T}} \oplus 3\%$$

and the position resolution is for the $x-$direction and $y-$direction respectively, σ_x=10 cm and σ_y=5 cm

Plug Calorimeter

The plug calorimeter ($1.1 < |\eta_{det}| < 3.6$) is based on a similar design to that of the central calorimeters. It consists of a lead-scintillator electromagnetic section followed by an iron-scintillator hadronic section, arranged in 23 layers. It covers 0.1 units of η by 5° in ϕ.

The main two parts of the plus calorimetry are the *Plug Electromagnetic (PEM)* and the *Plug Hadronic (PHA)* calorimeters. Additional scintillator tiles and strips provide shower measurements for electron to pion separation and photon identification. The energy resolution for the PEM is:

$$\frac{\sigma(E)_{PEM}}{E} = \frac{16\%}{\sqrt{E_T}} \oplus 1.\%$$

and for the PHA:

$$\frac{\sigma(E)_{PHA}}{E} = \frac{80\%}{\sqrt{E_T}} \oplus 5\%$$

3.2.4 Muon Chambers

The muon chambers are located in the outer part of the CDF detector. The muons are identified by taking advantage of the fact that they are minimum ionizing particles that lose only modest quantities of energy when passing through large amounts of matter. Muon detection is made by positioning drift chambers behind the calorimeters and in some cases behind additional shielding. The majority of particles produced in $p\bar{p}$ collisions reaching these detectors are muons with a relatively small contamination from hadronic particles.

The muon chambers cover a region of $|\eta| < 2$. The muon chamber components and the coverage they provide is pictured in Figure 3.11.

The *Central Muon Detector (CMU)* covers the region $|\eta| < 0.6$. It is made of single wire drift chambers arranged in 4 concentric layers that provide a maximum of four measurement points per incoming muon candidate. The wires are strung

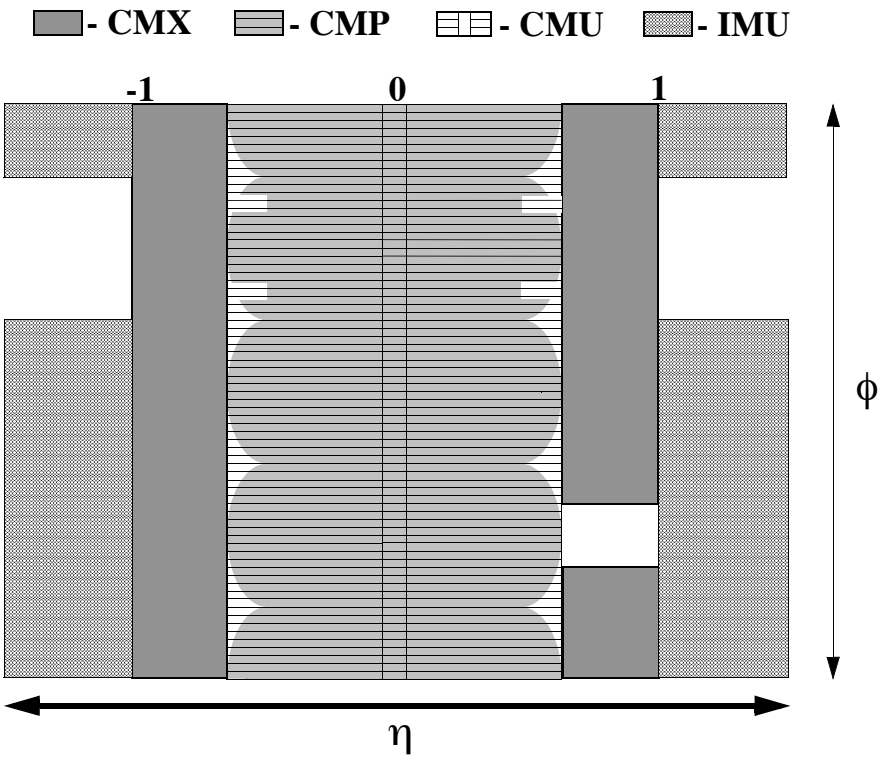

Figure 3.11: Map of the muon chambers $\eta - \phi$ coverage.

parallel to the beamline, thus providing axial position measurements. Behind the CMU chambers, additional similar wire chambers are placed, forming the *Central Muon Upgrade (CMP)* detector. The CMP covers the region $|\eta| < 0.6$ and provides 4 additional (to the CMU) measurement points in this eta region. In order to reduce the hadronic background, steel plates are placed between the CMU and the CMP. The CMU can detect a muon of $p_T > 1.4$ GeV/c and the CMP can detect a muon with $p_T > 2.2$ GeV/c.

The η region $0.6 < |\eta| < 1$ is instrumented with similar chambers that compose the *Central Muon Extension (CMX)* detector. The CMX provides 8 measurement points in total. No additional shielding is required for the CMX since the particles that reach the detector must traverse the calorimeter at a large angle, and thus reducing the hadronic background. The minimum momentum for a muon to reach the CMX is 1.7 GeV/c. The layout of the CMX detector is shown in Figure 3.12.

The forward region is instrumented with additional muon chambers, up to $\eta = 2.0$. The *Intermediate MUon (IMU)* detector is designed to trigger on muons with

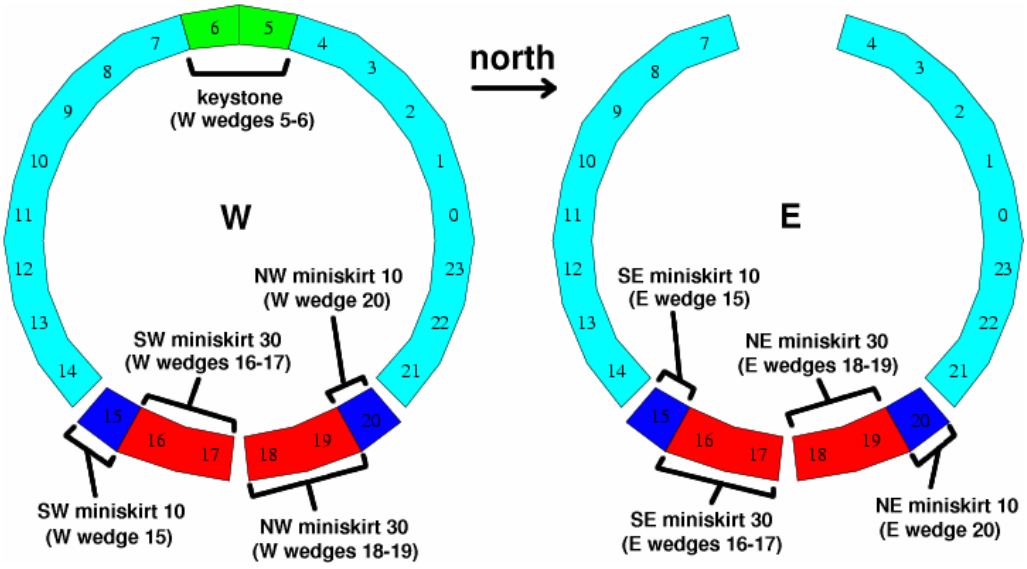

Figure 3.12: CMX wedge layout, end view. For the Run II of CDF, the gaps in ϕ have been instrumented with the *miniskirts* and the *keystone*, that use chambers similar to the rest of the CMX detector.

$1 < |\eta| < 1.5$ and identify offline muons with $|\eta| < 2.0$. It consists of CMP-like chambers and scintillation counters.

3.2.5 Luminosity Counters

The *Cherenkov Luminosity Counters (CLC)* system [20] is used to measure the luminosity of the $p\bar{p}$ interactions at the CDF interaction point. It is made of gaseous Cherenkov counters located at each end of the CDF detector, covering the pseudorapidity range $3.6 < |\eta| < 4.6$. The counters carry photomultipliers that detect the Cherenkov ultraviolet light emitted by charged particles traversing them. Measuring the inelastic collisions using the CLC, the instantaneous luminosity of the colliding beam can be extracted using an independent measurement of the inelastic cross section and a measurement of the CLC acceptance.

The uncertainty in the inelastic cross section ($\pm 4\%$) is the main uncertainty in the luminosity measurement. The uncertainty in the measured interactions rate comes from uncertainties in the CDF geometry simulation and the Monte Carlo simulation used for the CLC, and is less than $\pm 4.2\%$. The two uncertainties, added quadratically, give a $\pm 6\%$ uncertainty in the luminosity measurement. The accuracy of the measurement can not be significantly improved for the current method used

for the luminosity measurement, since the error is dominated by the inelastic cross section uncertainty [21].

3.3 Triggers and Data Acquisition System

The rate of collisions at the Tevatron (2.5 MHz) is too high for each event to be recorded for permanent storage. Given that only a small fraction of the inelastic $p\bar{p}$ collisions produce events of interest, the hadron colliders are equipped with a system capable of analyzing events in real time, selecting those worthy of further studies and storing them for subsequent analysis. This is the role played by the trigger and data acquisition system. The trigger system of the CDF experiment is made of three levels with increasing level of sophistication for event analysis and processing time. The diagram shown in Figure 3.13 summarizes the system [22].

The block diagram of the CDF trigger system is presented in Figure 3.14. The input to the Level 1 hardware comes from the calorimeters, tracking chamber and muon detectors. The decision to retain an event is based on the number and energies of electron, muon and jet candidates, as well as the missing transverse energy of the event. Events accepted by the Level 1 system are processed by the Level 2 hardware. All the information used in the Level 1 decision is available to the Level 2 system, but with higher precision; improved identification of electrons and photons is achieved and jets are reconstructed by the Level 2 cluster finder. Data from all the detectors arrive at the Level 3 farm for further processing.

Level 1 Trigger

The Level 1 trigger is made of custom hardware and is optimized for speed. The data for each bunch crossing are recorded and stored in a pipeline where it stays for 4 μs, the maximum time available for the Level 1 trigger to make a decision to accept or reject the event. Information from various detector systems are combined by the Level 1 trigger. The decision is sent to the front-end detector electronics and if accepted the event data are sent to Level 2 for further analysis.

The COT tracking, calorimeter, and muon detectors information is available at Level 1. Evidence for the presence of muons is obtained by looking for aligned hits in the CMU and CMX that are consistent in arrival time. Hits in the CMP are reconstructed based on the hits found in the CMU. Jets and electrons are reconstructed as a total and electromagnetic calorimeter energy deposited in a trigger tower (defined as two physical towers adjacent in η_{det}) above a given threshold.

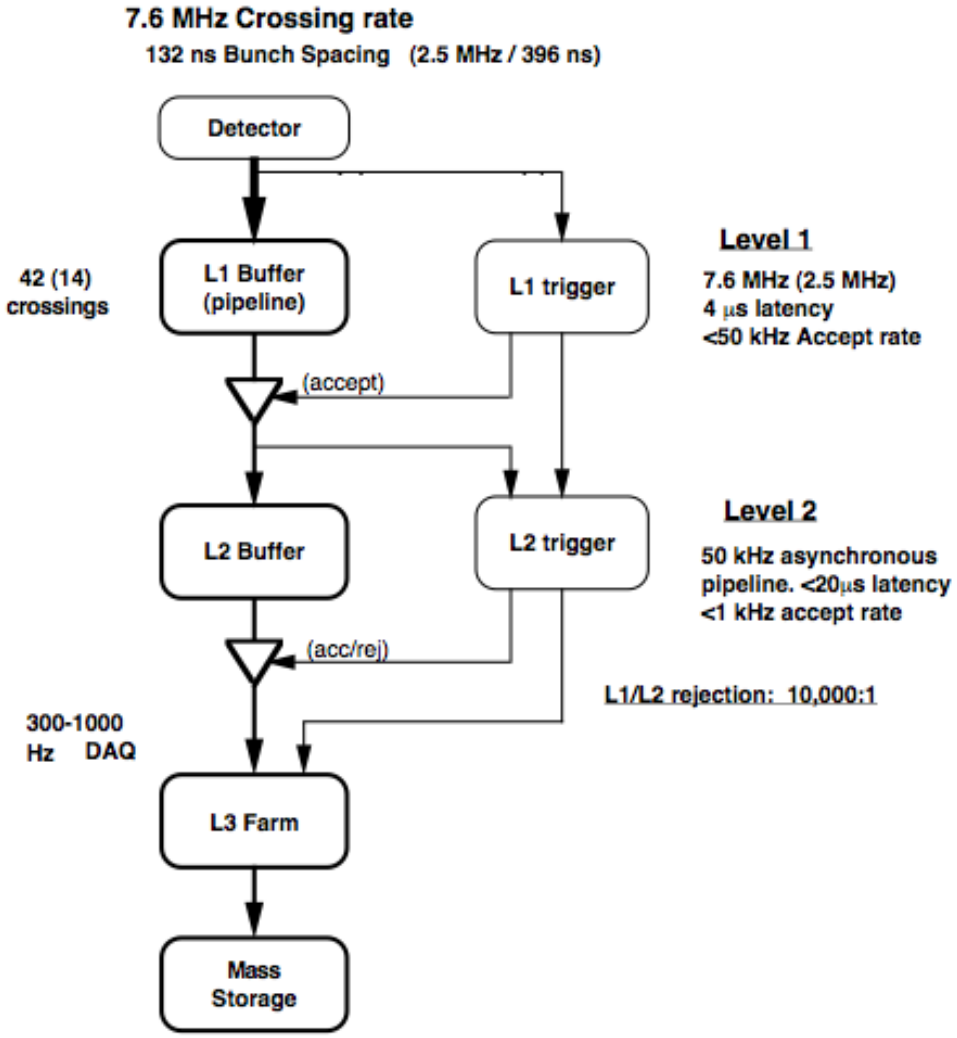

Figure 3.13: Dataflow for the CDF detector trigger and DAQ systems. The front ends buffer the data in 4μs pipelines while the Level 1 trigger processes the data and makes a trigger decision. For each level 1 accept the data are stored in a L2/DAQ buffer while the Level 2 trigger works. A Level 2 accept initiates the readout of the event data into the Level 3 processor farm. Following a Level 3 accept the data are written to disk/tape.

Missing transverse energy and the sum of the energy deposited in the calorimeters are also computed. Limited charged particle tracking is performed by the *eXtremely Fast Tracker (XFT)*, which examines hits only in axial superlayers of COT. Track segments are formed in each superlayer that are later linked together to form track

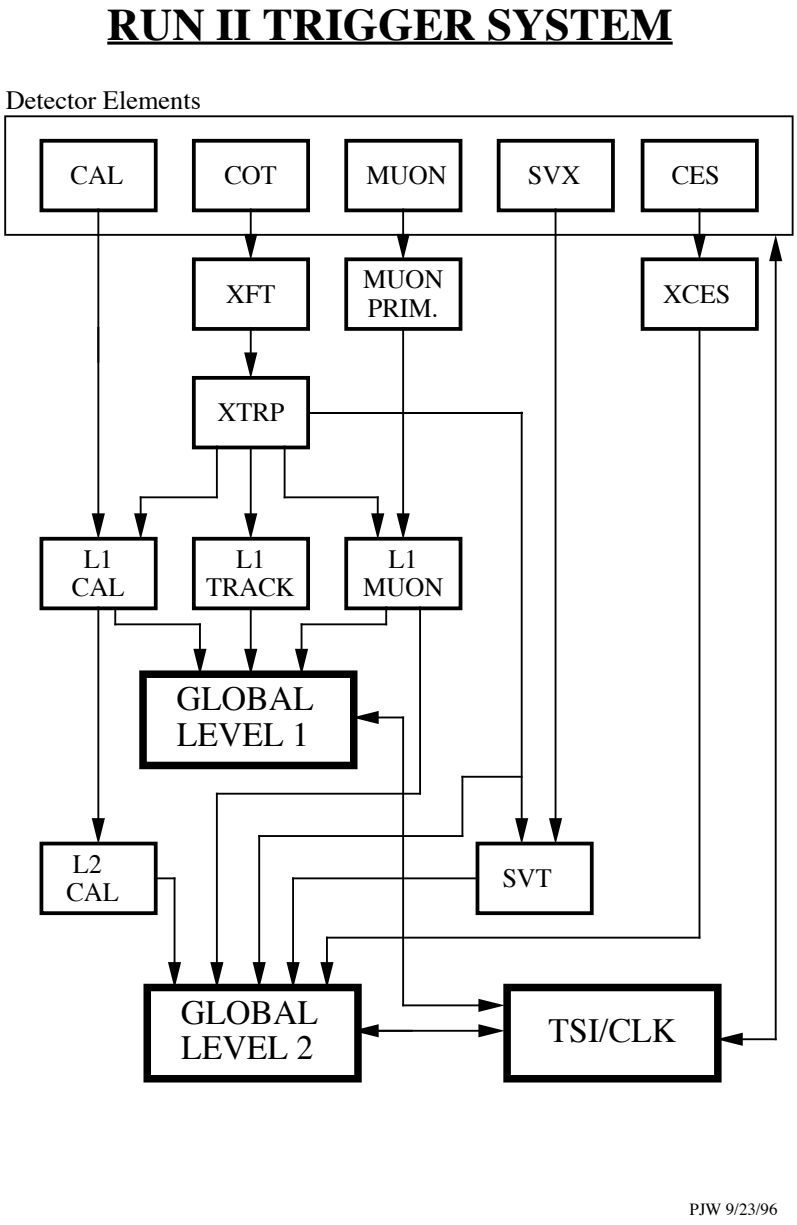

Figure 3.14: The Run II trigger system block diagram.

candidates. The presence of 10 or 11 hits per track segment (depending on the data-taking period) and the presence of track segments in each four axial superlayers are required. A *Track Extrapolation Unit (XTRP)* extrapolates the track candidates to the calorimeters and muon detectors to form electron and muon candidates. This information is collected together with the calorimeter trigger level information to make the Level 1 decision. The input event rate to the Level 1 trigger is 2.5 MHz

(corresponding to the bunch crossing rate) and the maximum output rate is 20 kHz, dictated by the Level 2 processing time of about 50 μs per event.

Level 2 Trigger

The data from Level 1 are stored in one of four event buffers that stores them until the Level 2 decision is reached. The Level 2 trigger is made of custom hardware and modified commercial processors. It is made of two main pieces of hardware: the *Secondary Vertex Trigger (SVT)* and the cluster finder hardware. The SVT uses silicon hit information, in conjunction with the XFT tracks, to trigger on the presence of tracks from displaced vertices. The cluster finder forms cluster of energies from neighboring calorimeter towers as defined by the Level 1 trigger, to form more sophisticated electron and jet candidates. The data from these systems as well as the data used for the Level 1 decision are sent to the Level 2 processor crate to make the decision. If accepted, the event data are read from the buffer and set to the Level 3 trigger. The maximum Level 2 accept rate is 300 Hz.

Level 3 Trigger

The Level 3 trigger is implemented as a farm of roughly 300 commercial dual processors connected by high-bandwidth networks to the digital readout and storage devices. The processors run a version of the offline CDF reconstruction algorithms that is optimized for speed. The processing time is about one second per event. Events are accepted by Level 3 at a maximum rate of about 75 Hz. The data for accepted events are sent to permanent storage for subsequent processing by the full offline reconstruction algorithms.

3.4 Summary

In this chapter, the Fermilab accelerator chain is summarized and the CDF detector and trigger system are described. The performance of both the accelerator and the CDF detector have been exceptional. More than 3 fb^{-1} of integrated luminosity has been delivered at CDF so far (early 2008). The Tevatron will continue running until 2009. A total of 6-8 fb^{-1} is expected be accumulated until then.

Chapter 4

Event Reconstruction and Selection

The disobon production in the semileptonic decay channel, contains signatures of leptons, neutrinos and quarks. Inside the detector, the leptons are reconstructed in the calorimeter and muon chambers, the neutrinos are identified as missing transverse energy ($\not\!\!E_T$) in the calorimeter and the quarks, that hadronize, generate jets of particles that leave their signatures in the calorimeter (Figure 4.1).

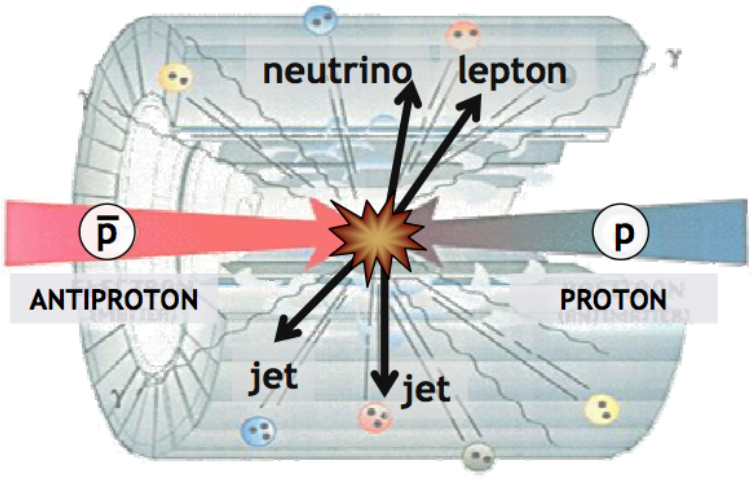

Figure 4.1: The semi-leptonic signature of the WW/WZ production: a lepton, a neutrino (identified as missing transverse energy) and jets, generated by the quark hadronization.

In this chapter we will describe the reconstruction of the objects we'll use in the analysis, including the requirements applied during data taking by the trigger system and the final candidate event selection criteria. A schematic description of

the reconstruction of the objects used in this analysis is shown in Figure 4.2.

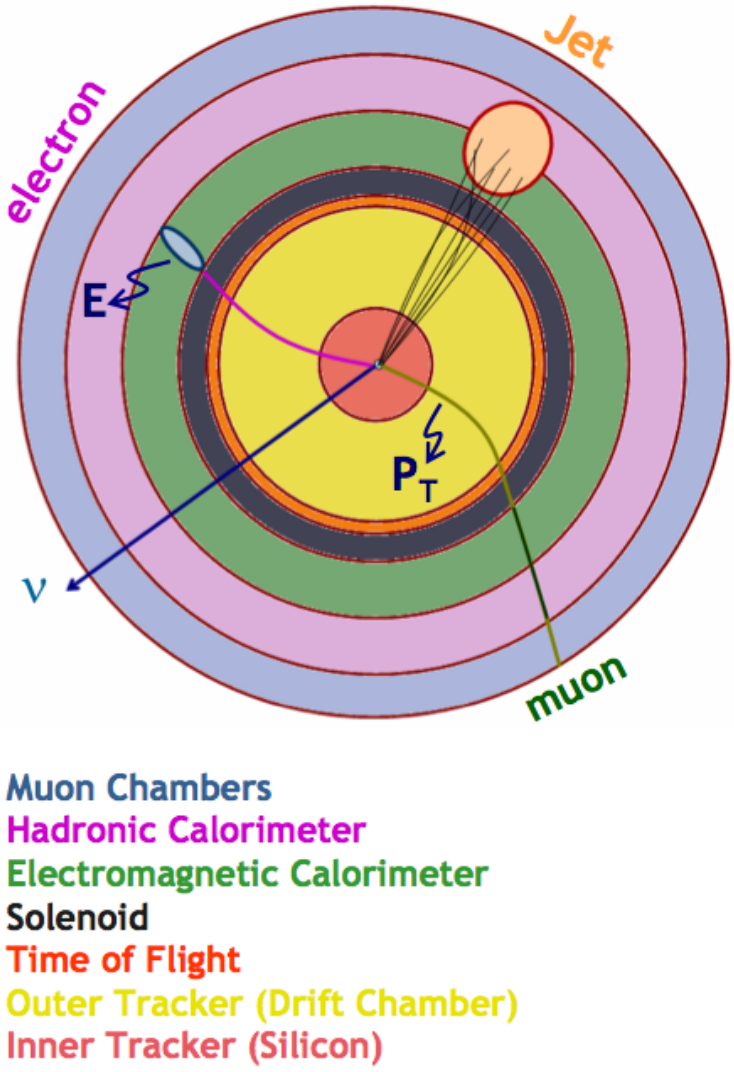

Figure 4.2: A schematic description of the reconstruction at the CDF detector of the objects used in the analysis: electrons, muons, neutrinos and jets.

4.1 General

Dataset

The datasets used in this analysis are data taken from February 2002 to September 2006 (9 periods of data). The data are divided in three sub-datasets: $0d$, corresponding to *period 0*, $0h$, corresponding to *periods 1-4* and $0i$, corresponding to *periods 4-8*. The run numbers cover the interval 138425 to 222426 selected by the good run list version 16, Top/EWK/Exotics electrons and muons with no silicon requirements, which corresponds to an integrated luminosity 1.2 fb^{-1}. For this analysis the offline CDF software has been used, more specifically the *StNtuple* package release 6.1.4.

The signal definition

The decay channel of this analysis contains three objects: the *charged lepton* (electron or muon)[1], the *neutrino* (missing transverse energy, $\not\!\!E_T$), and the *jets*.

The theoretical cross sections for this decay mode are ([5], [2])

$$\sigma_{WW} \times Br(W \to \ell\nu_\ell, W \to jj) = (12.4 \pm 0.8) \text{ pb} \times 0.146 = 1.81 \pm 0.12 \text{ pb}$$

$$\sigma_{WZ} \times Br(W \to \ell\nu_\ell, Z \to jj) = (4.0 \pm 0.3) \text{ pb} \times 0.07 = 0.28 \pm 0.02 \text{ pb}$$

The total cross section in the Standard Model of the signature we are looking for is therefore

$$\sigma_{WW/WZ} \times Br(W \to \ell\nu_\ell, W/Z \to jj) = (2.09 \pm 0.14) \text{ pb}$$

The background definition

There are several processes that result in the same final state topology (1 charged lepton, electron or muon, $\not\!\!E_T$ and jets) as the diboson production, and thus are backgrounds to this search. The background processes that are taken into account are:

- $p\bar{p} \to W(\to \ell\nu_\ell) + jets;\ \ell = e,\ \mu$
  In this case, generic QCD jets fake a hadronically decaying W. The production

[1] The tau is difficult to reconstruct at a hadron collider because the tau decay has one or two additional neutrinos. It is reconstructed by its hadronic or leptonic decays, the reconstruction is therefore not clean, but followed by large backgrounds (since many processes have the same signatures).

cross section of this process is more than 200 pb ($W(\rightarrow e\nu_e)+ \geq 2\ jets$, [27]).

- $p\bar{p} \rightarrow W(\rightarrow \tau\nu_\tau) + X$
  A tau is detected as an electron or a muon. The $W \rightarrow \tau\nu$ inclusive cross section is 2780 pb [28]. Requiring jets in the process drops the cross section to a value comparable to the $W(\rightarrow e\nu)+ \geq 2\ jets$ cross section.

- $p\bar{p} \rightarrow Z(\rightarrow \ell\ell) + X;\ \ell = e,\ \mu$
  One of the two leptons is not reconstructed, resulting in larger missing transverse energy (e.g. because it fell in un-instrumented areas of the detector). The cross section for the inclusive process is 497.42 pb [28].

- *QCD processes*
  A QCD jet fakes a lepton. The QCD processes are larger background for a $W \rightarrow e\nu$ than for a $W \rightarrow \mu\nu$.

- $p\bar{p} \rightarrow t\bar{t} + X,\ t \rightarrow Wb$
  The W (either leptonic or hadronic) comes from $t\bar{t}$ production. The process has a cross section of 6.7 pb.

The largest of these backgrounds is the $(W \rightarrow \ell\nu)$+jets. The large cross section of this process leads by itself, but even more with the rest of the backgrounds, to a very poor Signal over Background ratio ($S/B < 1\%$ initially).

The objects reconstruction

In order to study the signal and the background of the process of interest using the CDF detector data, the information from the detector needs to be processed and interpreted into physical objects (electrons, neutrinos, jets). The first step of the processing is performed online, via the CDF data acquisition and trigger system. Once the interesting data, containing electron and jet candidates and $\not\!\!E_T$ information, is stored on disks, offline selection algorithms are used to reconstruct the final objects that will be used in the analysis.

4.2 Trigger Requirements

At the trigger level, one attempts to select signal events with high efficiency while keeping the trigger accept rate low, rejecting many background events. It is possible to meet these criteria in this analysis by exploiting only one of the characteristics

of the signature: the presence of centrally produced electrons and muons with high transverse momentum (p_T).

4.2.1 Central Electron Trigger

The trigger path $ELECTRON\_CENTRAL\_18$ is used to select centrally produced high-p_T electrons. Below are listed the trigger requirements for the three trigger levels. The requirements have been stable through the data taking and the different run periods. The trigger efficiency[2] is $\epsilon_{trigger} = 0.962 \pm 0.006$ for period $0d$ and $\epsilon_{trigger} = 0.977 \pm 0.006$ for periods $0h\&0i$ [31].

- Level 1 Trigger
  - Energy deposit of a minimum 8 GeV in the calorimeter tower;
  - Ratio of energy deposited in the hadronic and electromagnetic sections of the calorimeter (E_{had}/E_{em}) required to be less than 0.125 to reject hadronic particles;
  - A track with $p_T > 8$ GeV/c found by the XFT is required to point to the tower.
- Level 2 Trigger
  - A calorimeter cluster is formed by adding adjacent towers with $E_T >$ 7.5 GeV to the "seed" tower found at Level 1;
  - For the cluster, the requirements are $E_T > 16$ GeV and E_{had}/E_{em} <0.125;
  - The Level 1 XFT requirement is confirmed.
- Level 3 Trigger
  - An electromagnetic cluster with E_T >18 GeV and $E_{had}/E_{em} < 0.125$ is required;
  - A fully reconstructed three-dimensional COT track with $p_T > 9$ GeV/c is required to point to the cluster.

[2] All errors in the trigger efficiencies are statistical.

4.2.2 Central Muon Trigger

Two trigger paths are used for the central muon selection. One finds the muons in the CMU and CMP ($|\eta_{det}| < 0.6$) and is called $MUON\_CMUP\_18$ and the other in the CMX ($0.6 < |\eta_{det}| < 1.0$) and is called $MUON\_CMX\_18$. The efficiency for the CMUP trigger is $\epsilon_{trigger} = 0.902 \pm 0.004$ for the $0d$ period and $\epsilon_{trigger} = 0.919 \pm 0.004$ for the $0h\&0i$. For the CMX, the trigger efficiency is $\epsilon_{trigger} = 0.967 \pm 0.004$ for the $0d$ period and $\epsilon_{trigger} = 0.955 \pm 0.004$ for the $0h\&0i$. Below, the trigger selection is explained.

- Level 1 Trigger
  - Hits in one or more layers of the CMU or CMX are found;
  - For the CMU/CMP trigger, 3 or 4 additional hits in the CMP are found and required to be consistent with hits in the CMU;
  - An XFT track with p_T >4 GeV/c (8 GeV/c) is demanded to match in the $r - \phi$ plane the hits found in the CMU/CMP (CMX).
- Level 2 Trigger
  - No additional requirements in general. In certain run periods a requirement of a COT track with $p_T > 8$ GeV/c was added. In periods of high luminosity this was essential for the good muon identification.
- Level 3 Trigger
  - A fully reconstructed three-dimensional COT track with $p_T > 18$ GeV/c is required to match the tracks reconstructed in the muon chambers.

4.3 Offline Reconstruction

The offline reconstruction concerns the events of the dataset that have been selected by any of the triggers mentioned above: $ELECTRON\_CENTRAL\_18$, and/or $MUON\_CMUP\_18$, and/or $MUON\_CMX\_18$. In these events, the objects of the analysis will be reconstructed. A first step in the reconstruction of the objects we are interested in for this analysis is the reconstruction of a *track* that is essential for the lepton identification.

4.3.1 Track Reconstruction

The track reconstruction of charged leptons is essential for the lepton reconstruction. Tracking information at CDF comes from the silicon detectors and the COT chambers. For reconstructing the central lepton the information from the COT chambers is sufficient and the COT tracking will be only described below. The silicon detector provides valuable information for vertex reconstruction in low p_T measurements (b physics) or when the COT η coverage is not sufficient (e.g. in plug lepton reconstruction).

COT tracking

The COT is able to reconstruct particle trajectories and their momenta up to $|\eta| = 1$. The reconstruction algorithm (*pattern recognition algorithm* [23]) is described below.

In each of the superlayers (axial or stereo), hits in three consecutive wires are grouped and fitted to a straight line. These segments are used as "seeds". Other hits in the superlayer within a distance of ≈ 1 mm from the segment are added to the straight line fit using an iterative procedure.

Two separate algorithms are used to form axial-only tracks: the *segment linking* algorithm links track segments between axial superlayers while the *histogram linking* algorithm performs a circle fit that adds axial hits starting from a seed track segment. Tracks found by both algorithms are merged together and track duplicates are removed. Hits in the stereo layers are added using a three-dimensional fit of the helical trajectory of the track.

Finally, tracks are refitted to take into account material effects and variations in the value of the magnetic field. In the last fit, the tracks are forced to originate from the beamline in the x-y plane to improve the momentum resolution.

The track reconstruction efficiency for tracks with $p_T > 10$ GeV is $\approx 97\%$. The efficiency itself is not used in the analysis, instead a scale factor that compares the track reconstruction efficiency of the data with respect to the Monte Carlo, is used. This scale factor is 1.009 ± 0.002 for the $0d$ period [32] and 1.014 ± 0.003 for the periods $0h\&0i$ [33]. The error includes statistics and systematics. The systematic error comes from the methodology used for the efficiency estimation.

4.3.2 Lepton Reconstruction

Track requirements

The central electrons and muons candidates have good track segments on three axial and two stereo superlayers. A *good track segment* is defined as containing at least 5 hits out of the possible 12 in the superlayer. In order to have good COT tracking efficiency we require the z coordinate of the track trajectory to be less than 60 cm away from the center of the CDF detector.

Additional track requirements are applied to the muon selection, to remove background events from cosmic rays and pion and kaon in flight decays. The tracks are required to originate from the center of the detector in the x-y plane and an upper limit (run dependent) is set for the χ^2 of the beam constrained fit over the number of degrees of freedom (χ^2/ndf). The cosmic background is mostly reduced by requiring the track hit timing information to be consistent with the bunch crossing for that event. Finally, the radius at which the track exits the COT is required to be greater than 140 cm to avoid regions where the muon reconstruction is not well-understood.

Central electrons

The reconstruction of central electron candidates begins by forming electromagnetic clusters in the CEM ($|\eta| < 1$). The cluster is made of a maximum of two adjacent towers in η and the sum of their transverse energy is required to be greater than 20 GeV. A COT track with $p_T > 10$ GeV/c is required to point to the most energetic tower of the cluster (seed tower). We demand the cluster to have $E_{had}/E_{em} < 0.055 + 0.00045E$ (Figure 4.3) where E is the total energy of the cluster in GeV to reject candidates that arise from hadrons faking an electron. The energy dependence of this cut ensures a high efficiency for real electrons over a large energy range. Similarly, high efficiency for real electrons and hadronic background reduction is ensured with an E_T dependent cut on the ratio of the cluster transverse energy and track p_T (E/p) ($E/p < 2.5 + 0.015E_T$).

A cluster in the calorimeter is formed from the energy deposited on the wires of the CES chambers. The position of the CES cluster is required to match the COT track: -3.0 cm $\leq q \times \Delta X \leq 1.5$ cm (where ΔX is defined at the $r - \phi$ plane) and $|\Delta z| < 3.0$ cm.

Electrons produced in W boson decays are *isolated* from neutral and charged particles with respect to electrons produced in jets. We require the *isolation* (E_T deposited in the calorimeters in a cone of radius $\Delta R = \sqrt{\Delta\eta^2 + \Delta\phi^2} = 0.4$ around

the electron candidate) be less than 10% of the cluster E_T (Figure 4.4).

A summary of the central electron selection cuts is given in Table 4.1. The identification and reconstruction efficiency for the a single central electron is of the order of 80%. In this analysis the single electron efficiency isn't used, since the full selection acceptance will be estimated using Monte Carlo events, as will be explained in a later chapter. A data to Monte Carlo scale factor, derived from comparison of the electron efficiency in data and Monte Carlo, will be used to scale the selection acceptance. This scale factor is 0.991 ± 0.004 for the $0d$ period of data and 0.979 ± 0.010 for $0h\&0i$ ([30]). The uncertainties are derived from statistics and inaccuracies in the methodology used for their definition.

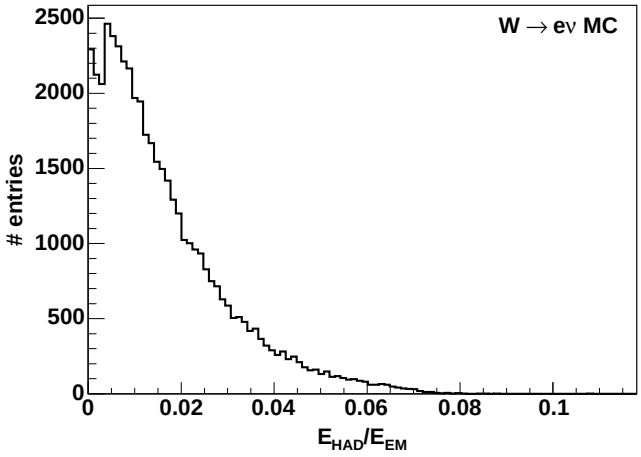

Figure 4.3: The electron E_{had}/E_{em} fraction in $W \rightarrow e\nu_e$ Monte Carlo events. No single cut requirement is set.

Central muons

Muons are identified by either a charged track matched to a reconstructed track segment ("stub") in the central (CMU and CMP) or extended (CMX) muon chambers. The stubs are formed by hits in the CMU, CMP and CMX and the extrapolated tracks are required to match the position of the stub in $r - \phi$ within 3, 5 and 6 cm in the CMU, CMP and CMX respectively. The energy deposited in the calorimeter by the candidate track is required to be consistent with that of minimum ionizing particles to remove fake hadronic particles. Similar isolation requirement as for the

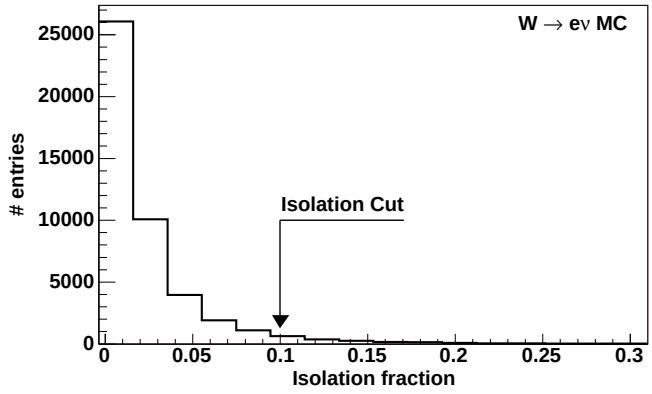

Figure 4.4: The electron isolation in $W \rightarrow e\nu_e$ Monte Carlo events.

Central Electron [35]	Region	Central
	Track	Yes
	Iso/E_T	≤ 0.1
	E_T	> 10 GeV
	P_T	> 10 GeV(> 5 GeV, if $E_T < 20$ GeV)
	Track $\lvert Z_0 \rvert$	≤ 60 cm
	E/P	$< 2.5 + 0.015 \times E_T$
	Had/Em	$\leq 0.055 + 0.00045 \times E$
	Signed CES ΔX	$-3 \leq q \times \Delta X \leq 1.5$ cm
	CES $\lvert \Delta Z \rvert$	< 3 cm
	Fiducial	Yes

Table 4.1: Electron Selection

electrons is applied for the muons, with the exception that the energy in the cone is compared to the track p_T instead of the cluster E_T.

As part of the muon stub selection, we apply cuts that ensure that the tracks reconstructed with the COT, point at regions of the muon chambers with high hit reconstruction efficiency. The projected position of the track in the x and z axes are compared to the muon chamber edges position. A negative value of the fiducial distance means that the track is projected to the inside of a chamber [29].

A summary of the central muon selection cuts is given in Table 4.2. The identification and reconstruction efficiency for the CMUP muons is of the order of 83% and for the CMX muons of the order of 91%. These efficiencies are not used in the analysis though, as described for the electron case, but it is a data to Monte Carlo scale factor that is used. For the CMUP muons the scale factor is 0.922 ± 0.006 for the $0d$ period of data and 0.918 ± 0.008 for $0h\&0i$. For the CMX muons, the values are 0.997 ± 0.006 for $0d$ and 0.979 ± 0.009 for $0h\&0i$.

Central Muon [35]	$\mathrm{Iso/P_T}$	≤ 0.1
	$\mathrm{P_T}$	> 20 GeV
	Track $\lvert \mathrm{Z_0} \rvert$	≤ 60 cm
	Track $\lvert \mathrm{D_0} \rvert$	≤ 0.2 cm (0.02 cm if Si Hits > 0)
	CMU Fid	$x - fid <$ 0 cm, $z - fid < 0$ cm
	CMP Fid	$x - fid <$ 0 cm, $z - fid < -3$ cm
	CMX Fid	$x - fid <$ 0 cm, $z - fid < -3$ cm
	E_{em}	$\leq 2 + max(0, (p - 100) * 0.0115)$
	E_{had}	$\leq 6 + max(0, (p - 100) * 0.028)$
	COT Ax hits / Ax Seg	$\geq 5 / \geq 3$
	COT St hits / St Seg	$\geq 5 / \geq 3$
	ρ_{exit}	> 140 cm if CMX
	$\lvert \Delta \mathrm{X_{CMU}} \rvert$	$\leq 3\ cm$
	$\lvert \Delta \mathrm{X_{CMP}} \rvert$	$\leq 5\ cm$
	$\lvert \Delta \mathrm{X_{CMX}} \rvert$	$\leq 6\ cm$
	χ^2/ndf COT (data only)	$< 2.75 (< 2.3\ if\ run\ >$ 186598)

Table 4.2: Muon Selection. The Fid labels refer to the cuts on the fiducial distances of the tracks from the muon chambers.

4.3.3 Jet Reconstruction

A jet is a collimated flow of hadrons produced by hard scattering processes, whose energy, mass and momentum can be related to a collection of partons. The jet, which we assume to be massless, is reconstructed as a cluster of calorimeter towers. A 4-momentum p_μ is assigned to it, as defined below. In order to associate the particles (hadrons) with jets, we use a selection process that we call the *jet algorithm*.

The algorithm that we use in this analysis is a *cone algorithm*. This term describes a procedure that intends to cluster all energy within a given radius R in the $\eta - \phi$ plane, to form a jet. The specific cone algorithm that we used is the "Jet Clustering Algorithm", or JETCLU [24].

Jet Clustering Algorithm

The JETCLU algorithm is an iterative algorithm that consists of the following steps.

- Create a list of calorimeter towers with $E_T > 1.0$ GeV, where

$$E_T = E_{EM} sin\theta_{EM} + E_{HAD} sin\theta_{HAD}$$

  where E_{EM} and E_{HAD} denote the energy measured in the electromagnetic and hadronic calorimeters respectively. The angles θ specify the location of the calorimeter cells with respect to a vertex position in z (Figure 4.5).

  These towers are called *seed towers*.

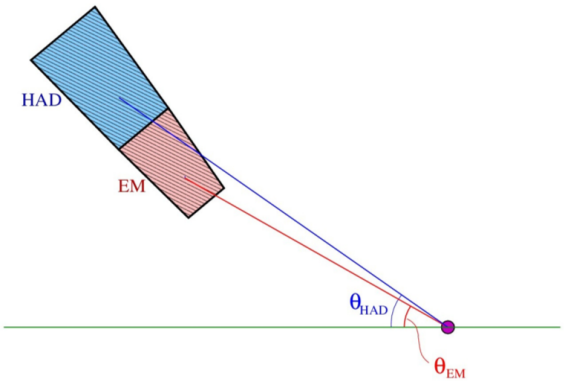

Figure 4.5: The calorimeter towers geometry for the *seed tower* definition.

- Starting with the highest-E_T seed tower, form *preclusters* by clumping together adjacent seed towers within a cone of radius R in $\eta - \phi$ space. Every seed tower is assigned to exactly one precluster and each precluster contains at least one seed tower.

- For each precluster find the E_T weighted centroid and draw a cone of radius R around it. A *cluster* consists of all towers within the cone that have $E_T >$ 0.1 GeV.

- Iteratively recalculate the cluster centroid, draw a new cone and add towers until the tower list remains unchanged or the number of iterations reaches a maximum number.

  The jet cone will always contain the original seed towers that originate it (precluster), even if the subsequent clustering steps place the seeds outside

the stable jet cone. This is called *ratcheting* and with it, a cluster may contain towers that are no longer within the cone.

The advantage of ratcheting is that it prevents that energy associated with hard scattering is finally unclustered in any of the jets. However, this procedure cannot be modeled theoretically and the algorithm is not infrared safe[3] and collinear safe[4].

- The overlapping clusters are treated as follows:
  - If the towers of one cluster are completely contained within the other, the smaller of the two is dropped
  - If the tower lists of different clusters partially overlap, an *overlap fraction* is computed by summing the E_T of the common towers and dividing the total by the E_T of the smaller cluster. If the fraction is above a cutoff, the two clusters are combined. Otherwise, the clusters remain separate and each tower is assigned to the cluster with the nearest centroid in $\eta - \phi$.
- The final cluster is a *jet*, defined by the tower list.

The general principle of a cone algorithm, together with the jet development at the detector, are shown in Figure 4.6.

Generic Jet Corrections at CDF

In the CDF experiment there is a dedicated group, the jet energy group, whose primary goal is to determine the energy correction to scale the measured energy of the jet energy back to the energy of the final state particle level jet. Additionally, there are corrections to associate the measured jet energy to the parent parton energy, so that direct comparison to the theory can be made [25].

The CDF jet energy corrections are divided into different levels to accommodate different effects that can distort the measured jet energy, such as, response of the calorimeter to different particles, non-linearity response of the calorimeter to the particle energies, un-instrumented regions of the detector, spectator interactions, and energy radiated outside the jet clustering algorithm. Depending on the physics analyses, a subset of these corrections can be applied.

Below, the jet corrections are summarized:

[3] *Infrared safe* is the jet whose properties do not depend on the presence of arbitrarily soft partons.

[4] *Collinear safe* is the jet whose properties are insensitive to partons radiated collinearly.

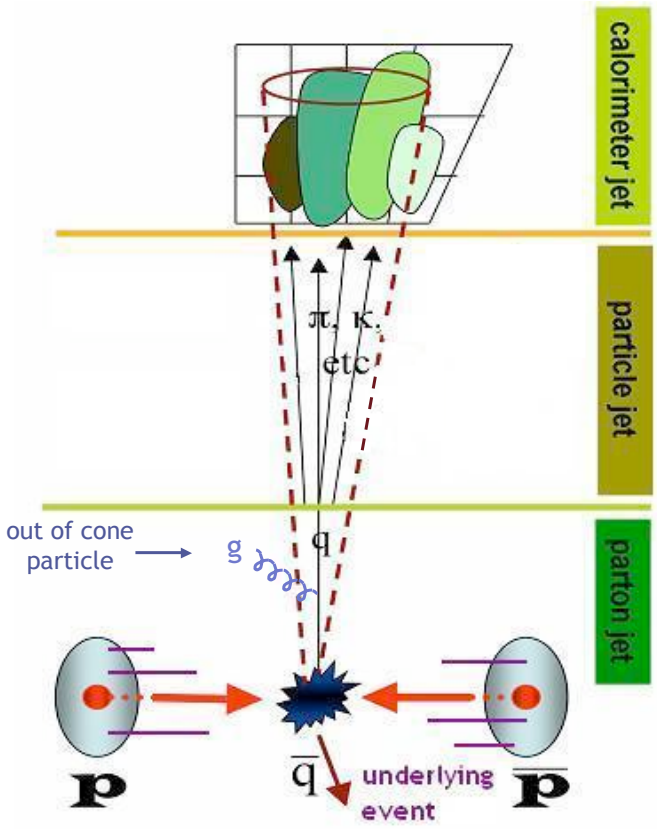

Figure 4.6: A schematic description of the jet reconstruction, based on the development of the jet: from flow of partons (partonic jet) to stream of particles (hadronic jet) to the measured jet (calorimeter jet).

- 'Level 0' or *Online/Offline Calibrations*; This correction sets the calorimeter energy scale. The effect is small ($\approx 3\%$).

- 'Level 1' or *Eta-dependent*; It is applied to raw jet energies measured in the calorimeter to make jet energy uniform along eta. It is an effect that clearly depends on the detector geometry and varies with η. Variations are as large as 20%. The uncertainty in the correction is η and p_T dependent and varies from 0.1% to 3%.

- 'Level 4'[5] or *Multiple Interactions*; The energy from different $p\bar{p}$ interactions

[5]The corrections Level 2 (time dependence of calorimeter photomultipliers) and Level 3 (Run I - Run II differences) were used in early runs. Currently they are covered in other corrections and

during the same bunch crossing falls inside the jet cluster, increasing the energy of the measured jet. This correction substracts this contribution in average. The correction is derived from minimum bias data and it is parameterized as a function of the number of vertices in the event. The correction is small (less than 1%).

- 'Level 5' or *Absolute Corrections*; Corrects the jet energy measured in the calorimeter for any non-linearity and energy loss in the un-instrumented regions of each calorimeter. The effect is p_T dependent. The correction factor is about 1.35 for p_T of 20 GeV and reduces to 1.1 for high-p_T jets (Figure 4.7). The uncertainty is also p_T dependent, and shown in the Figure.

- 'Level 6' or *Underlying Event Corrections*; The underlying event (UE) is defined as the energy associated with the spectator partons in a hard collission event. Depending on the details of the particular analysis, this energy needs to be subtracted from the particle-level jet energy. A factor 1.6 is used to take this into account. The uncertainty is 30% of the underlying event correction.

- 'Level 7' or *Out of Cone Corrections*; It corrects the particle-level energy for leakage of radiation outside the clustering cone used for jet definition, taking the 'jet energy' back to 'parent parton energy'. The correction is cone size dependent and jet p_T dependent (Figure 4.8). The uncertainty is also p_T dependent, and shown in the Figure.

The corrections Level 6 and 7 bring the jet energy scale to parton level energy scale. The rest of the corrections bring the jet energy to particle level energy scale.

The quantification of the corrections and their uncertainties described above refer to a jet cone size of 0.4. The corrections and their systematics become more significant for larger cone size (e.g. for the underlying event systematic uncertainties, Figure 4.9).

4.3.4 Missing Transverse Energy ($\not\!\!E_T$)

The $\not\!\!E_T$ is first introduced in a previous section (3.2.1). The $\not\!\!E_T$ is defined as

$$\not\!\!E_T = |\sum_i E_{T,i}\hat{n}_{T,i}|$$

not applied anymore.

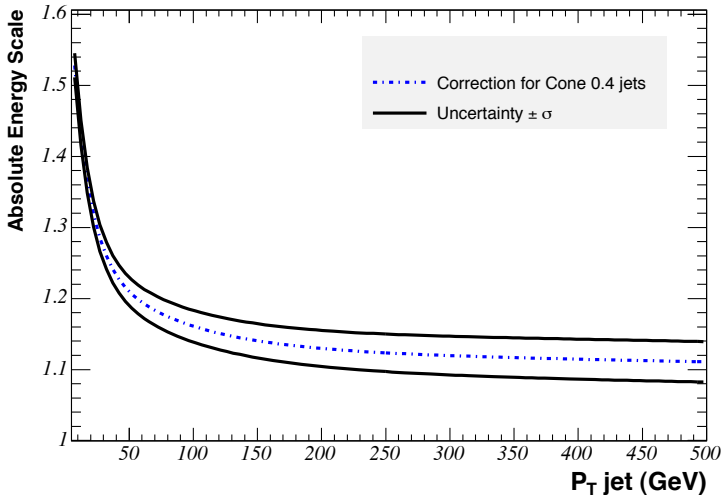

Figure 4.7: Absolute energy scale as a function of the jet p_T. The uncertainties due to this correction are also shown in the plot (from [25]).

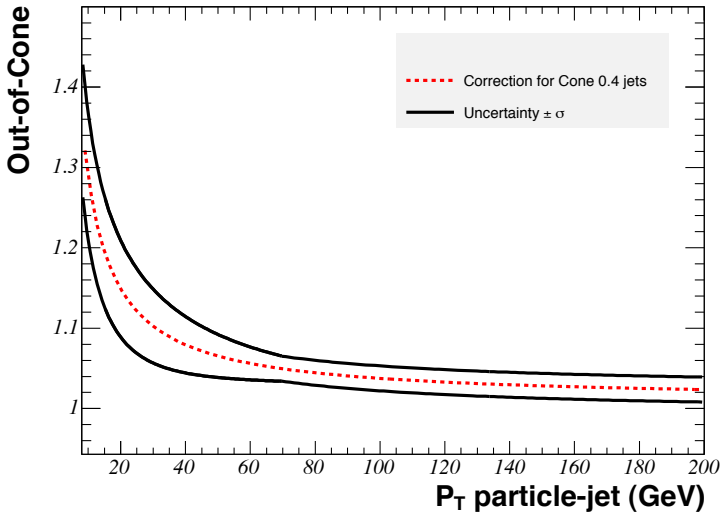

Figure 4.8: Out of cone correction factor as a function of the jet p_T. The uncertainties due to this correction are also shown in the plot (from [25]).

where the sum is over all the calorimeter towers and $\hat{n}_{T,i}$ is the transverse component of the unit vector pointing from the interaction point to the calorimeter tower i.

The $\not\!\!E_T$ is corrected for the muons that do not leave much of their energy in the calorimeter. It is also corrected for the jets, which are taken into account in

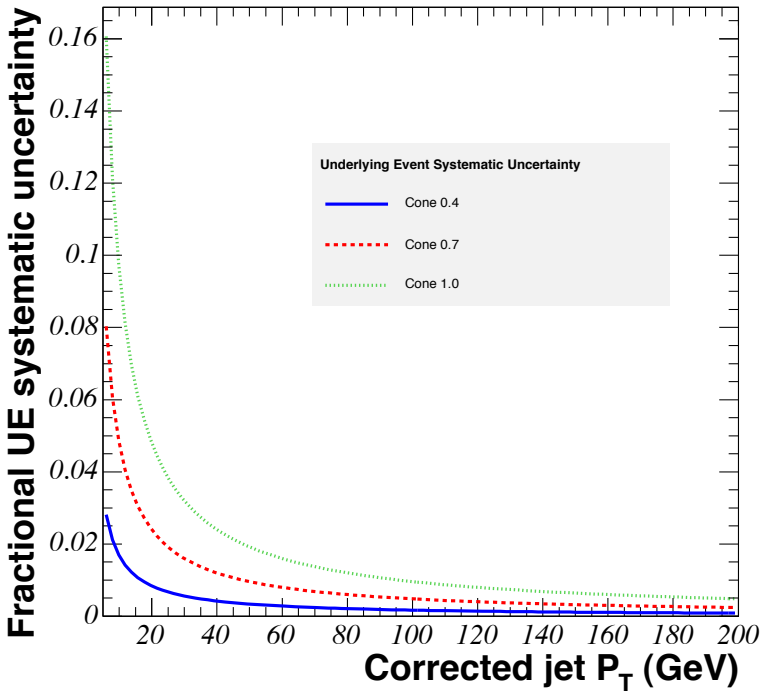

Figure 4.9: Underlying event correction systematic uncertainties as a function of the jet p_T, for various jet cone size (from [25]).

the $\not\!\!E_T$ calculation without corrections, but in a tower by tower basis. For the jet corrections in the $\not\!\!E_T$, the uncorrected jet energy is subtracted by the $\not\!\!E_T$ and the corrected up to level 5 (detector level) jet energy is added:

$$\not\!\!E_T = \not\!\!E_T{}^{raw} - \sum_{i=1}^{NJets} E_{T_i}^{uncorr.} + \sum_{i=1}^{NJets} E_{T_i}^{corr.}$$

The effect of the corrections is significant, especially in events with high jet multiplicity and muons, and it affects not only the $\not\!\!E_T$ absolute value but also the shape.

4.4 Event Selection

In order to study the semileptonic decays of WW and WZ production, we select events that have:

- Exactly one lepton, central electron or central muon. The definition of these objects is given in Tables 4.1 and 4.2.

- $\not\!\!E_T$ >25 GeV, as demonstrated in Figure 4.10.

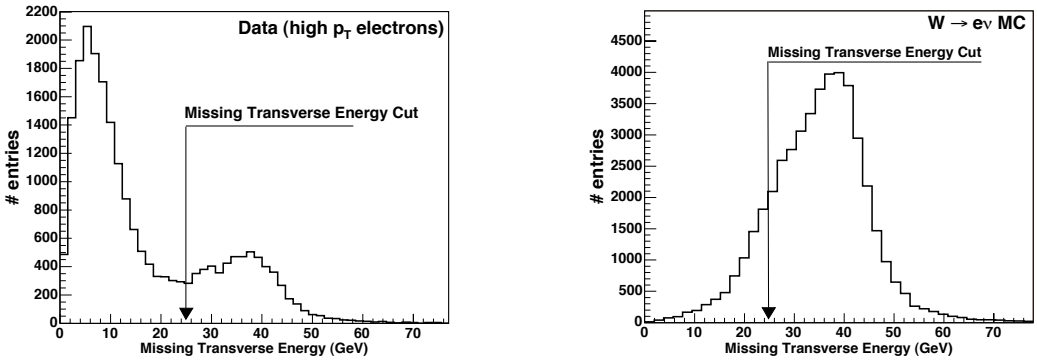

Figure 4.10: The $\not\!\!E_T$ distributions for data and $W \rightarrow e\nu_e$ Monte Carlo. The $\not\!\!E_T$ cut is set at 25 GeV. Below that value, the background dominates (as seen on data).

The $\not\!\!E_T$ selection used in the analysis is summarized in Table 4.3.

$\not\!\!E_T$	Value	> 25 GeV
	Muon Correction	Yes
	Jet Correction	$P_T^{Jet} > 8$ GeV, then corrected L5

Table 4.3: $\not\!\!E_T$ Selection

- At least two jets with p_T >15 GeV each. The jets are corrected at Level 7, in order to achieve reconstruction at parton level. In order to achieve good data to Monte Carlo agreement (as will be described in the following chapter) an additional cut has been set at $\Delta\eta(J1, J2)$ <2.5. The signal signature doesn't have significant contribution above this point. The jet selection cuts that are used in the analysis are summarized in Table 4.4.

- One additional cut applied to ensure good data to Monte Carlo agreement is on the leptonic W transverse mass: 30 GeV < M_T < 120 GeV. The good agreement in this region will be demonstrated in the following chapter.

4.5 Summary

A series of sophisticated triggers and algorithms are used for the data to be collected and translated into physical quantities. The main objects that form the signatures

Jet	Algorithm	JetClu
	Cone	0.4
	Correction	Level 7
	P_T	> 15 GeV
	$\|\eta\|$	< 2.4
	Electron Removal	$\Delta R < 0.52$
	NJets	≥ 2
	$\Delta\eta(J1, J2)$	< 2.5

Table 4.4: Jet Selection

of interest are the charges leptons (electrons and muons), the neutrinos and the jets. In this chapter, the electron and muon reconstruction, the jet algorithms and the missing transverse energy measurement are presented. The event selection includes exactly one charged lepton, missing transverse energy > 25 GeV and at least two jets of $p_T > 15$ GeV each. In the following chapter, this selection will be applied in data and Monte Carlo simulated events, and the agreement between the two will be verified.

Chapter 5

Monte Carlo

In order to understand the data that physicists deal with, it is essential to understand the various components that generate interesting effects. In a process of interest, like for instance the semi-leptonic decays of the WW and WZ production, it is essential to know not only the characteristics of the signal signature but also the contributions of the background processes. It is therefore essential to have very precise representation of the event properties of a wide range of reactions. This is the role of the Monte Carlo (MC) in high energy physics; it provides an accurate description of the physics processes. The events that are generated using MC algorithms give a representation of a physics process at the interaction point. These events are treated for detector effects in order to be comparable to the data.

5.1 Monte Carlo at High Energy Physics

5.1.1 The Complexity

Multi-particle production is the most characteristic feature of modern high energy physics. To first approximation all processes have a simple structure at the level of interactions between the fundamental objects of nature (e.g. $u\bar{d} \to W^{+*} \to W^{+}[\to e^{+}\nu_{e^{+}}]Z^{0}[\to d\bar{d}]$). However corrections make this simple picture of two quarks producing at the final state two quarks and two lepton, become much more complex; indeed, instead of a 4-particle final state, hundreds of final particles are produced [36].

Corrections are initiated by bremsstrahlung-type modifications (e.g. emission of additional final state particles, like photons or gluons). The photon emission process has a sizable effect in electron final states. In case of gluon emission, because of the large strong coupling, a large flux of particles can be the result in the final state.

This is called the *parton shower*; the large number of partons in the final state result from a single initial parton. Such effects can be calculated theoretically, however the answer is complicated and lengthy. Perturbative calculations that take into account higher to leading order corrections are often very difficult to be computed, but for precision studies it is necessary that such effects are considered.

Another very important correction comes from the confined nature of quarks and gluons. The structure of the incoming hadrons as well as the complicated hadronization process of the quarks and gluons, are not well described in the perturbative language. The chain of processes subsequent to hadronization (e.g. the fragmentation) are very complicated and their description is only based on models. For precision studies, the detailed modeling of the hadronization process is required.

Monte Carlo generators simplify the complexity problem, by factorizing it into a number of components, each of which can be handled accurately. They form events with the same average behavior and the same fluctuations as in data. This is done by selecting all relevant variables according to the desired probability distributions, ensuring randomness of the final events. All physics effects are cast into a probabilistic language. This principle is very simple, and very successful once the probability distributions used for the description of a process are accurate enough. The most challenging step in the Monte Carlo generation is the modeling of the perturbative corrections and effects like the fragmentation.

5.1.2 The Techniques

Two approaches exist traditionally. One is the *Matrix Element* method, in which Feynman diagrams are calculated order by order. This is in principle the correct approach, however calculations become very complicated, or even impossible, in higher orders. The perturbative expansion is well described at high energy scales, because of the running of the strong coupling a_s, therefore inclusive measurements of well-separated jets are reliable. However, when soft gluon emission becomes significant in the event, the matrix element approach becomes less relevant. This is where the *Parton Shower* method gives a solution. In this approach, an arbitrary number of branchings of one parton into two (or more) may be combined to yield a description of multi-jet events, with no explicit upper limit of the number of partons involved. This gives a good description of the substructure of jets, but the showers don't give good predictions for multi-jet events.

5.1.3 Monte Carlo Generators

Within the CDF collaboration, PYTHIA ([36], [37]) is the Monte Carlo generator most widely used for the simulation of the electroweak processes. PYTHIA generates events at Leading Order (LO) approximation and uses the *Parton Shower* approach to the perturbative corrections modeling, except explicit matrix-element-inspired corrections to the parton shower in specific processes (e.g. inclusive single boson production). This approach offers a good description of the electroweak processes. However, if one is interested in large multiplicity of QCD jets, the description that PYTHIA provides isn't accurate. For such processes there is the need of a *Matrix Element* approach.

ALPGEN ([38]) is *'A collection of codes for the generation of multi-parton processes in hadronic collisions'*; it is a Monte Carlo generator that provides *Matrix Element* evaluation at Leading Order approximation and interfaced with PYTHIA for the *Parton Shower* implementation.

$W + jets$ using ALPGEN+Pythia

The case of the $W + jets$ is only a specific one, but it is a good example of an ALPGEN+PYTHIA sample; it is in any case a significant background for the signature of interest in this thesis, but also other various interesting signatures, including Higgs signatures. The good modeling of this process is therefore essential. The different subprocesses included in the $W + jets$ calculation are listed in Figure 5.1.

jproc	subprocess	jproc	subprocess	jproc	subprocess
1	$q\bar{q}' \to W$	2	$qg \to q'W$	3	$gq \to q'W$
4	$gg \to q\bar{q}'W$	5	$q\bar{q}' \to Wq''\bar{q}''$	6	$qq'' \to Wq'q''$
7	$q''q \to Wq'q''$	8	$q\bar{q} \to Wq'\bar{q}''$	9	$q\bar{q}' \to Wq\bar{q}$
10	$\bar{q}'q \to Wq\bar{q}$	11	$q\bar{q} \to Wq\bar{q}'$	12	$q\bar{q} \to Wq'\bar{q}$
13	$qq \to Wqq'$	14	$qq' \to Wqq$	15	$qq' \to Wq'q'$
16	$qg \to Wq'q''\bar{q}''$	17	$gq \to Wq'q''\bar{q}''$	18	$qg \to Wqq\bar{q}'$
19	$qg \to Wq'q\bar{q}$	20	$gq \to Wqq\bar{q}'$	21	$gq \to Wq'q\bar{q}$
22	$qg \to Wq'q'\bar{q}'$	23	$gq \to Wq'q'\bar{q}'$	24	$gg \to Wq\bar{q}'q''\bar{q}''$
25	$gg \to Wq\bar{q}q\bar{q}'$				

Figure 5.1: Subprocesses included in the $W(\to e\nu_e) + jets$ code. Additional final-state gluons are not explicitely shown here but are included in the calculations.[39]

The $W+jets$ sample is composed of sub-samples divided according to the parton multiplicity ($W+0p$, $W+1p$, ..., $W+np$). For a given multiplicity κ, parton-level configurations are generated with partons constrained by a minimum p_T. PYTHIA is then used for the jet showering and using a jet algorithm, jets are formed at generator level (there are no detector effects applied yet). The generated κ partons are matched with jets in ΔR[1]. A jet can only be matched to one parton. If all κ partons are matched with jets, then the event is kept, else it is discarded. By following this algorithm, the samples that are generated for each multiplicity will be inclusive samples for this specific multiplicity. Exclusive samples are formed by requiring that the number of reconstructed jets (at generator level) be equal to the number of partons κ. By merging exclusive jet samples we obtain an inclusive sample that contains all jet multiplicity.[2]

At CDF the $W+jets$ sample consists of 5 sub-samples. All are exclusive in multiplicity, except the last one that is inclusive ($W+4p$).

5.2 Signal and Background Modeling

The modeling of the signal and background processes of interest is performed using MC. The various samples used in the analysis are listed in Table 5.1. The luminosities mentioned in this table for the MC samples are calculated using the luminosity definition:

$$Lumi_{MC} = \frac{N_{Gen}}{\sigma_{theor}}$$

where N_{Gen} is the number of generated events and σ_{theor} is the theoretical cross section for the PYTHIA samples and the relative generation cross section for the $W+np$ samples. The Monte Carlo luminosity is an *effective* luminosity used for the scaling of the MC samples to the data.

By using the theoretical cross section in the effective luminosity calculation, we overlook the fact that the MC samples, being PYTHIA samples, only give an LO approximation to the data. For the $W+np$ samples specifically, the relative cross sections are used for the normalization of the samples and the overall normalization is given by re-scaling the $W+jets$ sample to achieve data-MC agreement. The re-scaling is made simultaneously for the electron and the muon selection, and only in a control region (defined in 5.3.3).

[1] $\Delta R = \sqrt{(\Delta\eta^2 + \Delta\phi^2)}$

[2] The procedure described is called *'MLM prescription'*.

A set of multiplication factors (efficiencies and scale factors) has been used for scaling the electroweak MC samples to the data. These efficiencies and scale factors are the ones mentioned the description of the event reconstruction (Chapter [2]) and are summarized in Table 5.2.

The only process that is not modeled using MC is the QCD background. The method used for its estimation is the "$\not\!\!E_T$ vs Iso", a data based method widely used by many CDF Run II analyses ([28],[34]), and which is described below.

$\not\!\!E_T$ vs Iso

One of the most challenging backgrounds to estimate is the background due to the QCD processes, where a lepton is faked by jets. This effect is most significant in the case of electrons, which can be easily faked by jets of low track multiplicity and significant electromagnetic energy. This background is estimated by extrapolating the number of background events from a region away from the W signal into the W signal region. This assumes that for the background there is no correlation between the lepton isolation and the $\not\!\!E_T$.

Figure 5.2 shows the isolation fraction vs the $\not\!\!E_T$ for the data. We define below four regions. One is the signal region, with lepton isolation fraction < 0.1 and $\not\!\!E_T > 25$ GeV. The other three regions are defined to some extent *arbitrarily*; they are regions with negligible signal contamination, and the QCD background estimated using such definitions gives good overall agreement between data and MC.

- Region A: isolation fraction > 0.3 and $\not\!\!E_T < 10$ GeV
- Region B: isolation fraction < 0.1 and $\not\!\!E_T < 10$ GeV
- Region C: isolation fraction > 0.3 and $\not\!\!E_T > 25$ GeV
- Region D: isolation fraction < 0.1 and $\not\!\!E_T > 25$ GeV (Signal region)

We therefore make the assumption that the QCD background in the signal region is given by the ratio

$$N_{QCD\ Region\ D} = \frac{N_{Region\ B} \times N_{Region\ C}}{N_{Region\ A}}$$

The regions A, B and C have small contributions from the signal itself as well as other electroweak backgrounds such as $W \to \tau\nu$ and $Z \to e^+e^-$, for the case of $W \to e\nu$. Therefore, in order to correctly extrapolate from the regions A, B and C

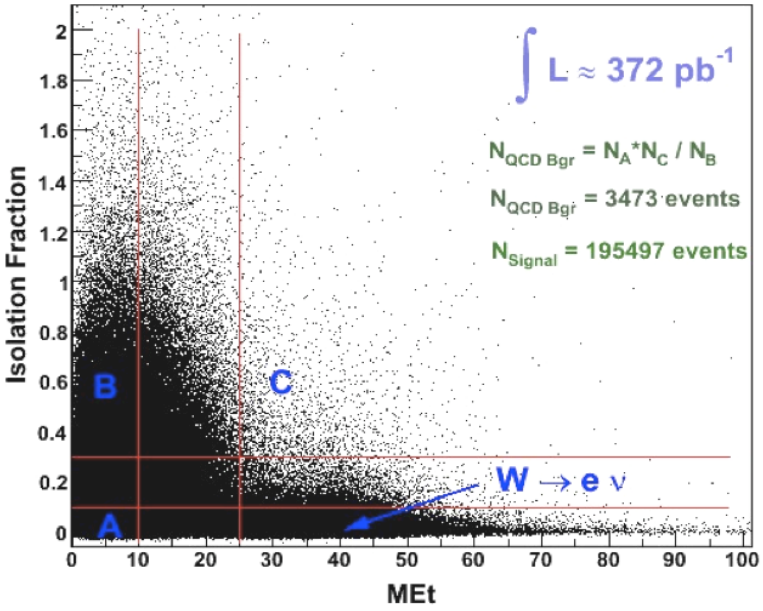

Figure 5.2: The $\not\!\!E_T$ vs Iso diagram, for the $W \to e\nu$ process only and the first period of data (corresponding to 372 pb^{-1}). The definition of the various regions is shown.

to the QCD background in the region D, these contributions have to be taken into account.

Therefore, the formula we use to extract the QCD background from the data is

$$N_{QCD\ Region\ D} = \frac{(N_{Region\ B} - N_B^{EWK} - N_B^{Signal}) \times (N_{Region\ C} - N_C^{EWK} - N_C^{Signal})}{N_{Region\ A} - N_A^{EWK} - N_A^{Signal}}$$

Process	$\sigma \times Br$(pb)	Sample	Lumi (pb^{-1})	Comments
WW	12.4*0.146	wtop2w	167550	PYTHIA
WZ	3.96*0.07	wtop2z	531471	
W($e\nu$)+0p	1810	pt0sw0	2474.9	W+np
W($e\nu$)+1p	225	pt0s1w	19716.6	
W($e\nu$)+2p	35.5	pt0s2w	23379.7	ALPGEN+PYTHIA
W($e\nu$)+3p	5.63	pt0s3w	127383.	
W($e\nu$)+4p	1.59	pt0s4w	388214.	MLM Matching
W($\mu\nu$)+0p	1810	pt0sw5	2500.6	
W($\mu\nu$)+1p	225	pt0s6w	20093.8	
W($\mu\nu$)+2p	35.5	pt0s7w	22536.7	
W($\mu\nu$)+3p	5.63	pt0s8w	132490.	
W($\mu\nu$)+4p	1.59	pt0s9w	794695.	
W$\rightarrow \tau\nu$	2780	we0s9t	3191.8	PYTHIA
		we0sat	2252.8	
Z$\rightarrow$ee	497.42	ze0sbd	6362.	
		ze0sad	12600.3	
Z$\rightarrow \mu\mu$	497.42	ze0sam	6357.4	
		ze0s9m	12586.6	
$t\bar{t}$	6.7	tewk0z	468286	
		tewk1z	538866	
QCD	from data			$\not\!\!E_T$ vs Iso
DATA		bhelbd	361.8	Total Lumi 1.2 fb^{-1}
		bhelbh	398.7	
		bhelbi	446.1	

Table 5.1: Summary of samples (Monte Carlo and data). The sample names are the CDF descriptions.

	Period	CEM	CMUP	CMX
DATA-MC ID sc.f.	0d	0.991 $\pm$ 0.004	0.922 $\pm$ 0.006	0.997 $\pm$ 0.006
[30]	0h&0i	0.979 $\pm$ 0.010	0.918 $\pm$ 0.008	0.979 $\pm$ 0.009
Eff. Trigger	0d	0.962 $\pm$ 0.006	0.902 $\pm$ 0.004	0.967 $\pm$ 0.004
[31]	0h&0i	0.977 $\pm$ 0.006	0.919 $\pm$ 0.004	0.955 $\pm$ 0.004
Data-MC Trck sc.f.	0d	1.009 $\pm$ 0.002		
[32], [33]	0h&0i	1.014 $\pm$ 0.003		
Eff. Vtx.	0d	0.985 $\pm$ 0.002		
[31]	0h&0i	0.961 $\pm$ 0.002		

Table 5.2: Data-MC scale factors and efficiencies

5.3 Event Selection Validation

5.3.1 $W \to \ell\nu_\ell$, $Z \to \ell^+\ell^-$

The event selection that has been described previously is validated with comparisons of the data with the MC predictions. Before applying all the selection requirements, simple and clean processes are typically tested. Such processes are the $Z \to \ell^+\ell^-$, with which the lepton selection is verified, and the $W \to \ell\nu_\ell$, that includes both lepton and $\not\!\!E_T$. This latter process is most relevant to our signature of interest. At the early stage of the analysis, $W \to \ell\nu_\ell$ cross section measurements have been performed with the different lepton types, and the good agreement in various kinematic shapes is verified. The uniformity of the shapes and event yields over the run periods is also verified.

Table 5.3 shows some indicative values for the cross section measured[3] for different run periods, for the different lepton types. In these measurements statistical uncertainties are not considered, the errors are statistical only.

Lepton Type	Period of Data	Cross section (nb)
CEM	$0d$	2.76 ± 0.01
CMUP	$0h\&0i$	2.74 ± 0.01
CMX	$0h\&0i$	2.87 ± 0.01

Table 5.3: $W \to \ell\nu_\ell$ cross section measurements for the event selection validation. The CDF measurement ([28]) for the $W \to e\nu_e$ cross section is $\sigma \times BR = 2.781 \pm 0.015(stat) \pm^{0.057}_{0.062} (sys) \pm 0.167(lum)$ nb, there is therefore agreement between the measured values.

Typical kinematical distributions for the data to MC agreement are shown in Figure 5.3. Figure 5.4 shows the $Z \to e^+e^-$ mass distributions for different run periods. The mass is fit with a gaussian in each case. The energy scale is stable over the run periods.

5.3.2 $WW\&WZ \to \ell\nu_\ell + jets$ Signal shape

In the $W \to \ell\nu_\ell$ selection, the jet requirements are added (Table 4.4) in order to obtain the full selection of the signature of interest.

[3] The method used for the cross section measurement is based on the luminosity definition. It is the same methodology used for the CDF $W \to \ell\nu_\ell$ cross section measurements ([28]). A description of the method will be omitted here, since this measurement does not contribute in the final result and is only used for early validation.

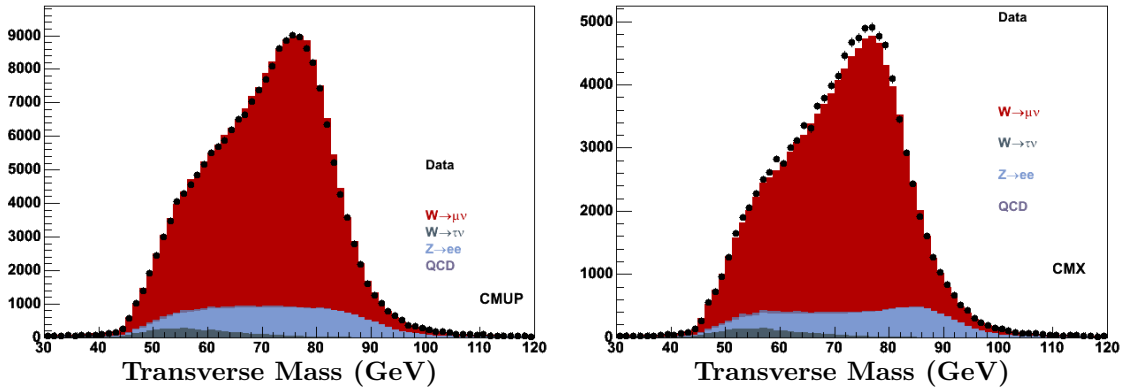

Figure 5.3: The transverse mass for the CMUP and CMX selection in the $W \rightarrow \mu\nu_\mu$ process. There is good agreement between the data and the MC expectations.

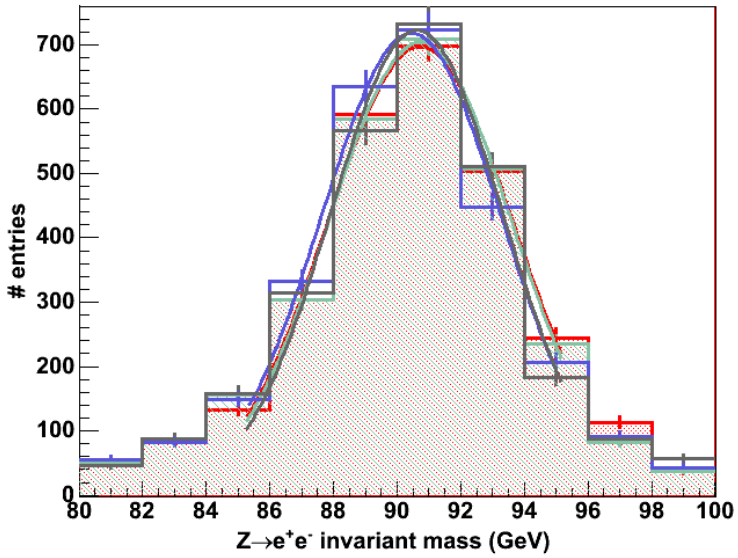

Figure 5.4: The $Z \rightarrow e^+e^-$ invariant mass, using the data. The background contamination is very small. The data are divided in 4 arbitrary sub-periods and the mass is compared. The agreement is good in both central value and width.

One would expect that the signal dijet invariant mass shape would be a gaussian with mean in the W/Z mass and width defined by the jet resolution. What the MC events that pass the event selection give is shown in Figure 5.5. In the event selection we ask for two or more jets, and from those we take into account the two leading jets in order to reconstruct the dijet invariant mass. However, the two leading jets do not always result from a W. Matching the quarks originated from a W (generator level MC) to the two leading jets in ΔR, we estimate that there is a mismatching of

$\approx 25\%$ overall (Figure 5.6). Based on the latter plot, we define the invariant mass signal region to the the region within $\approx 2\sigma$ away form the peak. We therefore define the signal region as: invariant mass $\in [60, 100] GeV$. It contains $\approx 80\%$ of the real hadronic W's. In this region, the mismatched jets are $\approx 15\%$.

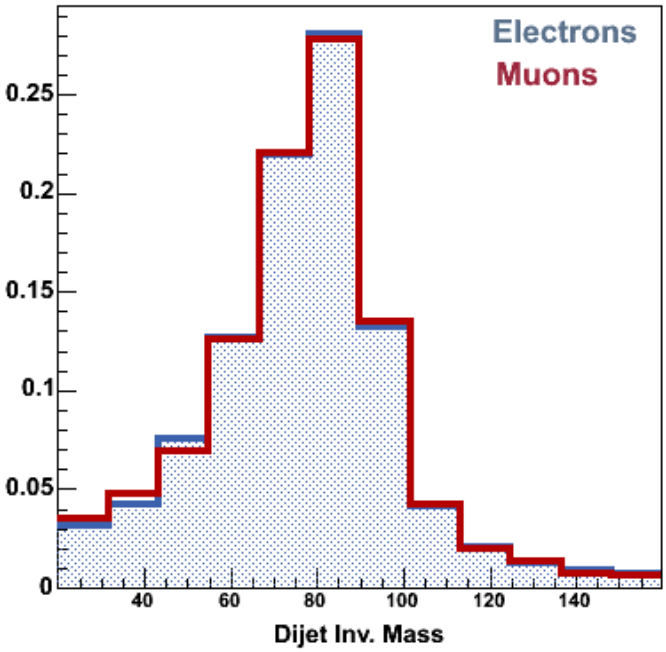

Figure 5.5: Di-jet invariant mass - Signal shapes (hadronic W of the WW&WZ production) for the electron and muon channel separately. Monte Carlo only.

The signal events (WW/WZ) are a small fraction of the total number of selected events. The MC expectation for the shape of the total number of events is shown in Figure 5.7.

5.3.3 Data vs MC (full selection)

The control region for testing the data to MC agreement is the invariant mass sidebands (invariant mass $\in [45, 60] \cup [100, 160] GeV$), where the signal fraction is negligible. Comparisons of several variables for electrons and muons combined together are shown in Figures 5.8-5.9. The data-MC agreement is good for nearly all the variables. In particular, for the invariant mass (the variable that will be used to derive the signal) the χ^2 probability for the data-MC agreement is $\approx 30\%$. The data-MC agreement has been verified separately for the different lepton types.

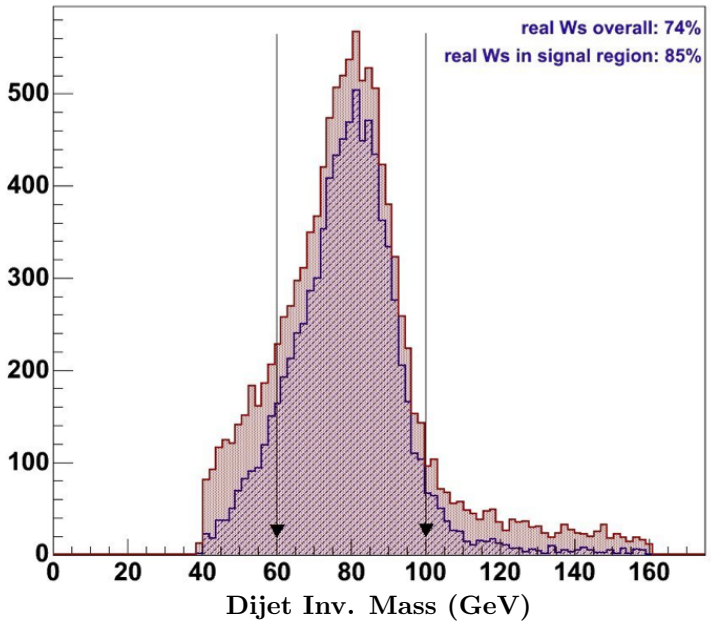

Figure 5.6: Di-jet invariant mass (hadronic W of WW production) - 2 leading jets matched to quarks (blue curve) with respect to two leading jets shapes (red curve). The study is made for the electron channel only, but can be generalized to the muon channel, given that the invariant mass shape does not differ between electrons and muons.

There are two variables where the agreement between data and MC is poor, compared to the rest: the p_T of the leading jet end the ΔR between the two leading jets. The disagreement is mainly observed in the low p_T region of the leading jet (15-30 GeV). This behavior is not unexplainable: having set the cut of the jet p_T at 15 GeV, with jets corrected at Level 7, the behavior at low p_Ts becomes very sensitive to MC generation cuts and to the details of the underlying event and the extra interactions (pile-up). This disagreement could be faced by applying a harder cut the leading jet p_T. However, a harder cut would result in sculpting of the dijet invariant mass towards the signal region and for reasons that will become obvious in the following chapter, such a sculpting is undesirable. Given that the disagreement is not significantly affecting the dijet invariant mass shape, the selection cuts do not change.

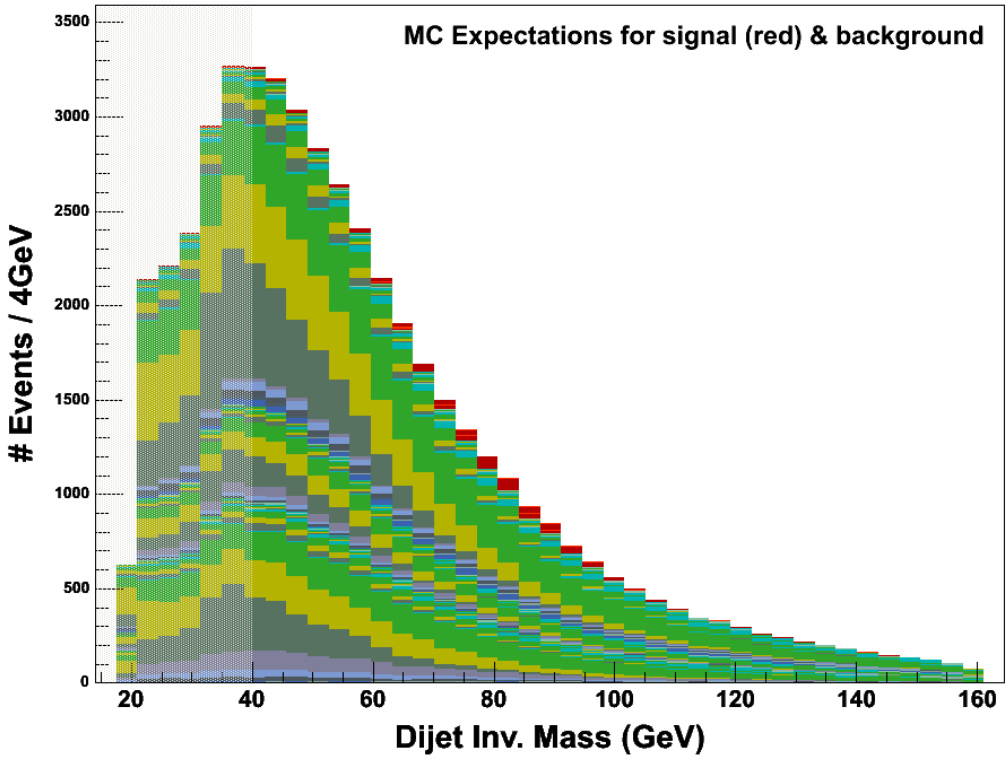

Figure 5.7: Di-jet invariant mass shape for signal and background.

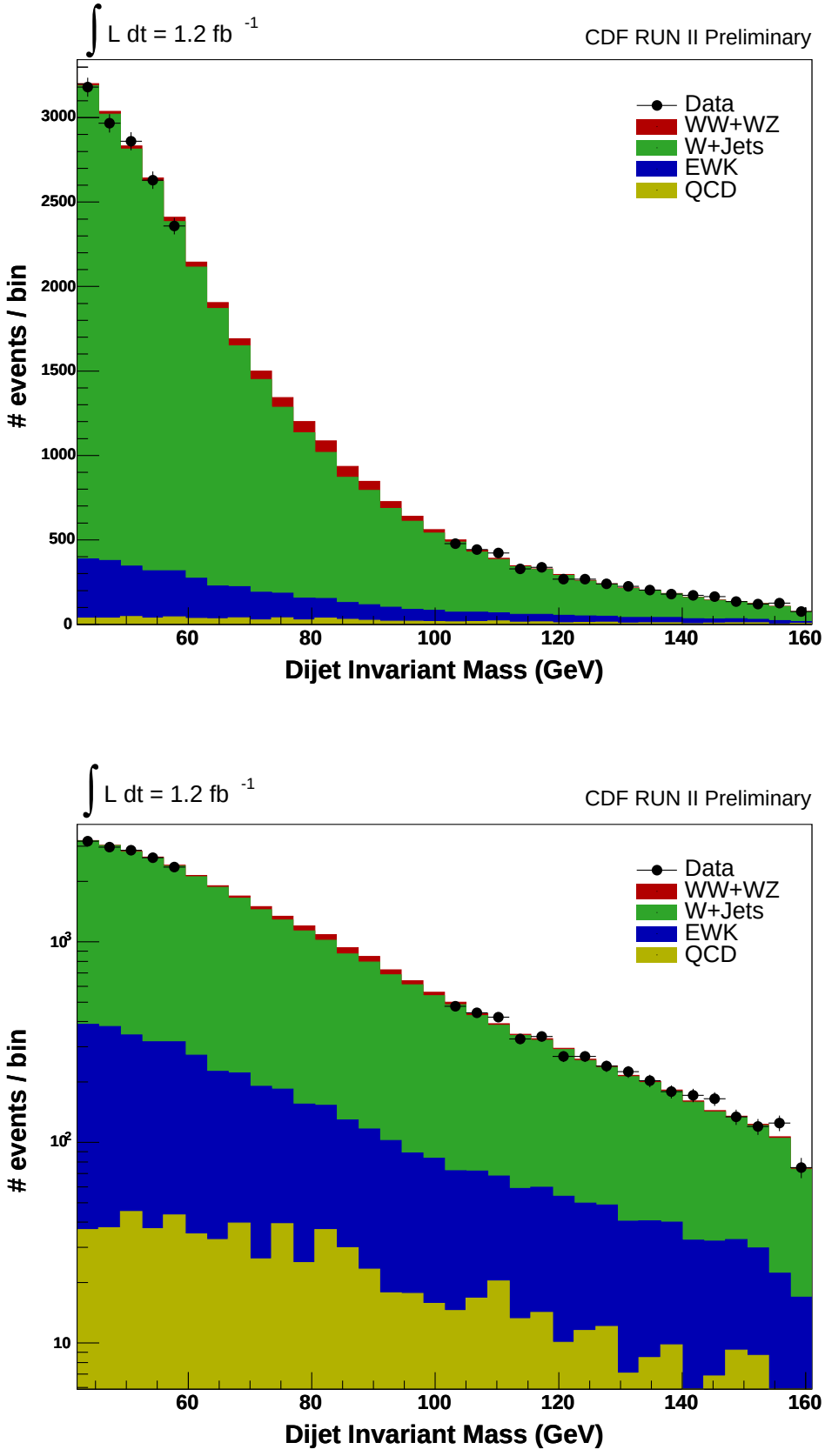

Figure 5.8: The Dijet Invariant Mass; Data-MC comparison in the sidebands.

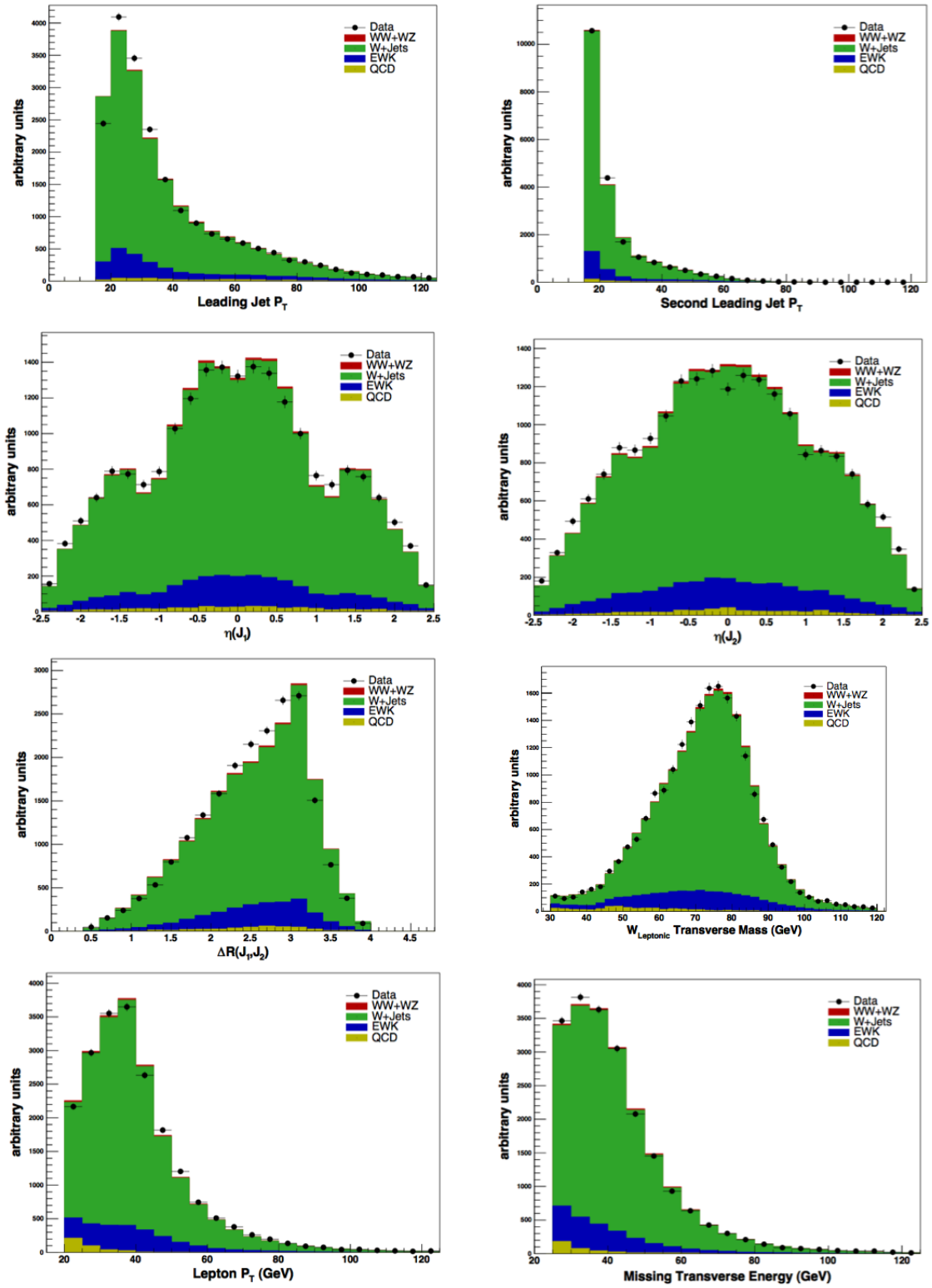

Figure 5.9: Data-MC comparisons in the dijet invariant mass sidebands.

5.4 Summary

The signatures of interest (both signal and background) are initially studied using Monte Carlo events, simulated events that by construction have the same average behavior and the same fluctuations as the data. In this chapter, the techniques for the Monte Carlo generation are described and the samples used for this analysis are presented. Using the Monte Carlo, the event selection is validated by comparing the expectations to the data. The methodology followed further in the analysis is presented in the following chapter.

Chapter 6

Analysis Description

The signal and the background signatures of the semi-leptonic decays of the WW and WZ production have been modeled using Monte Carlo, as presented in the previous chapter. The Monte Carlo provides a good modeling of the data therefore both shapes and yields can be trusted, as it has been shown. So far the data themselves have not been studied except in the signal region sidebands. In fact, the data will only be studied in the last part of the analysis. The analysis methodology will be set using the Monte Carlo description of the signal region.

Using the Monte Carlo description in the signal region we find that the signal (S) over background (B) ratio (S/B) is very poor. Also very poor are the signal fraction ($S/(S+B)$) and the $significance$, defined as the ratio of the signal yield S to the total statistical error (in the gaussian approximation) ($significance = S/\sqrt{(S+B)}$) (Table 6.1). In order to increase the probability of seeing a signal these ratios need improvement, and in this perspective is based the methodology which has been chosen.

Before ANN Cut		$\frac{S}{S+B}$	$\frac{S}{\sqrt{S+B}}$
SIG	716	0.024	4.2
BGR	29093		

Table 6.1: Signal and background yields for invariant mass [45,160]GeV

6.1 Analysis Methodology Overview

The methodology that has been used for the analysis is motivated by the fact that the initial significance and S/B are very poor and the signal is therefore hidden

in a very large background. In principle, direct cuts could be applied in various kinematic variables where the signal and the background are separated. However, there is the possibility to exploit correlations between several variables by using some *multivariate technique*. Such techniques exploit information from several variables simultaneously, while direct cuts only incorporate information from one variable at a time. In this analysis, the multivariate technique we use is the *Artificial Neural Network* (explained further in section 6.2).

The Artificial Neural Network is trained using variables where the signal and background are well separated in shape. The output is a global variable where the signal and background are as widely separated as possible. This global variable is used for the maximum significance gain point definition. We perform a lower cut at this point. In the data above this point the signal and background have the 'maximum possible' significance, within the context of the chosen Neural Network.

We use the dijet invariant mass to continue the analysis. We parameterize the shape of the dijet invariant mass after the Neural Network cut is performed. The shape of the signal is given by the Pythia Monte Carlo, while the shape of the background is motivated by Monte Carlo and contains two free parameters. The overall parameterization includes the signal and background descriptions, with the signal fraction being a free parameter. A likelihood function is constructed using this parameterization, and a fit is performed on the data. The fit will give us the parameters of the background as well as the signal fraction, that is interpreted as a number of events.

This analysis procedure summarized above is schematically described in Figure 6.1 and is explained in detail in the rest of this chapter.

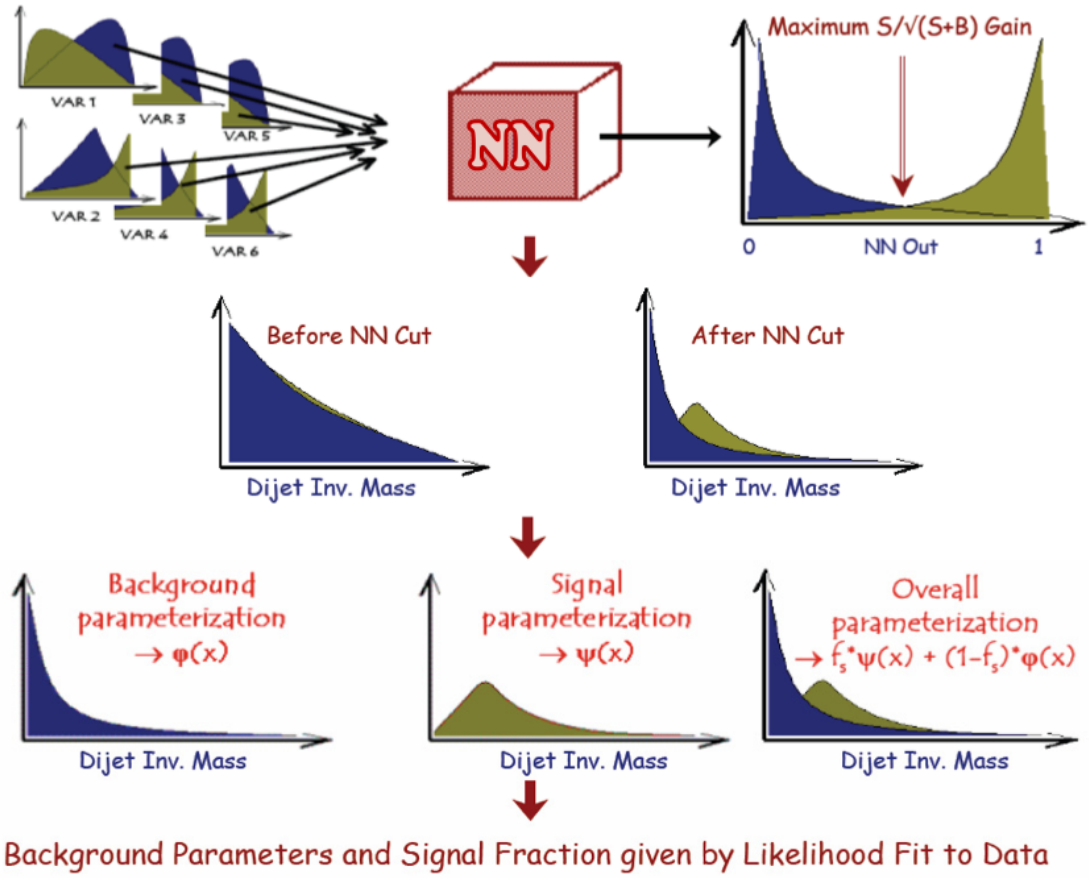

Figure 6.1: Analysis methodology schematic overview.

6.2 The Artificial Neural Network

6.2.1 General

In high energy physics, the main type of Artificial Neural Network (ANN) used is called the 'feed-forward multilayer perceptron', which is 'trained' using a 'back-propagation' algorithm. Using simple words to describe it, a feed-forward network can be thought of as a single-valued function of input values. The function has many parameters, called weights and thresholds, the values of which determine the output for a given input vector. Usually the output is a continuous distribution in the range 0 to 1. The training of the network is in fact equivalent to a minimization procedure. The aim is to reduce the 'error function' which is essentially a chi-square-like quantity, the sum of the squared deviations of the neural network output from the desired output for signal (usually 1) and background (usually 0). Then the trained network with its optimised weights and thresholds is used with real events, and the network output for each event is used to define if the event is selected or not [40].

A schematic representation of a feed-forward network is shown in Figure 6.2.

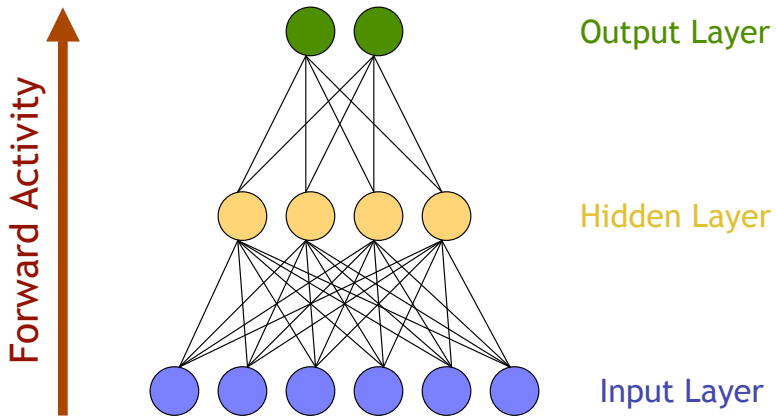

Figure 6.2: An example of a simple feed-forward network. In allows signals to travel one way, from input to output. There is no feedback; the output of any layer does not affect the same layer. Such networks are extensively used in pattern recognition.

The ANN that has been used is the Root interface to JETNET[1] [41] developed by the Ohio State University [42].

[1] JETNET is a FORTRAN collection of subroutines for training and testing ANNs.

6.2.2 Input Variables

The prime criterion to judge upon which variables to use in the ANN input is the separation between signal and background. For this analysis, the obvious variables to use would be the two leading jet p_Ts, and variables related to those, given that the signal jets are more energetic than the background ones. However, such a choice leads to a ANN output that carries this information, therefore cutting in the ANN output is equivalent to cutting in the jet p_Ts. This cut leads in the sculpting of the dijet invariant mass close to the signal region, with the consequence that the sidebands are no longer well defined. Artificial peaks close to the signal region are unwanted.

A different approach is to use dimensionless variables (angles and angle related ones) in the training of the ANN. Performing cuts in these variables does not significantly change the dijet invariant shape, since these variables are less correlated with it. Several such variables have been used in the input of the ANN, but the variables giving the best discrimination between signal and background (best significance improvement) are the six listed below:

- $\eta_{Jet1} - \eta_{Jet2}$
- $max(\eta_{Jet1}, \eta_{Jet2})$
- $\frac{\sum P_T^2}{\sum P^2}$, sum over all objects (for the neutrino, in both numerator and denominator, the $\not{E}_T$ is used)
- $\frac{\sum P_T^2}{\sum P^2}$, sum over the two leading jets
- $\Delta\theta_{1,2} = \theta_{Jet1} - \theta_{Jet2}$, in the boosted di-jet system
- $\Delta\theta_{di-jet,1}$, in the boosted di-jet system. $\Delta\theta_{di-jet,1}$ is given by

$$if\ \ \phi_{Jet1}^{Boosted} * \phi_{di-jet} > 0,\ \ \Delta\theta_{di-jet,1} = |\theta_{Jet1}^{Boosted} - \theta_{di-jet}|$$

$$else\ \ \Delta\theta_{di-jet,1} = |\pi - \theta_{Jet1}^{Boosted} - \theta_{di-jet}|$$

The training of the ANN has been performed using the variables in the signal region only, and both the background and signal descriptions are given by the MC. In Figure 6.3 the background and signal shapes of the input variables are shown. The signal description is given by the combination of the WW and WZ expectations,

as given by the Pythia inclusive MC samples. The background is described by the sum of all the different backgrounds (Table 5.1).

The ANN has been trained with the electrons and muons combined. In order to do that, we verify that the electron and muon signal and background shapes are similar. This is shown in the Figures 6.4 and 6.5, where the signal and background shapes for the various input variables are compared.

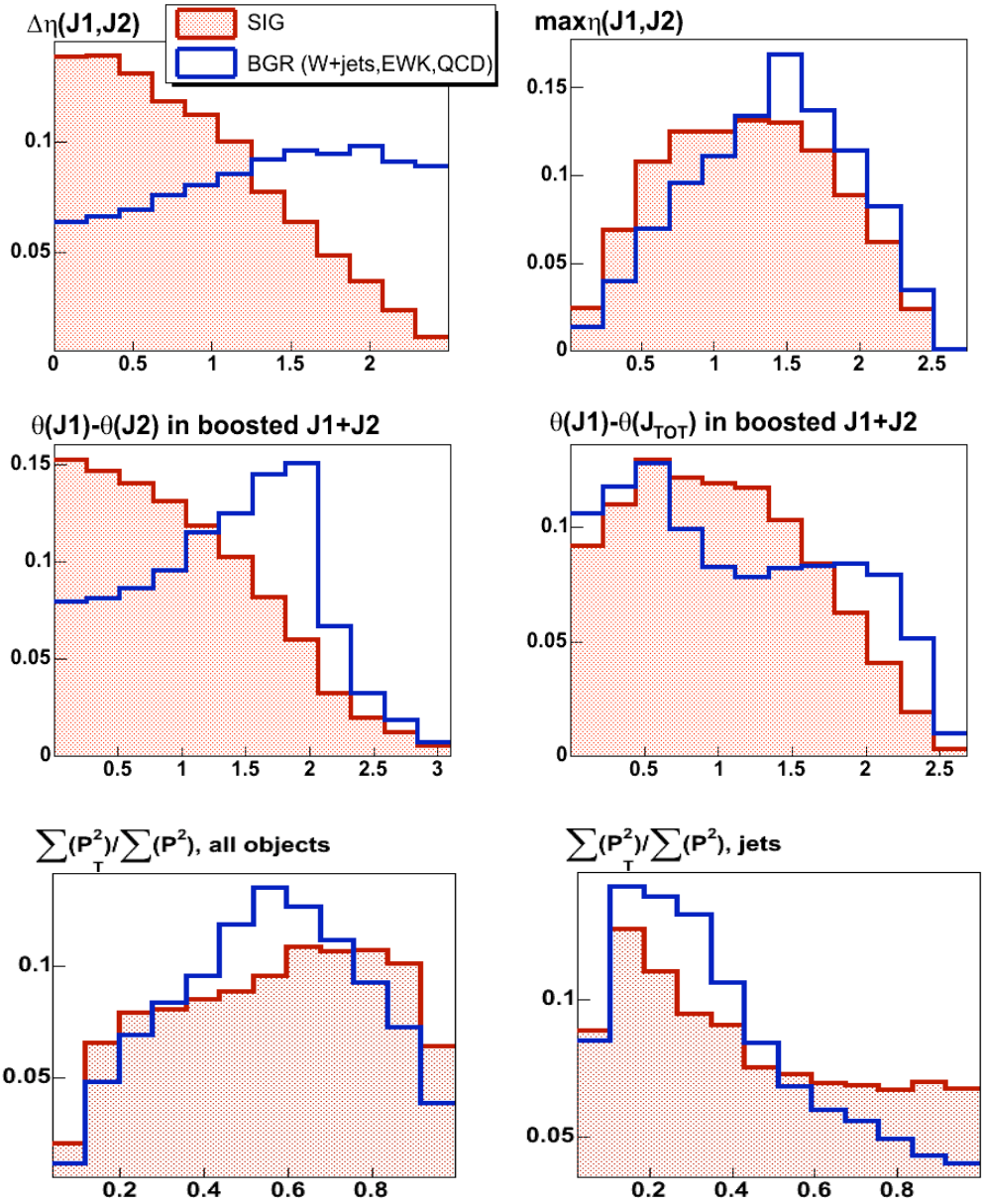

Figure 6.3: Neural Network input variables. The ANN is trained with events in the signal region only.

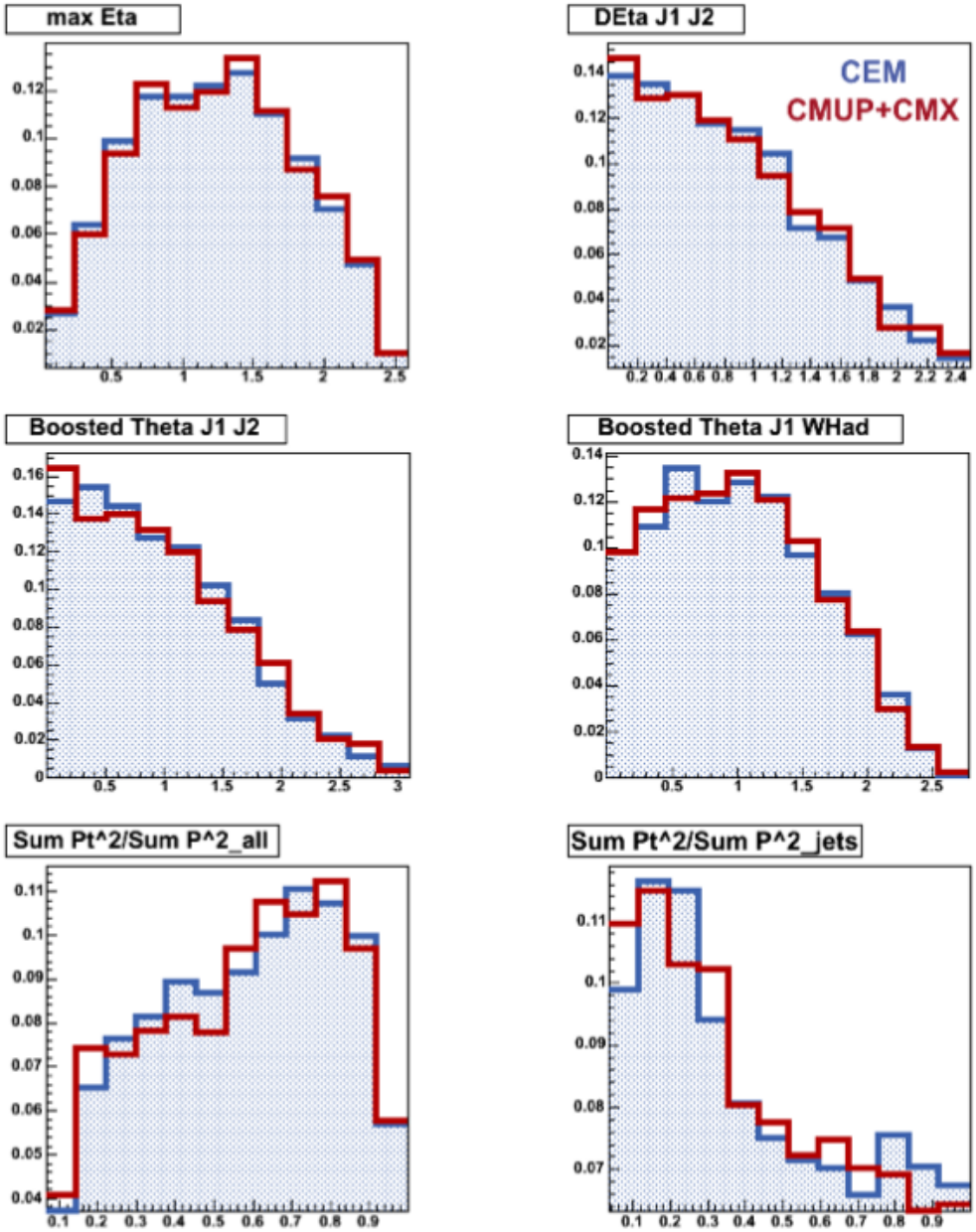

Figure 6.4: ANN input variables (SIGNAL) - Comparison between CEM electrons (blue) and CMUP&CMX muons (red).

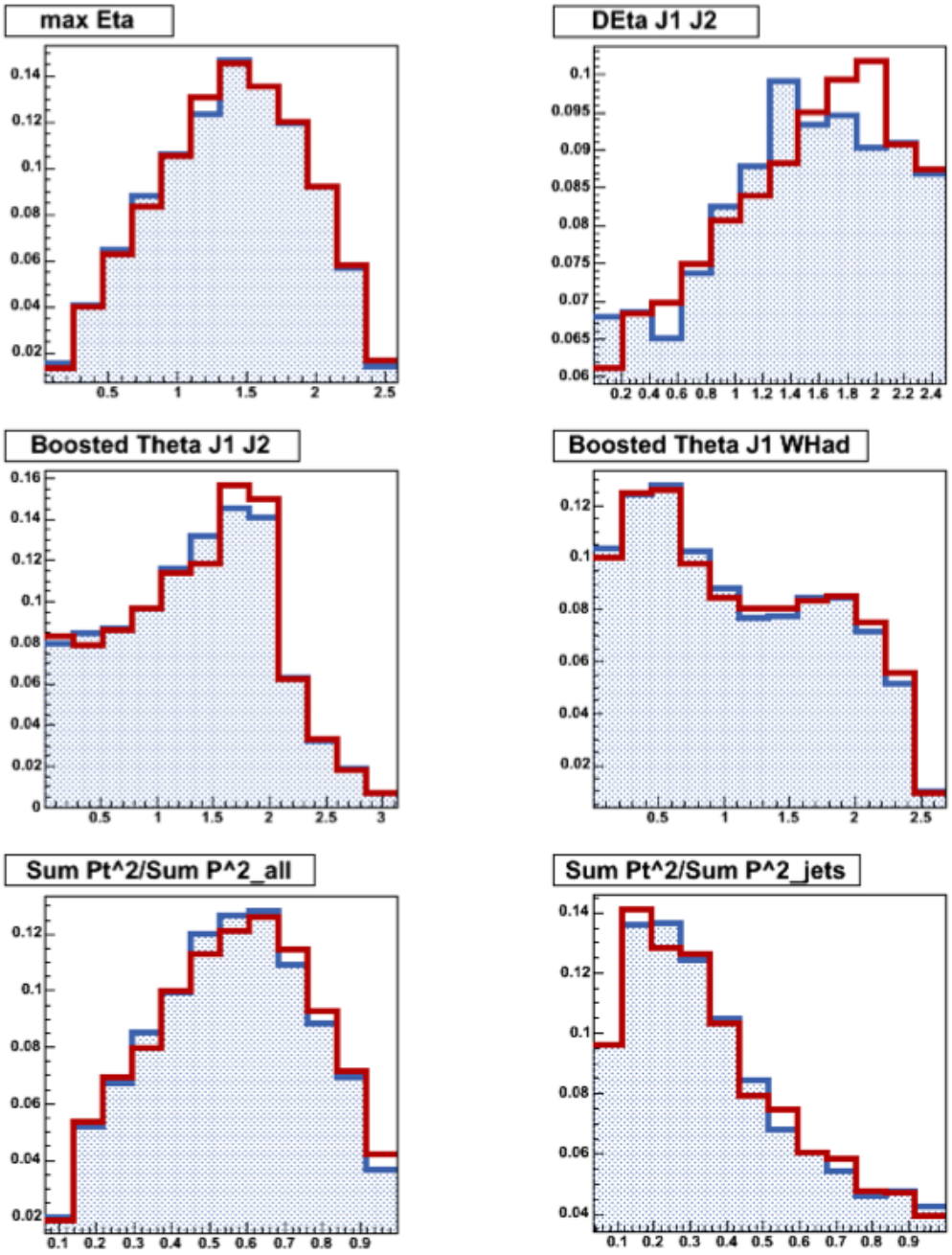

Figure 6.5: ANN input variables (Background) - Comparison between CEM electrons (blue) and CMUP&CMX muons (red).

6.2.3 ANN Output

A significance curve is plotted as a function of the ANN output. The significance is defined as

$$Significance = \frac{S}{\sqrt{S+B}}$$

Several sets of input variables have been used, with different numbers of input nodes and different minimization algorithms, and the set that leads to the best significance gain has been chosen as the one to be used. This is how the 6 variables described in 6.2.2 have been chosen. Those variables together with 7 hidden nodes and the so called "Backpropagation minimization algorithm" give the ANN output plot and the significance gain curve that is shown in Figure 6.6. Figure 6.7 shows the error plot of the ANN for the training and the testing samples, as a function of the number of epochs (an epoch is a sweep through the entire training data).

A summary of the signal and background yields after the ANN cut is given in Table 6.2. A comparison of the shapes of the signal and background before and after the ANN cut is shown in Figures 6.8 and 6.9.

After ANN Cut		$\frac{S}{S+B}$	$\frac{S}{\sqrt{S+B}}$
SIG	554	0.036	4.5
BGR	14481		

Table 6.2: Signal and background yields using Monte Carlo, for invariant mass [45,160]GeV, after the ANN cut.

The ANN outputs a file of weights that is applied to the MC (all backgrounds and the signal) and to the data sidebands. Comparisons between data and MC in the sidebands is shown in Figure 6.10 (Invariant mass comparisons) and in Figure 6.11 (ANN output comparison). We conclude that the data are well described by the MC for what concerns the ANN output in the sidebands (the χ^2 probability for the Data-MC agreement is $\approx 30\%$).

The parameterization of the signal and the background shapes after the ANN cut will be used in a likelihood fit that will be applied on data to estimate the signal fraction.

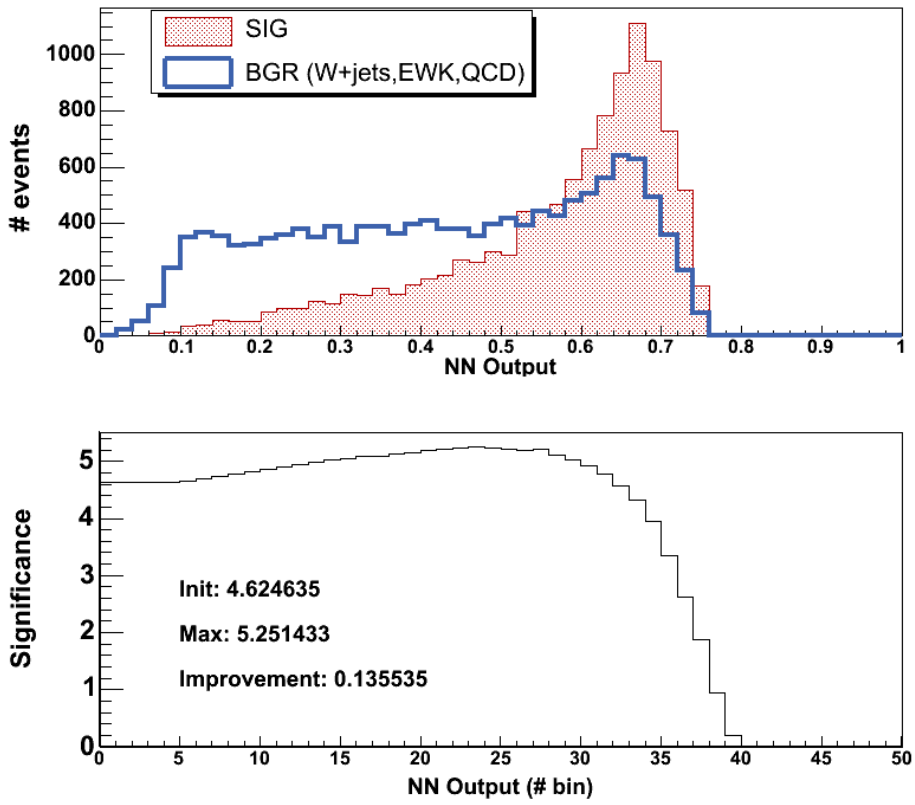

Figure 6.6: ANN output and significance improvement curve. The point of the maximum significance gain is the point where the ANN cut will be applied. The x axis of the significance plot is just an indication of the bin number and can be compared directly with the x axis of the ANN output plot. *Note: The training is performed for events in the signal region only.*

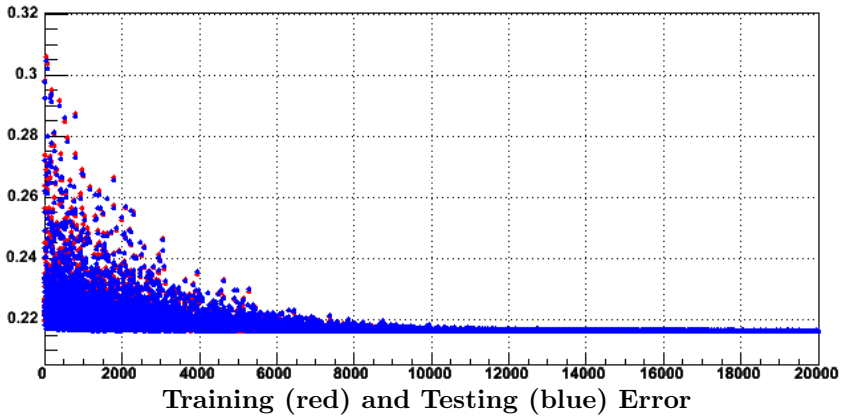

Figure 6.7: ANN error histogram, as a function of the number of epochs.

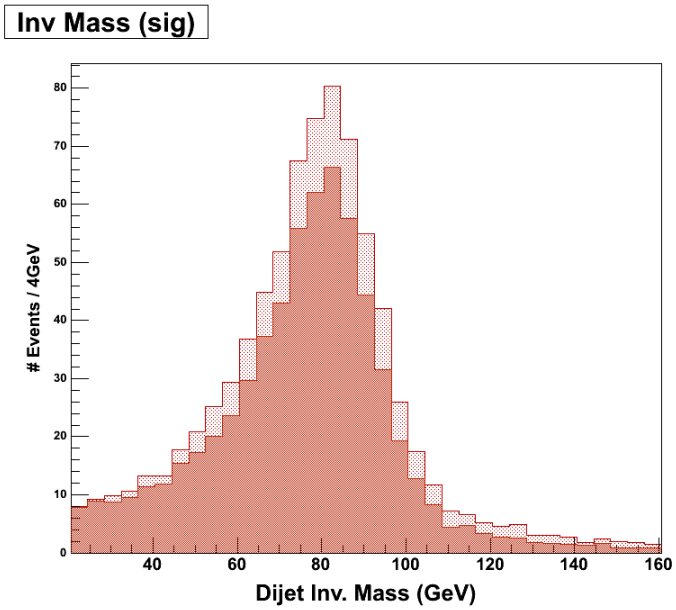

Figure 6.8: Signal shape comparison, before and after the ANN cut.

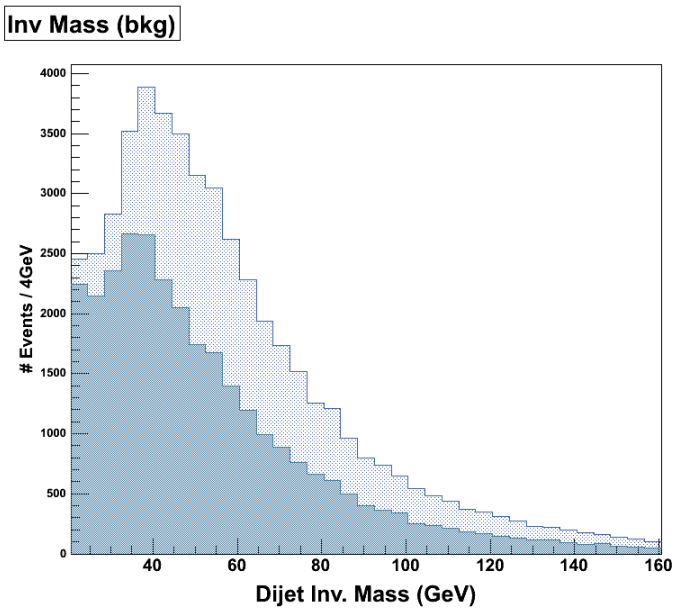

Figure 6.9: Background shape comparison, before and after the ANN cut.

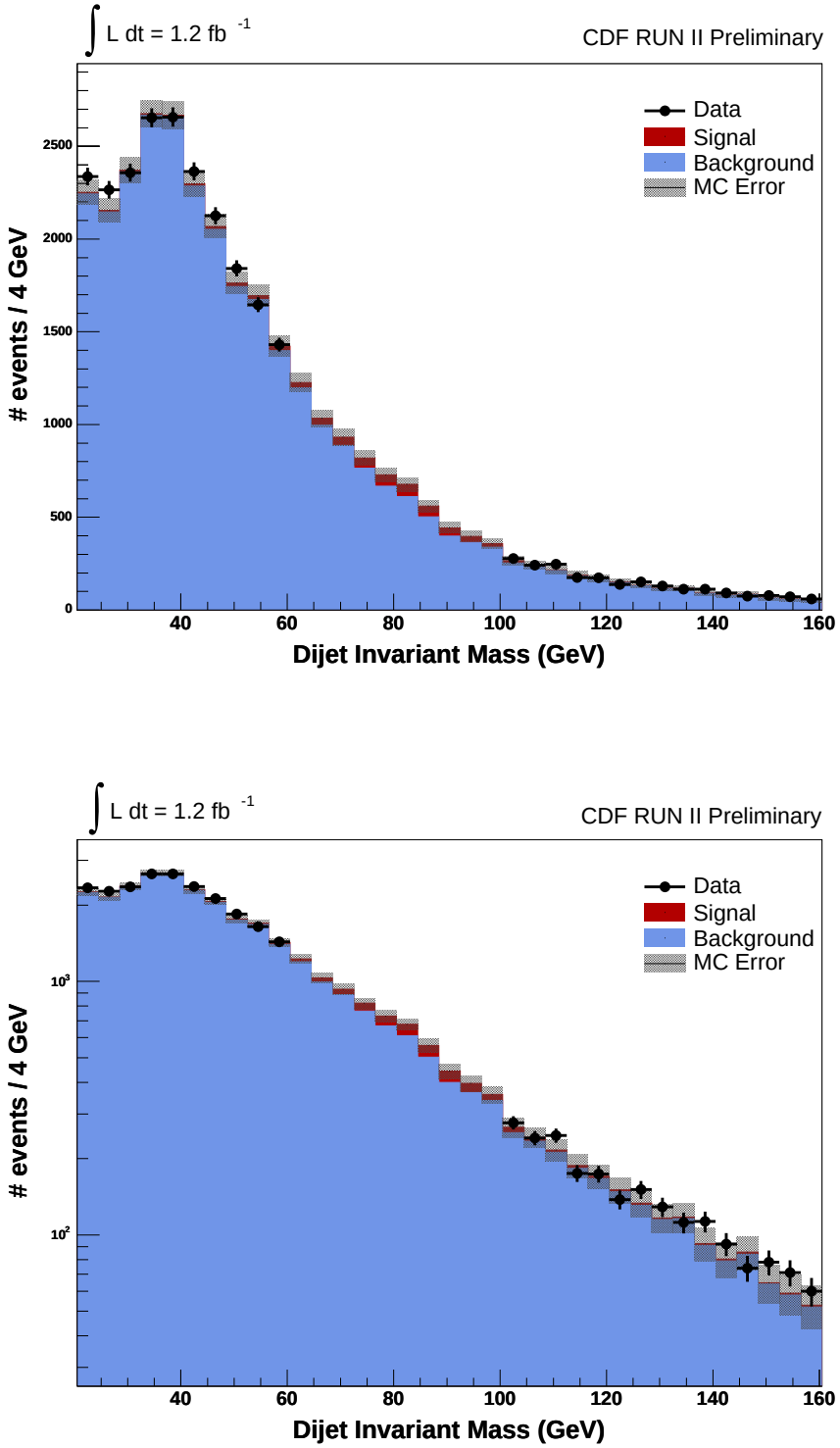

Figure 6.10: DATA-MC comparison after the ANN cut (sidebands only). The χ^2 probability for the Data-MC agreement is $\approx 60\%$.

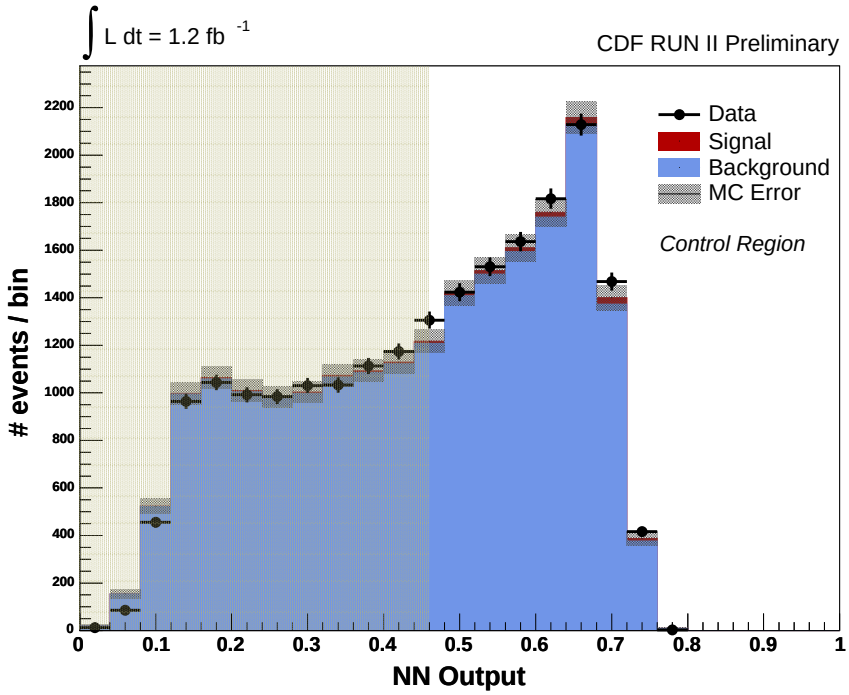

Figure 6.11: ANN Output - Data-MC comparison in the dijet invariant mass sidebands.

6.3 Likelihood Fit

6.3.1 Likelihood Definition

The parameterization of the signal and background shapes is given by the fits that are shown in Figure 6.12-6.13.

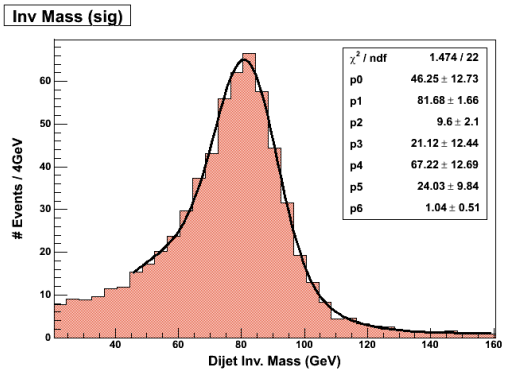

Figure 6.12: Signal shape after the ANN cut

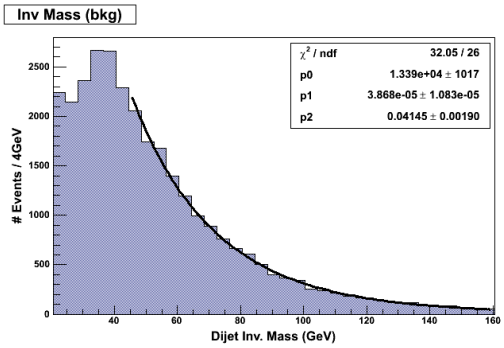

Figure 6.13: Background shape after the ANN cut

Putting those shapes in formulas, the probability distribution functions (PDF) for the signal and the background are:

$$PDF_{BGR}(x) = f^{BGR}_{normalization} \times exp(\alpha x^2 + \beta x)$$

$$PDF_{SIG}(x) = f^{SIG}_{normalization} \times (Gauss1(x) + Gauss2(x) + constant)$$

$$PDF_{TOTAL}(x) = PDF_{SIG}(x) + PDF_{BGR}(x)$$

where x is the dijet invariant mass and $f^{BGR}_{normalization} = 1 - f^{SIG}_{normalization}$ for PDF_{TOTAL} normalized to one.

The background shape is an exponential-like shape with two free parameters. The signal shape is fixed using the MC prediction. It is composed of mainly two different contributions, a gaussian that expresses the peak and resolution and one more that describes the *mismatched* jets, at low p_Ts. The total PDF contains one additional free parameter, the signal fraction.

The likelihood is defined as

$$-2 \log \mathcal{L} = -2 \sum_x \log PDF_{TOTAL}(x)$$

We define the *likelihood ratio* as

$$Q = \frac{\mathcal{L}(\mathcal{S}+\mathcal{B})}{\mathcal{L}(\mathcal{B})}$$

The likelihood ratio is a quantity that will be used in the evaluation of our result.

An unbinned likehood fit is performed for a large number of toy experiments. Each of them consists of background and signal events, of a Poisson fluctuating number according to the expectations from MC. In the fit, the parameters α and β of the background parameterization, as well as the signal fraction f_S are left floating, and the toy experiments are used to test the fitter [2].

An estimator of biases in the fitter is given by the pull of each floating variable, that is defined as

$$Pull = \frac{Expected\ Value - Fit\ Value}{Fit\ Error}$$

Test with 5K pseudoexperiments of 16K events each have been performed using the fitter, giving the pulls of Figure 6.14. Given that they are, within the statistical errors, 0 with unitary width, we are confident that the fitter is unbiased.

6.3.2 Likelihood Fit in the Sidebands

Before looking at the signal region, the data in the sidebands are used to check the background parameters α and β. The values α and β as given by the MC and data in the sidebands are given in Table 6.3. The likelihood fit to the sidebands of data is shown in Figure 6.15. Note that the fit is performed in the invariant mass range [45,160]GeV, since below 45 GeV there is a turnover, therefore going lower in the invariant mass, results in a fit with poor χ^2.

Fit Region	α (GeV^{-2})	β (GeV^{-1})
Data sidebands	$(7.14 \pm 1.56)10^{-5}$	$(4.67 \pm 0.28)10^{-2}$
Data [45,160]GeV	$(8.00 \pm 1.68)10^{-5}$	$(4.84 \pm 0.31)10^{-2}$

Table 6.3: Background parameters for the fit in the sidebands and the overall fit on the data (this last point will be explained later, and this table will be referenced).

After unblinding the data, the parameters α, β and f_S are fitted simultaneously.

[2] The fitter is written in *ROOT* using *MINUIT*. *MIGRAD* errors are taken into account (symmetric errors)

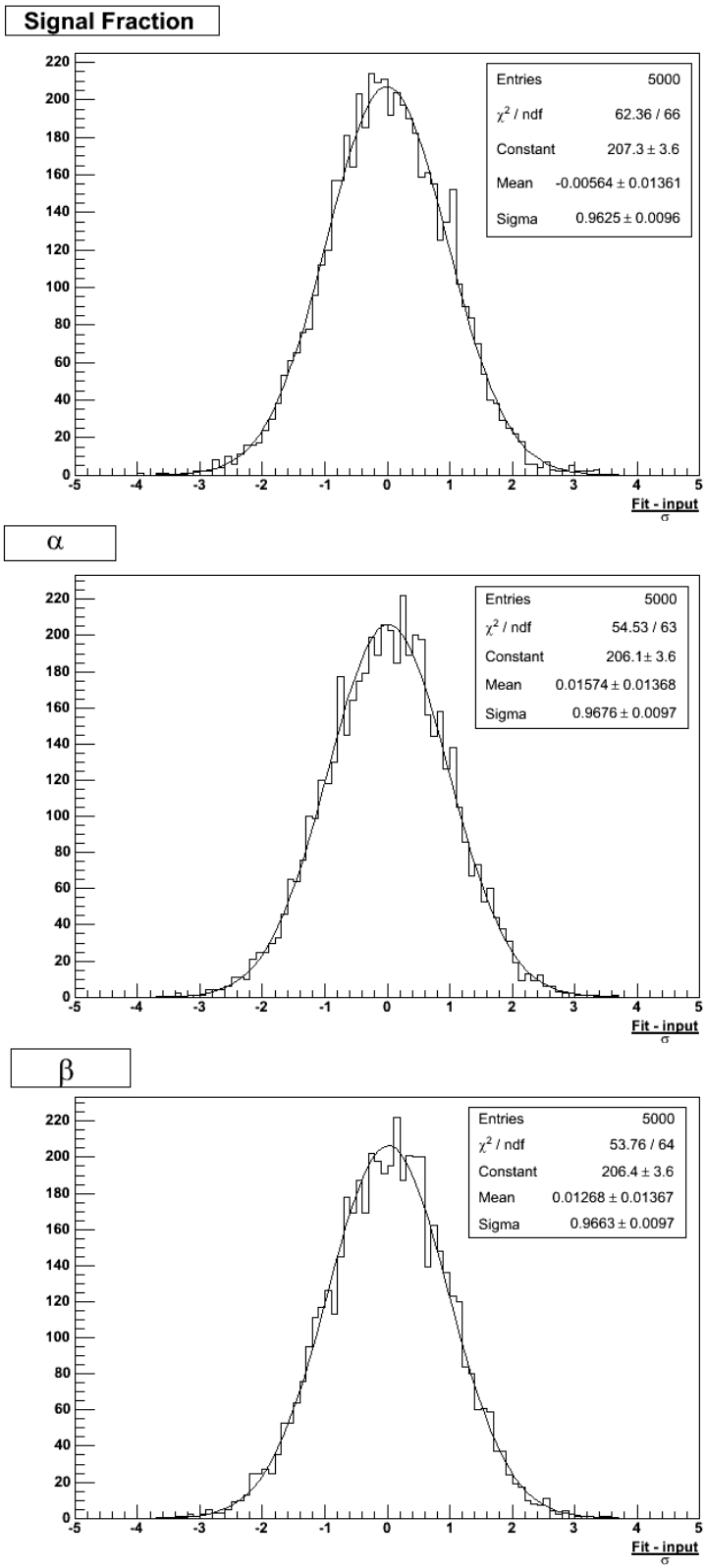

Figure 6.14: Pulls for the three free parameters of the likelihood fit (signal fraction, α, β). Toy MC has been used for testing the likelihood fitter. 16K events for each for 5K pseudoexperiments give the result that is displayed here.

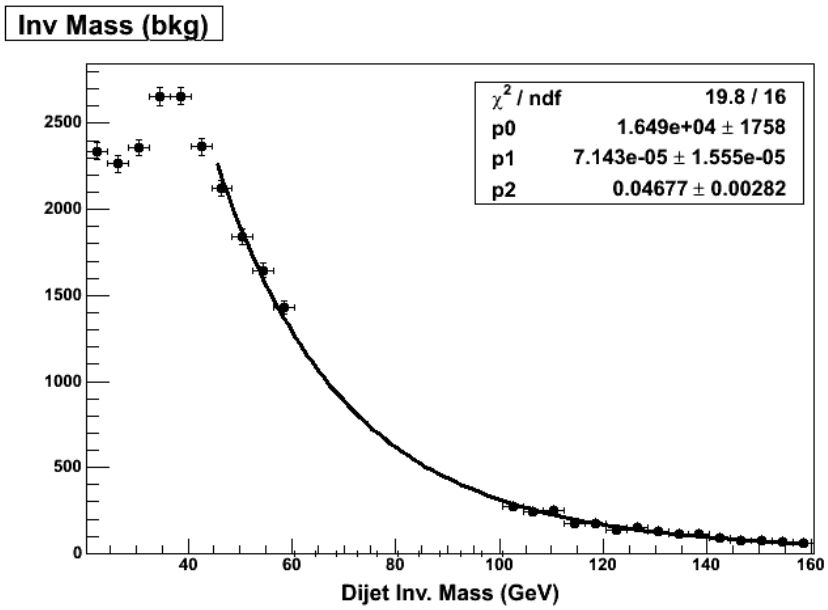

Figure 6.15: Likehood fit to sidebands of data.

6.3.3 Likelihood Ratio

A question that arises at this point is how will the signal fraction, that the likelihood fit will return, be evaluated. In other words, the question we have to answer is how much of the background could fake the signal, and vice versa.

In order to estimate this, we test the signal plus background hypothesis and the background-only hypothesis with pseudoexperiments that we generate based on the tests we have performed. We deal with these pseudoexperiments exactly as we deal with the data: we perform a fit for the three free parameters, and each time calculate the likelihood ratio. The procedure we follow is described below:

- The fit to the data in the sidebands of the invariant mass gives the parameterization of the background (the parameters α and β) that we use for generating toy pseudoexperiments. The signal description comes from MC (Pythia).

- We generate toy pseudoexperiments that describe the 'S+B' (signal plus background) hypothesis. For each of these pseudoexperiments we perform fits, exactly as we do on data. Using the values that the fit returns we calculate the likelihood ratio Q_{S+B}):

$$Q_{S+B} = \frac{\mathcal{L}(fr = fr_{fit_1}; \alpha = \alpha_{fit_1}; \beta = \beta_{fit_1})}{\mathcal{L}(fr = 0; \alpha = \alpha_{fit_2}; \beta = \beta_{fit_2})}$$

The fit values in the numerator come from a fit with all three parameters free, while in the denominator the signal fraction is fixed to zero, and the fit is done with the other two parameters being free.

- We generate toy pseudoexperiments that describe the 'B only' (background only) hypothesis. For each of these pseudoexperiments we perform two fits and compute the likelihood ratio Q_{Bonly} as described above.

We identify the median of the likelihood ratio for the S+B hypothesis. Counting the fraction of events that have smaller likelihood ratio for the B only hypothesis than this one, we identify what is the expected significance of our measurement. This fraction of events represents the fraction of background events that could fake the signal, and corresponds to a p-value that can be interpreted as a significance assuming gaussian distribution for it.

6.3.4 Expected Significance

Following the procedure described in the previous section, we use pseudo-experiments to plot the test statistic (likelihood ratio) that will answer the question *What is the signal significance we expect to measure?*. As explained previously, we test the S+B hypothesis (Figure 6.16) and the B-only hypothesis (Figure 6.17). Following the prescription described in the previous section, we estimate an expected significance of $\approx 2.5\sigma$; there is a probability (p-value) of $\approx 1\%$[3] that the background (6.17) will fluctuate high and fake the signal (median in Figure 6.16).

6.3.5 Nomenclature Comment

In previous sections and chapters, the significance was defined as $Significance = S/\sqrt{S+B}$. In this section we refer to a significance that has no longer the same definition.

The significance, as defined so far, is the definition of the significance at a counting experiment: if we imagine a dijet invariant mass with a single bin, this one bin would have a statistical error of $\sqrt{S+B}$. Therefore, the signal number of events that we would measure in this bin would have a statistical significance of $S/\sqrt{S+B}$.

[3]The significance in standard deviations can be extracted from a gaussian probability using the error function. In ROOT the significance is given using the formula: $TMath :: ErfInverse(1 - p - value) * sqrt(2)$.

Such an approach assumes that the modeling of the signal and background is exact, and the only error to be interpreted is the statistical one.

In the approach we have followed for the signal fraction extraction, we don't depend on the Monte Carlo shape or absolute number of events; the background model is motivated by Monte Carlo, but its details are fixed using the data. The significance we measure using the likelihood ratio as a test statistic includes the uncertainties in the background modeling, as given by the fitter. This is the reason why the numbers for the significance mentioned in previous sections and chapters do not agree with the expected significance we measure in this section.

6.4 Summary

The analysis methodology was presented in this chapter. It is motivated by the very poor signal over background ratio that the signature of interest has initially. An Artificial Neural Network (ANN) is used for the signal to background separation. A cut in the ANN output is applied and the the dijet invariant mass shapes of the events that pass the cut are parameterized. The parameterizations are fed into a likelihood fitter, where the signal fraction is a free parameter. Using the likelihood ratio as a test statistic, we perform pseudo-experiments and find that the expected significance for the measurement is $\approx 2.5\sigma$.

We are therefore ready to look at the signal region with data, and perform an overall fit. This is presented in the following chapter, together with the systematic uncertainties.

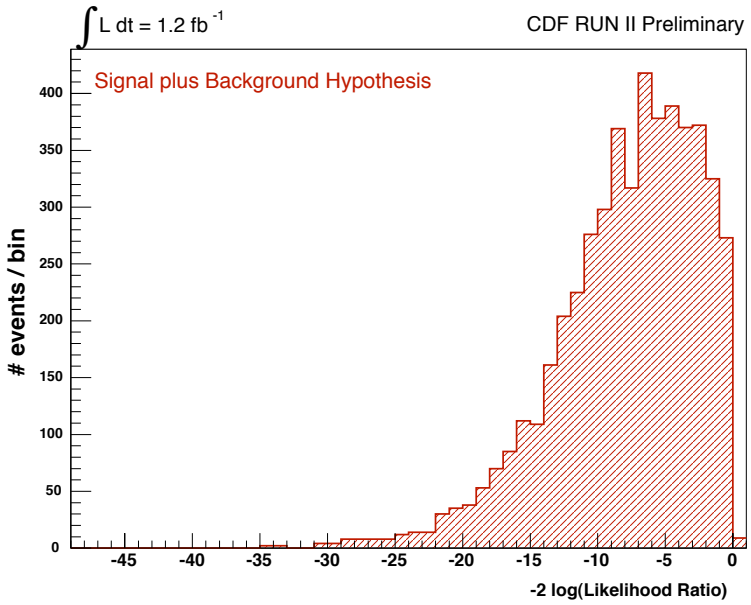

Figure 6.16: Likelihood ratio for the S+B hypothesis (5K events) (pseudo-experiments).

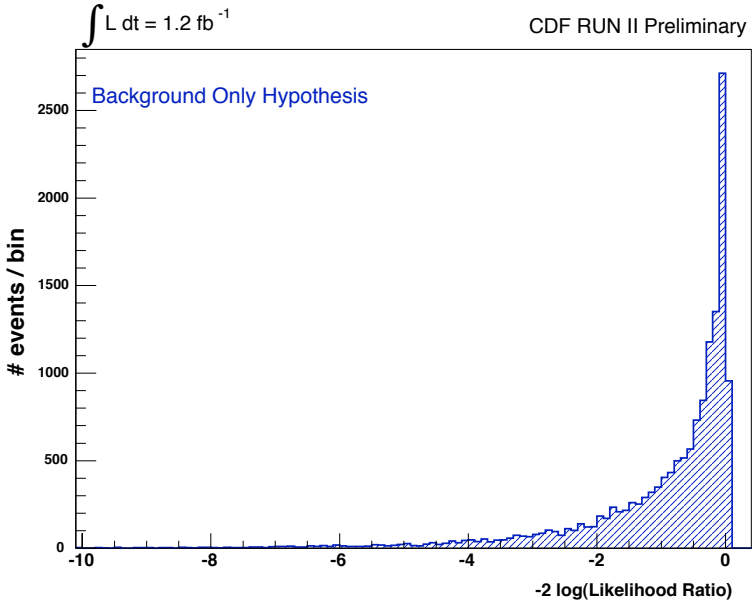

Figure 6.17: Likelihood ratio for the B only hypothesis (10K events) (pseudo-experiments).

Chapter 7

Analysis Results and Systematics

In this chapter the results of the analysis are presented: the likelihood fit after the data are *unblinded*, the cross section measurement and a cross section limit. This measurement is statistically limited, however there are significant sources of systematic uncertainties too, which are also presented here.

7.1 Likelihood Fit on Data

After unblinding the data, the parameters α, β and f_S are fitted simultaneously in the dijet invariant mass range [45,160]GeV. The background parameters (second line on Table 6.3) are measured to be compatible with the values given by the sidebands. The signal fraction is measured to be $f_S = 0.027 \pm 0.014$. We measured 15016 total number of events, that correspond to 410 ± 212 signal events. From the Standard Model MC studies presented in Section 6.2.3, we were expecting to measure 15035 ± 123 total events, out of which 554 ± 24 signal events.

The likelihood fit on the data, as well as the background estimation, are shown in Figures 7.1 and 7.2. Figure 7.3 shows the signal shape measured with the data. The expected shape and the shape we see with the data agree well.

The number of events that we measure is compatible, within the statistical errors, with the expected number of events. In the same conclusion we arrive by comparing the most probable expected likelihood ratio to the likelihood ratio taken by the data (Figure 7.4): we had a $\approx 25\%$ probability to get a signal fraction as low or lower than the one we actually measured.

Following the procedure described in Section 6.3.3, we estimate a statistical significance for the measurement of 1.94σ (Figure 7.5). This number is compatible with the statistical significance that the fit result gives.

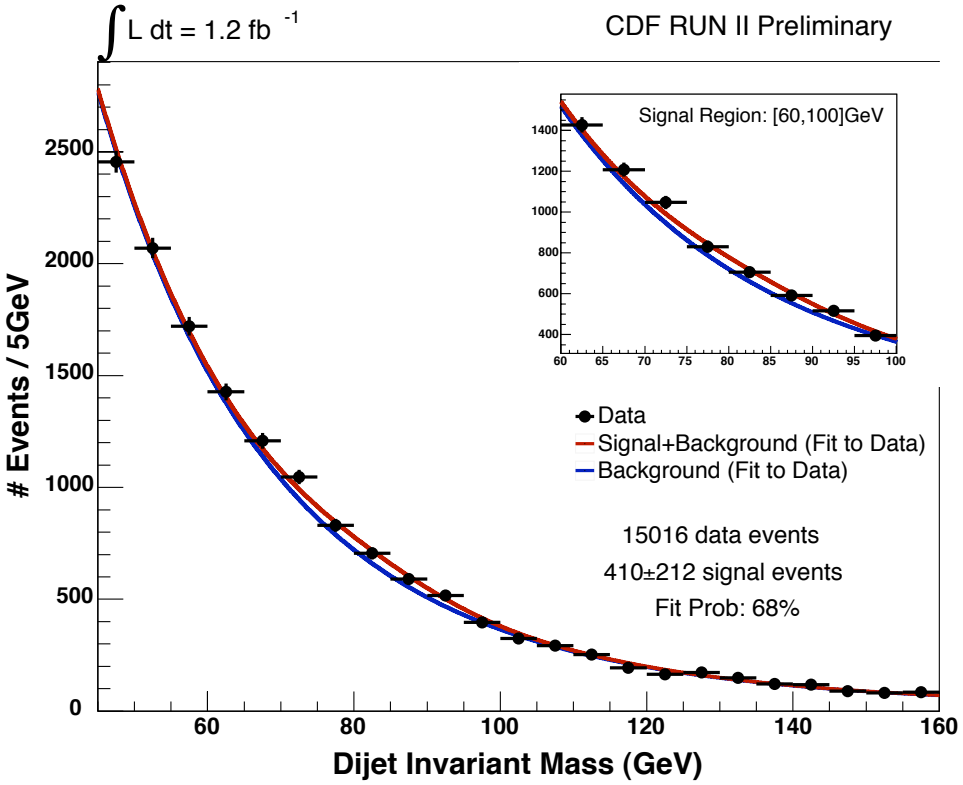

Figure 7.1: Likehood fit on data (red line). The blue line shows the background estimation.

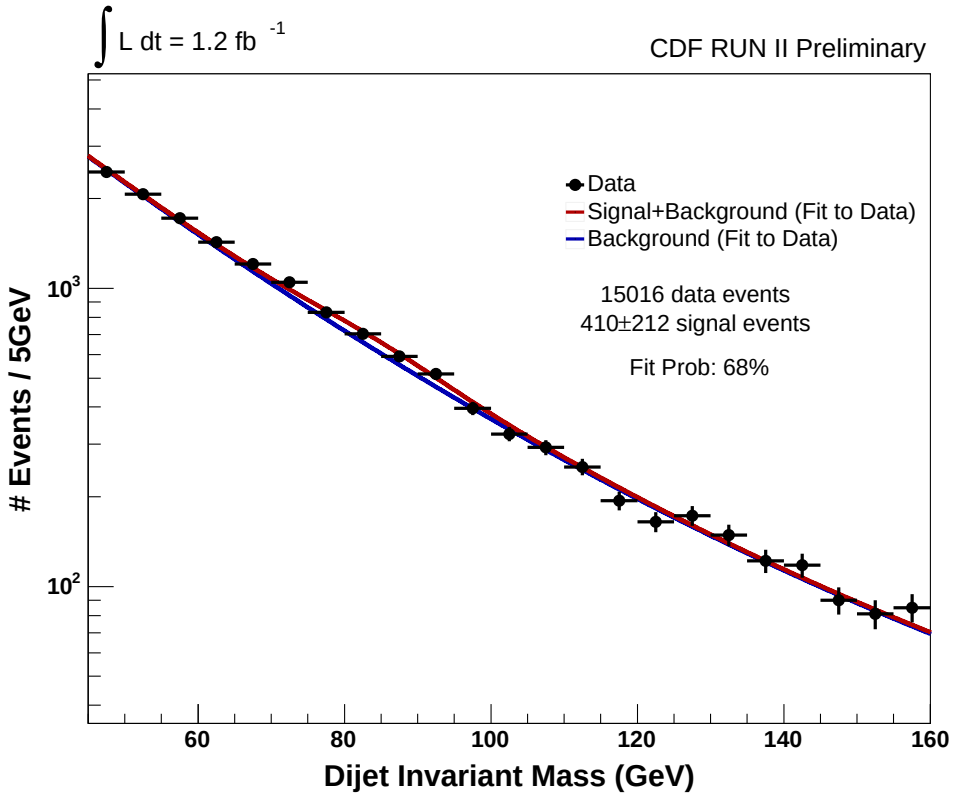

Figure 7.2: Likehood fit on data (red line). The blue line shows the background estimation - log scale.

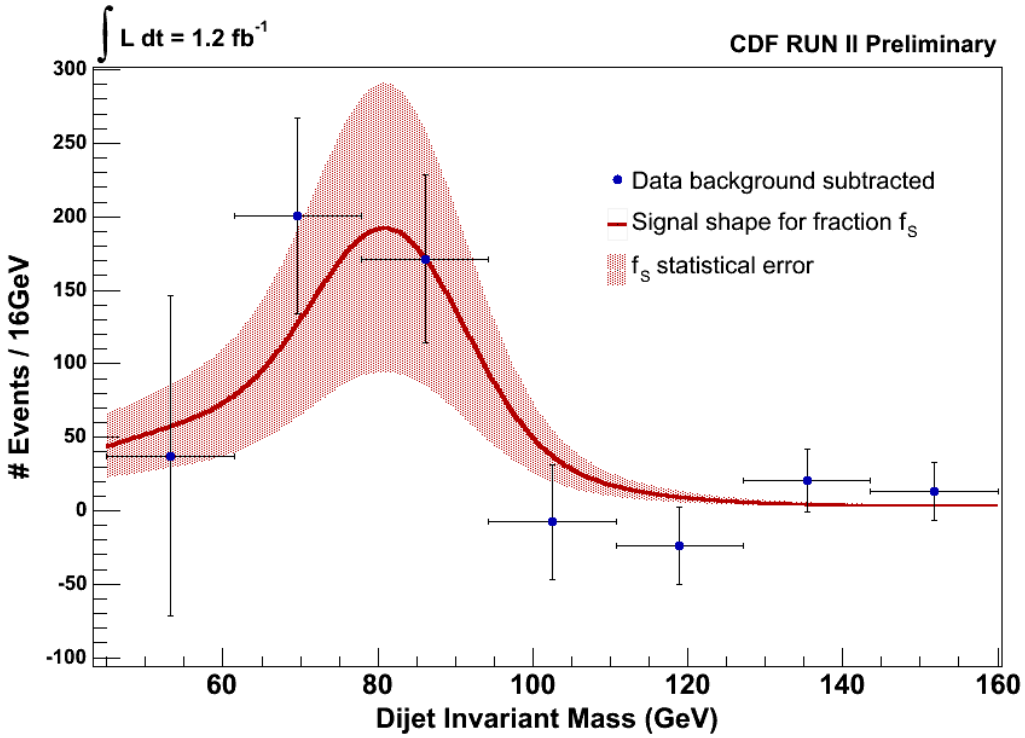

Figure 7.3: The signal shape measured on data. The plot is made by subtracting the measured background shape from the data. The red line corresponds to the MC shape for the measured signal fraction. There is a good agreement between the MC shape and the shape seen in the data.

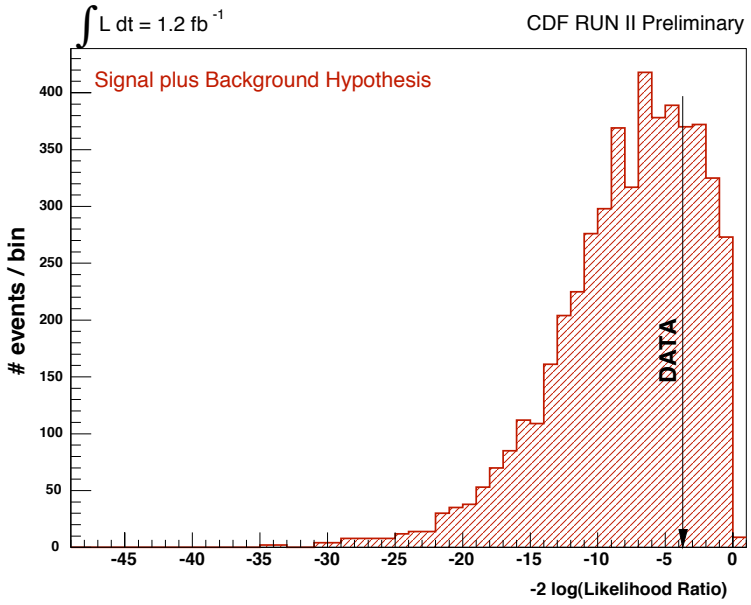

Figure 7.4: Likelihood ratio for the S+B hypothesis (5K events).

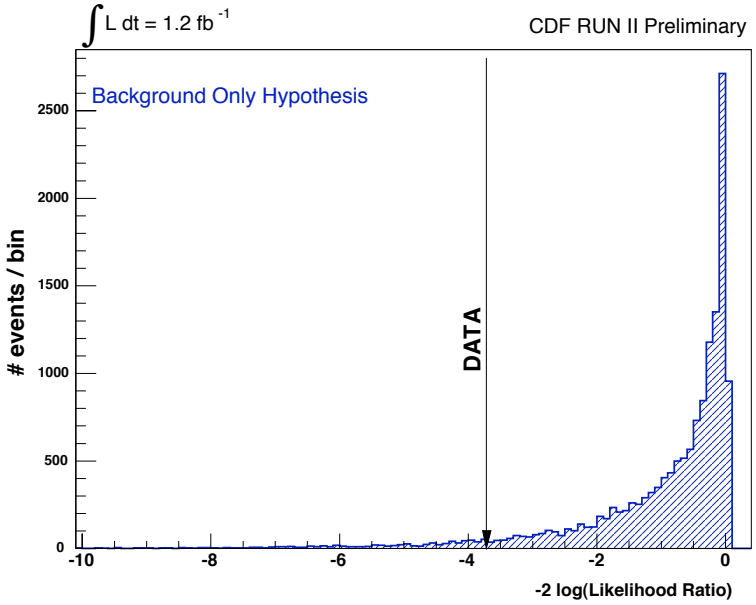

Figure 7.5: Likelihood ratio for the B only hypothesis (10K events).

7.2 Cross Section

To estimate the cross section that corresponds to the decay channel of this analysis, we use the formula[1]

$$\sigma \times Br = \frac{N_{Signal}}{\sum_{\ell}(\alpha cc_{\ell}^{WW/WZ} \times \epsilon_{\ell}) \times \mathcal{L}}$$

where

- N_{Signal} is the number of signal events that we measure. We have measured 410 ± 212 signal events.
- $\alpha cc^{WW/WZ}$ is the MC acceptance. It is defined as

  $$\alpha cc^{WW/WZ} = \frac{N_{Reco}}{N_{Gene}^{|Z_0|<60cm}}$$

  where N_{Reco} is the number of MC events that pass the event selection and $N_{Gene}^{|Z_0|<60cm}$ is the number of MC events generated within $|Z_0| < 60cm$ (requirement that ensures the good COT tracking efficiency). Given that the signal of this analysis is composed of two contributions (WW and WZ), we estimate the acceptance as

  $$\alpha cc^{WW/WZ} = \frac{\sigma^{WW(\ell\nu jj)} \times \alpha cc^{WW(\ell\nu jj)} + \sigma^{WZ(\ell\nu jj)} \times \alpha cc^{WZ(\ell\nu jj)}}{\sigma^{WW(\ell\nu jj)+WZ(\ell\nu jj)}}$$

  For each lepton type, the values of αcc are given in Table 7.1.
- ϵ is a mean efficiency scale factor. It is calculated using the scale factors of Table 5.2. More precisely:

  $$\epsilon_i = \epsilon^{DATA-MC} \times \epsilon^{VTX} \times \epsilon^{TRCK} \times \epsilon^{TRIG}$$

  $$\epsilon = \frac{\sum_i \epsilon_i \times \mathcal{L}_i}{\sum_i \mathcal{L}_i}$$

  with the index i refearing to each of the 3 datasets ($0d, 0h, 0i$, Table 5.1). For each lepton type, the values of ϵ are given in Table 7.1.
- $\sum_{\ell}$ is the sum of $\alpha cc^{WW/WZ} \times \epsilon$ over the different lepton types (CEM, CMUP, CMX), Table 7.1. We calculate the sum to be 0.228.

[1] We referred to this formula when the luminosity was described. We then used the formula in its simpler format $N = \sigma \times \mathcal{L}$.

	CEM	CMUP	CMX
αcc	0.138	0.082	0.035
ϵ	0.129	0.067	0.032

Table 7.1: Acceptance and efficiency for the different lepton types.

- $\mathcal{L}$ is the total luminosity we have processed ($\mathcal{L} = 1210$ pb^{-1})

Taking into account only the statistical error in the number of signal events we measure

$$\sigma \times Br = 1.94 \pm 0.77 \text{ pb}$$

that is compatible with the theoretical prediction for the cross section [5]

$$\sigma_{theory} \times Br = 2.09 \pm 0.14 \text{ pb}$$

95% CL upper limit

We will set a 95% CL upper limit for the measured cross section. Assuming that the measurement follows a gaussian distribution, we can use simple bayesian statistics for the limit. The 95% CL upper limit corresponds to a one-sided confidence interval: we want to find what is the value for which there is 95% probability that the cross section is indeed as low of lower. Considering a standard Gaussian PDF $\varphi(\chi)$, we want to find out how many standard deviations away from zero the integral that corresponds to the one-sided tail will be 5% (shaded area in Figure 7.6) [2].

We can use the inverse standard Gaussian function Φ^{-1} to estimate this number of standard deviations; for a one-sided 95% confidence interval, we find that the number of standard deviations is 1.645. The 95% CL upper limit can therefore be set by the estimated value plus 1.645 standard deviations [43]. Therefore, the 95% CL upper limit we set for the cross section is

$$\sigma \times BR < 2.76 \; pb$$

[2] This statement can be of course generalized for any $(1-\alpha)$% one-sided confidence interval, as shown in the picture.

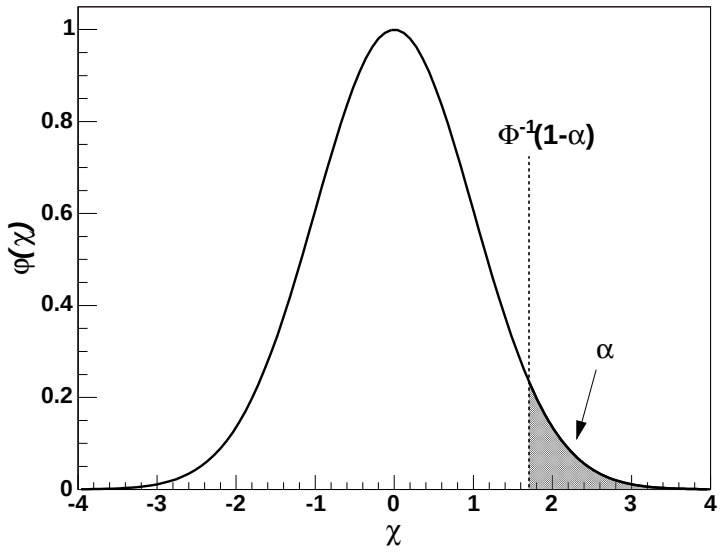

Figure 7.6: The standard Gaussian PDF $\varphi(\chi)$ showing the relationship between the inverse standard Gaussian Φ^{-1} and the confidence level, for a one-sided confidence interval.

7.3 Systematics

7.3.1 What are *Systematics*?

All the errors we have interpreted so far are statistical errors. They address an uncertainty in a statistical basis: if not just a single CDF experiment would exist, but hundreds of CDF experiments, then the data from these experiments would correspond to results different from the current one, but within the statistical error we defined.

In the measurement we performed, various assumptions were made. We assumed that the MC description of the signal shape is exact, and used in the likelihood fit as such; we assumed that the background shape is indeed a two-parameter function of the dijet invariant mass; we assumed that the luminosity is exact; etc. However, we don't know if these assumptions were indeed correct.

A measure of the quality of the various assumptions we have made in the analysis is given by the systematic uncertainties. In fact, *A systematic uncertainty is, in any statistical inference procedure, the uncertainty due to incomplete knowledge of the probability distribution of the observables* [44].

For the measurement we performed, we need to address separately two kinds of systematics: those that affect the significance of the measurement, and those that affect the cross section. In the first category the uncertainties is the signal fraction measurement are interpreted. These uncertainties can affect the conclusion about the significance. The uncertainties in the signal fraction, together with the uncertainties in the acceptance and the luminosity are giving the overall uncertainty in the cross section.

7.3.2 Systematic Uncertainties

Systematics affecting the signal fraction

- *Jet Energy Scale (JES)*: The energy scale of the jets is corrected for various factors, as already described in an early chapter. Each of the corrections of the jet energy scale carry an uncertainty and the quadratic sum of these uncertainties is what we study as Jet Energy Scale (JES) uncertainty. The JES is shifted $\pm 1\sigma$ on an event by event basis. Given that the background is defined using data, variations in the signal description as given by MC will only be considered. The JES is performed for all corrections up to level 7,

and taken into account in the $\not\!\!E_T$ corrections as well. The signal shape is parameterized for the two cases of variations. Toy MC is generated using the new parameterization, and fitted with the standard signal parameterization. The difference in the fit is taken as the systematic error, and is evaluated to be 10%.

- *Jet Resolution ($\Delta\sigma_{Jet}$)*: This systematic uncertainty gives an estimation of the dependence of the result on the signal dijet invariant mass resolution. It is estimated by a 10% Gaussian smearing[3] of the jet resolution, on a jet by jet basis[4]. The smeared out signal shape is parameterized, and toy MC is generated according to the new parameterization, and fitted with the standard one. The systematic uncertainty due to resolution is estimated to be 10%.

- *Background shape*: The background shape was fit to the following form

$$PDF_{BGR} = exp(\alpha x + \beta x^2)$$

that has two parameters α and β. The form gives an adequate fit to both the simulated Monte Carlo samples and the data. In order to investigate the systematic uncertainties on the background shape, fits with more parameters, from three to six, were carried out.

Figures 7.7-7.10 show the fits to the data with the different background parameterizations. The shift in the signal fraction as given by toy pseudo-experiments that use the difference parameterization but are fit with the initial one is also shown.

From the variation of the results on both the data and simulated samples from these fits a 20% systematic uncertainty was assigned.

- *Initial and final state radiation systematics (ISR/FSR)*: This systematic uncertainty studies the sensitivity of the signal shape to initial and final state radiation variations. To evaluate this systematic the ISR and FSR are varied

[3]The 10% has been defined using jet-photon balancing [45].

[4]Each jet p_T is multiplied by a factor that is a random number from a gaussian distribution $Gaus(Jet\ p_T, 0.1 \times p_T))/p_T$.

in the PYTHIA samples, following the Joint Physics group approach [46]. The following PYTHIA parameters are varied, as indicated in Table 7.2[5].

The signal shape as given by the different samples for the four different cases (more/less ISR/FSR) is parameterized each time, a toy MC is generated according to the new parameterization and fitted with the standard one. The systematic uncertainty due to the ISR systematic uncertainties is estimated to be 5% while the FSR systematic is found not to affect the signal fraction.

default ISR	PARP(61)=0.146	PARP(64)=1.0
more ISR	PARP(61)=0.292	PARP(64)=0.5
less ISR	PARP(61)=0.073	PARP(64)=2.0
default FSR	PARP(72)=0.146	PARP(71)=4.0
more FSR	PARP(72)=0.292	PARP(71)=8.0
less FSR	PARP(72)=0.073	PARP(71)=2.0

Table 7.2: PYTHIA settings for ISR and FSR variations. Note that in order for these settings to be used, one needs to set MSTP(3)=1 and then provide the default values manually.

Adding all the systematic uncertainties affecting the signal fraction in quadrature, we get a total systematic error of 25%. The total number of signal events we measure becomes:

$$N_{Signal} = 410 \pm 212(stat) \pm 102(sys)\ signal\ events$$

The systematic error will affect the significance of the measurement. Assuming that all the systematic sources are uncorrelated with each other and that the systematic error is uncorrelated with the statistical error, we can add the statistical and systematic errors in quadrature and get a total error of ϵ_{TOT} =235 events. This error brings the significance of the measurement to 1.7σ.

[5]Describing the meaning of each of the PYTHIA parameters is too technical for the purpose of the thesis, so I just refer to them. More information can be found in the PYTHIA manual [36].

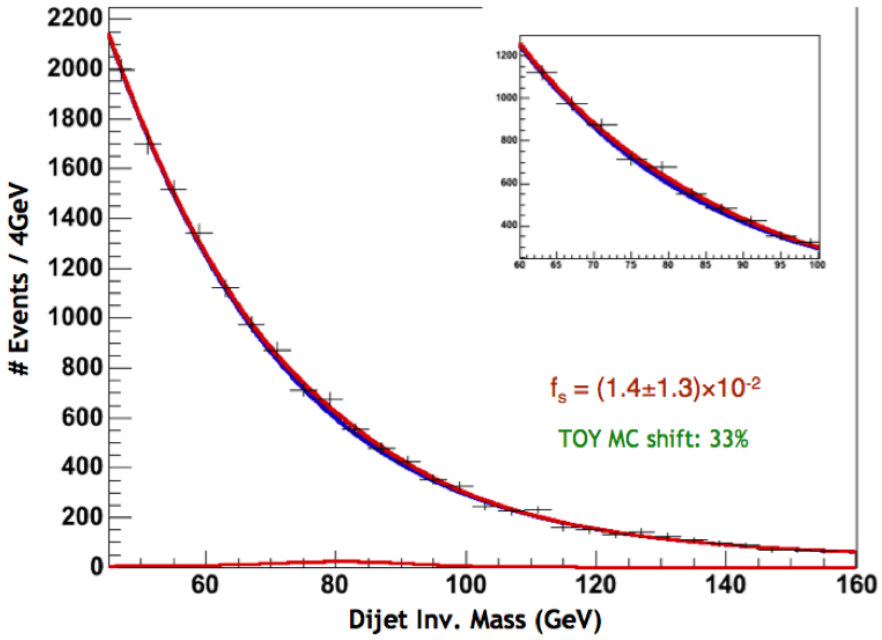

Figure 7.7: Fit to data performed using a 3-parameter background description.

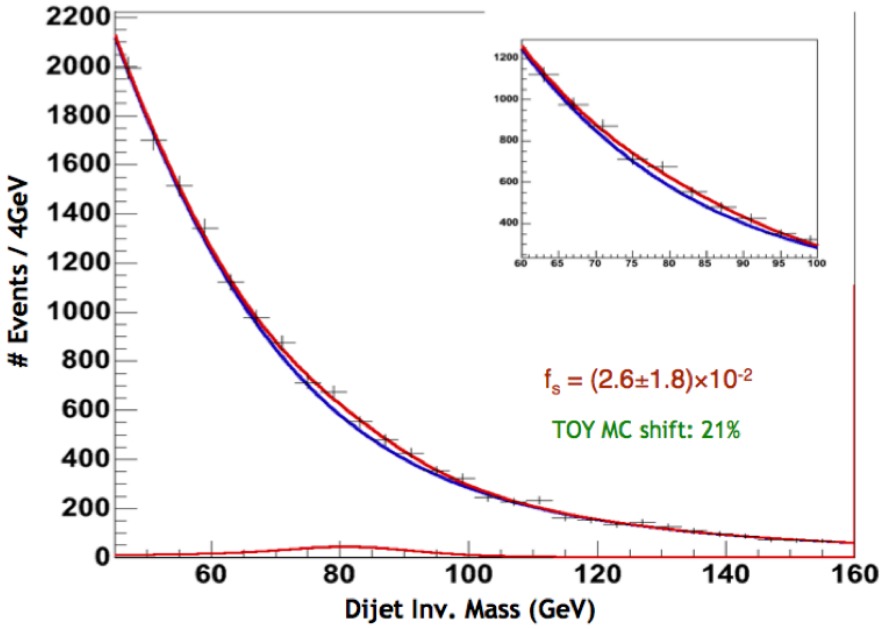

Figure 7.8: Fit to data performed using a 4-parameter background description.

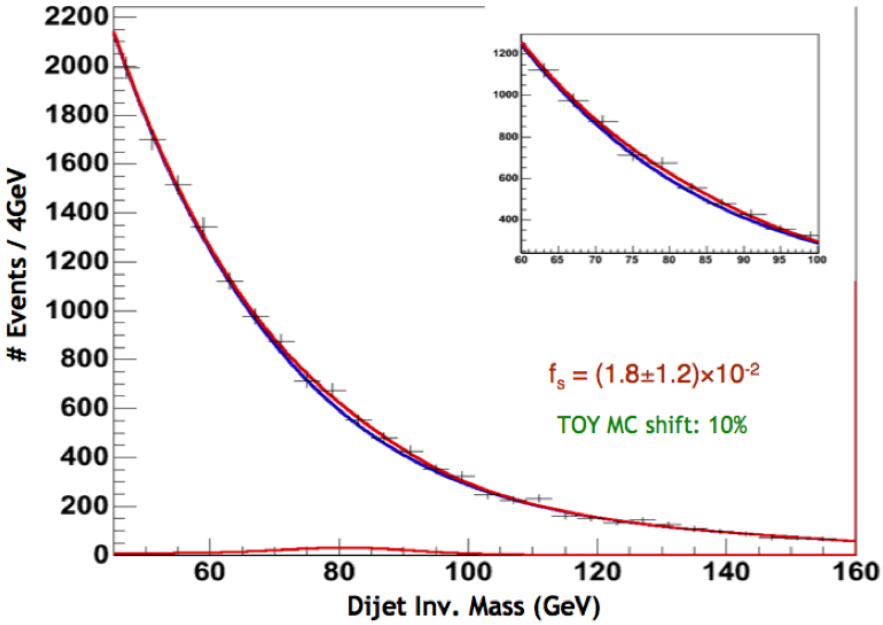

Figure 7.9: Fit to data performed using a 5-parameter background description.

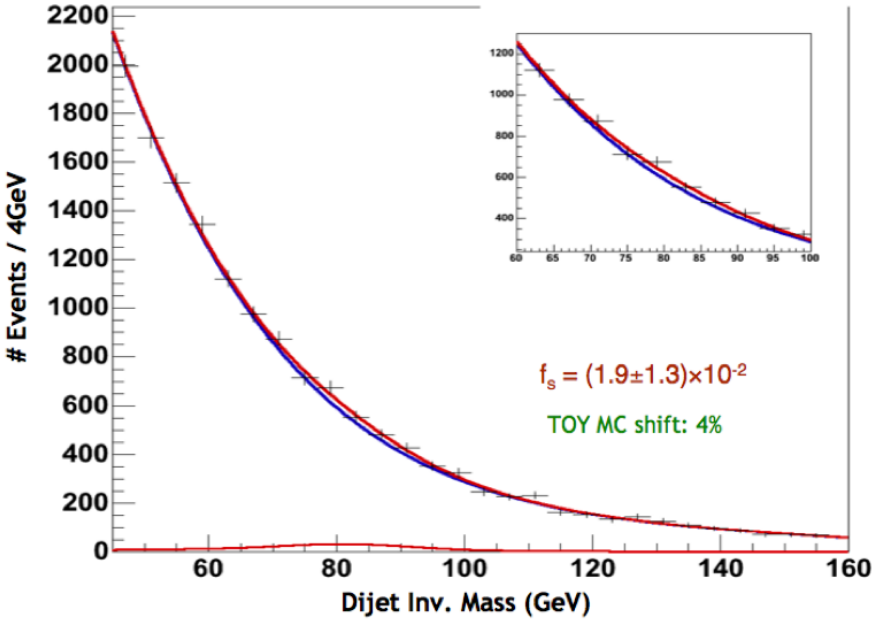

Figure 7.10: Fit to data performed using a 6-parameter background description.

Systematics affecting the acceptance

- *JES*: We count the number of events that pass the selection cuts, after varying the JES. We see that the uncertainty is 3%.

- $\Delta\sigma_{Jet}$: No differences are measured by changing the jet resolution.

- *ISR/FSR*: We count the number of events that pass the selection cuts after varying the ISR and FSR in the WW inclusive PYTHIA samples (as described in the previous session). We measure an uncertainty of 2% for each of the ISR and FSR.

- *Lepton W (PDF, scale factors and efficiencies)*: This interprets the uncertainties in the efficiencies and scale factor we have used. There is a standard 3% uncertainty.

In total, the systematic uncertainty affecting the acceptance is estimated to be 5%.

Systematics affecting the luminosity

As already described in the luminosity measurement method, the luminosity measurement has a 6% systematic uncertainty [21].

Systematics propagation in the cross section

The systematic uncertainties are propagated in the cross section using the error propagation formula, that gives

$$(\frac{\delta\sigma}{\sigma})^2 = (\frac{\delta\alpha}{\alpha})^2 + (\frac{\delta N_{Signal}}{N_{Signal}})^2 + (\frac{\delta\mathcal{L}}{\mathcal{L}})^2$$

This leads to a systematic uncertainty of 26% to be assigned in the cross section. The cross section becomes

$$\sigma_{WW/WZ} \times Br(W \to \ell\nu, W/Z \to jj) = 1.47 \pm 0.77(stat) \pm 0.38(sys)\ pb$$

The 95% CL upper limit to the cross section is estimated to be (including the systematic uncertainties)

$$\sigma \times Br < 2.88\ pb$$

A summary of all systematic uncertainties the affect the result of this analysis is given in Table 7.3.

Source	**Effect in Signal Fraction**
Jet Energy Scale	10%
Jet Resolution	10%
Background Shape	20%
ISR	5%
FSR	< 1%
Source	**Effect in Acceptance**
Jet Energy Scale	3%
Jet Resolution	< 1%
ISR	2%
FSR	3%
W leptonic	3%
Source	**Effect in Cross Section**
Total Signal Fraction	25%
Total Acceptance	5%
Luminosity	6%
Total Effect in Cross Section	26%

Table 7.3: The systematic uncertainties and their effect in the signal fraction, the acceptance and finally the cross section.

7.4 Summary

In this chapter, a search for WW plus WZ production in lepton-neutrino plus dijet final state, using 1.2 fb^{-1} of data, has been presented. An ANN has been used for the significance optimization. MC studies showed an $\approx 2.5\sigma$ expected effect, but on data we saw a statistical 1.9σ effect. Including systematic uncertainties, the significance of the measurement is 1.7σ. The theoretical prediction for the cross section is

$$\sigma^{theory}_{WW/WZ} \times Br(W \to \ell\nu, W/Z \to jj) = 2.09 \pm 0.14\ pb$$

We measured

$$N_{Signal} = 410 \pm 212(stat) \pm 102(sys)\ signal\ events$$

that correspond to a cross section

$$\sigma_{WW/WZ} \times Br(W \to \ell\nu, W/Z \to jj) = 1.47 \pm 0.77(stat) \pm 0.38(sys)\ pb$$

The 95% CL upper limit to the cross section is set at

$$\sigma \times Br < 2.88\ pb$$

Chapter 8

Future Perspectives

In this chapter, the future perspectives of this signature are summarized, perspectives not only at the CDF experiment, and the Tevatron, but also at the LHC, where unprecedented energy scales will be reached.

8.1 Significance Improvements

The search for WW and WZ production in the semi-leptonic decay channel, that is presented in this thesis, is strongly limited by statistics at the current phase. The analysis is performed using 1.2 fb^{-1} of data, while there are currently about twice this amount of data on tape at CDF to be analyzed. Making a simple extrapolation of the expected statistical significance ($\approx 2.5\sigma$ at 1.2 fb^{-1}) at the currently available luminosity, one would expect to see an at least 3.5σ effect, what would be the first evidence for diboson production in the semi-leptonic decay channel, at hadron colliders. In fact, this would also be the first generic dijet resonance evidence at hadron colliders. Except from the challenge of observing it, this channel has also sensitivity for new physics evidence via the anomalous triple gauge couplings, as already explained in the theoretical introduction.

The significance of the measurement can be improved not only by adding more data but also by improving the analysis methodology.

In the current phase, we use the ANN output to perform a cut, and we fit the dijet invariant mass shape of the events that pass this cut. By using the ANN output itself to perform a fit, the significance would be possibly better. In such an approach, the ANN training could include variables such as the invariant mass itself, the separation between the signal and the background would therefore be stronger

in the output plot (e.g. Figure 8.1). Further investigation is of course needed on that point, since the systematics could be enhanced by the use of such technique.

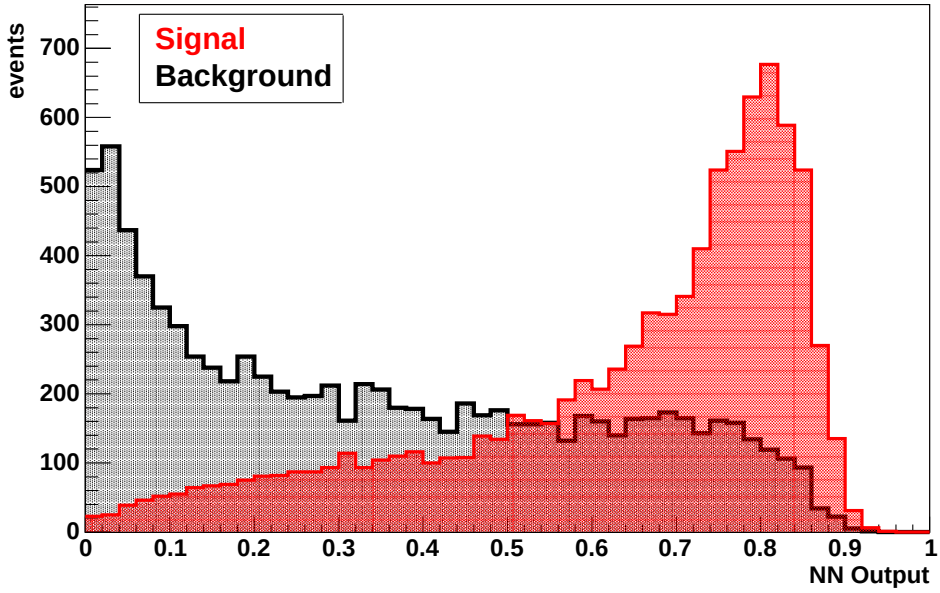

Figure 8.1: ANN output for training in the invariant mass range [40,160]GeV. The invariant mass itself has been used for the training. The signal to background separation looks promising but the effect of systematics has not been investigated. Note: The shapes are normalized in integral, not in relative cross section.

Another possible way of significance improvement, using still the current approach of the analysis, would be to improve the dijet invariant mass resolution. This was investigated at an early phase of the analysis using the so call *H1 algorithm*[1] for the jet reconstruction. In this algorithm information from the COT tracker is used in the jet reconstruction; each calorimeter jet is matched to a track in the COT, improving that way the energy resolution. When this algorithm was tested, it was still at a preliminary phase and the jet corrections were not sufficiently applied. The improvement was therefore not very significant, and for this reason the algorithm was dropped at the time. However, the calibrations in the H1 algorithm are currently applied, and the resolution has been seen improved in other signatures [47].

[1]Name inspired from the HERA H1 collaboration, where the algorithm was first used and from where it was imported into CDF.

8.2 Triple Gauge Coupling Measurements

A summary of the TGC theory is given in the theoretical introduction of the thesis. The parameters of the couplings that we want to measure are the $\Delta g_1^Z = \Delta g_1^\gamma$, $\Delta\kappa_Z = \Delta\kappa_\gamma$ and $\lambda_Z = \lambda_\gamma$ (with $V = Z, \gamma$), all zero within the SM.

In order to interpret the cross section limit that has been set in this analysis as a limit in the triple gauge coupling parameters, an NLO MC simulation program, called *MCFM*[2] has been used. Using MCFM and for $\Lambda = 1.5$ TeV, we perform a scan of the cross-section of the process $WW \to \ell\nu jj$ for the parameters $\Delta\kappa$ and λ, each time keeping the parameter Δg fixed to zero. One of the two parameters, $\Delta\kappa$ or λ, depending on the parameter of the actual scanning, is also fixed to zero. Making the assumption that the WZ contribution does not affect significantly the trend of the cross section dependence on the TGC parameters, we rescale the cross section given by MCFM to the total theoretical $WW + WZ$ cross section for the SM point (zero for each parameter). From the cross-section plots (Figures 8.3 and 8.2) and using the cross section limit (including systematics) we set limits on the TGCs at

$$(\lambda, \Delta\kappa) = ([-0.36, 0.36], [-0.36, 0.50])$$

These limits are not optimal, they are in fact comparable to the limits[3] set with this decay channel, 350 pb^{-1} of data but a dedicated analysis that used the leptonic W p_T as a variable to extract limits, that is more sensitive to the anomalous couplings than the cross section [26].

Preliminary studies have been performed for a dedicated analysis for TGC limits. Using MCFM, various variables have been tested for the sensitivity to anomalous TGCs. One of the most sensitive variables is found to be the $H_T \equiv \sum_{all\ objects}(p_T)$ (Figure 8.4). This is an example of a variable whose tails, which are characterized by good signal over background ratio and high sensitivity to anomalous couplings, could be used to set stringent limits in the TGC parameters.

Once the search for the semi-leptonic WW and WZ production is updated with more data and the result becomes more significant, the limits to the aTGC parameters will become the most stringent.

[2] Monte Carlo for FeMtobarn processes

[3] $(\lambda, \Delta\kappa) = ([-0.29, 0.29], [-0.51, 0.45])$ using 350 pb^{-1}

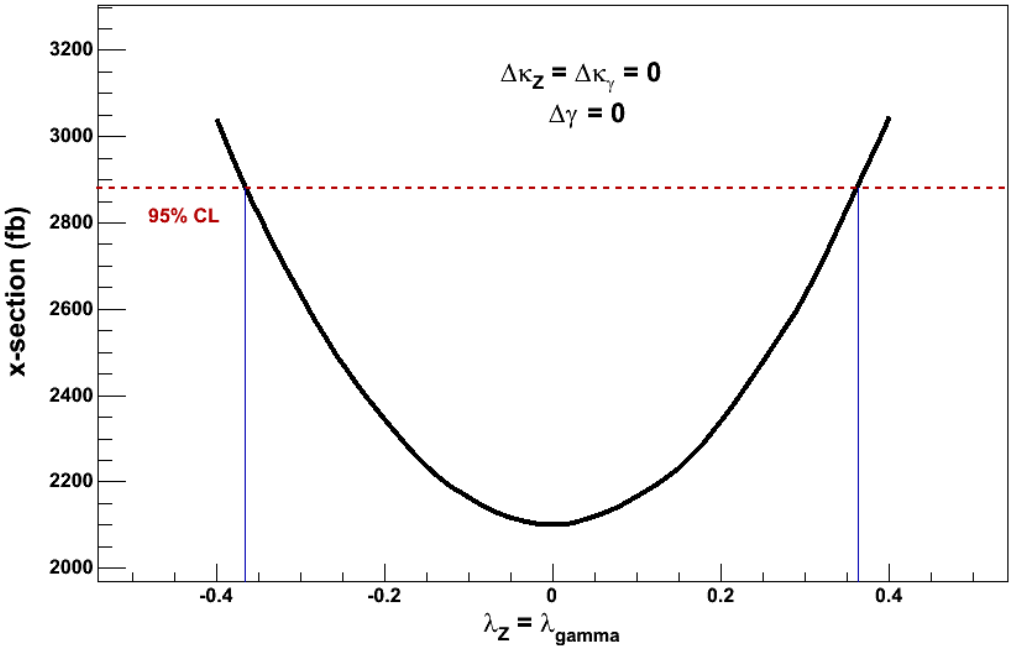

Figure 8.2: Limits on λ.

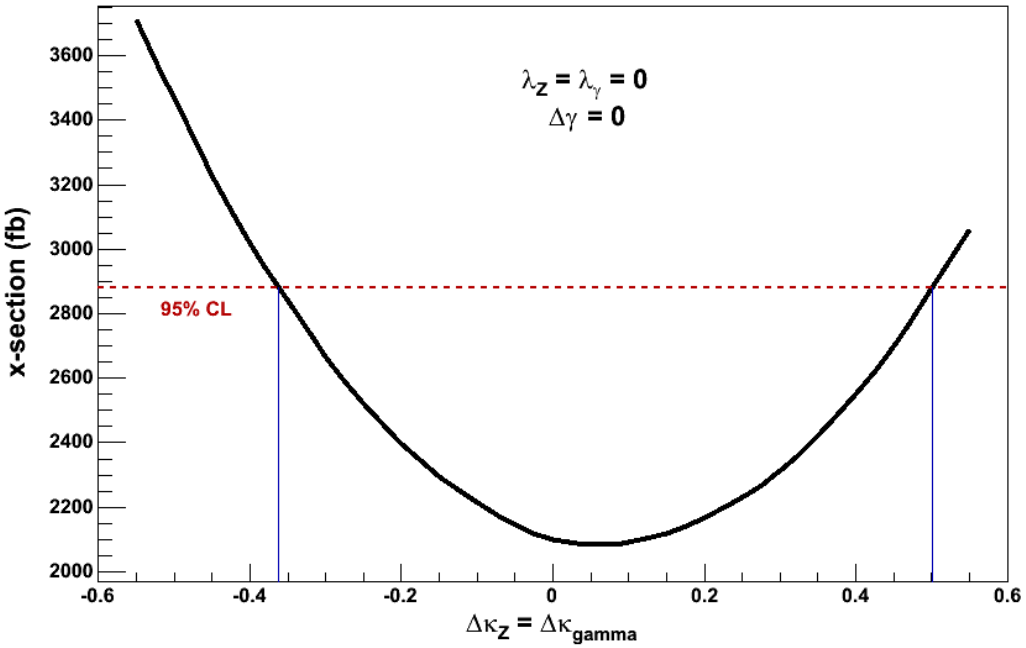

Figure 8.3: Limits on $\Delta\kappa$.

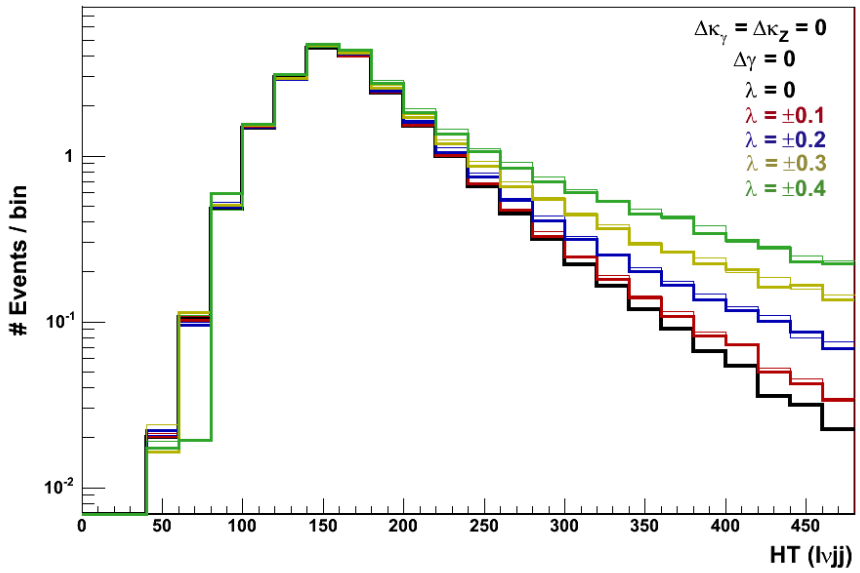

Figure 8.4: λ variations for the H_T variable. The $\Delta\kappa$ and Δg parameters are set to 0.

8.3 $WW/WZ \rightarrow \ell\nu_\ell + jets$ at the LHC

The LHC will probe a new energy range that is expected to reveal new particles and new phenomena. From the start-up, physicists will search for their direct or indirect evidence. Diboson processes will have a particular interest: unobserved particles, such as the Higgs, have experimental signatures with diboson states and deviations from the SM in the diboson production itself could manifest as anomalous TGCs. It is not surprising that both LHC experiments have very advanced physics programs that involve diboson signatures.

The production cross section for all the physics processes will be higher at the LHC with respect to the Tevatron, and such will be the case for the diboson production too (Figure 8.5). Particularly enhanced will be the signatures produced by gluon fusion, like the $t\bar{t}$ production. In fact, about 90% of the $t\bar{t}$ events at the LHC will be produced by gluon fusion while the quark-antiquark annihilation only contributed about 10% ([48]). In the case of the diboson production however, the enhancement is not as big. The gluon fusion process $gg \rightarrow WW$ does contribute to the diboson production, but only at about 5% ([49]). Studying the semi-leptonic diboson decays at the LHC will therefore become more difficult than at the Tevatron;

the significant backgrounds will be not only the $W + jets$ but also the $t\bar{t}$ production. Unfortunately, there are not ongoing studies for this channel in either of the two experiments. The diboson studies are currently limited in the fully leptonic decay channels.

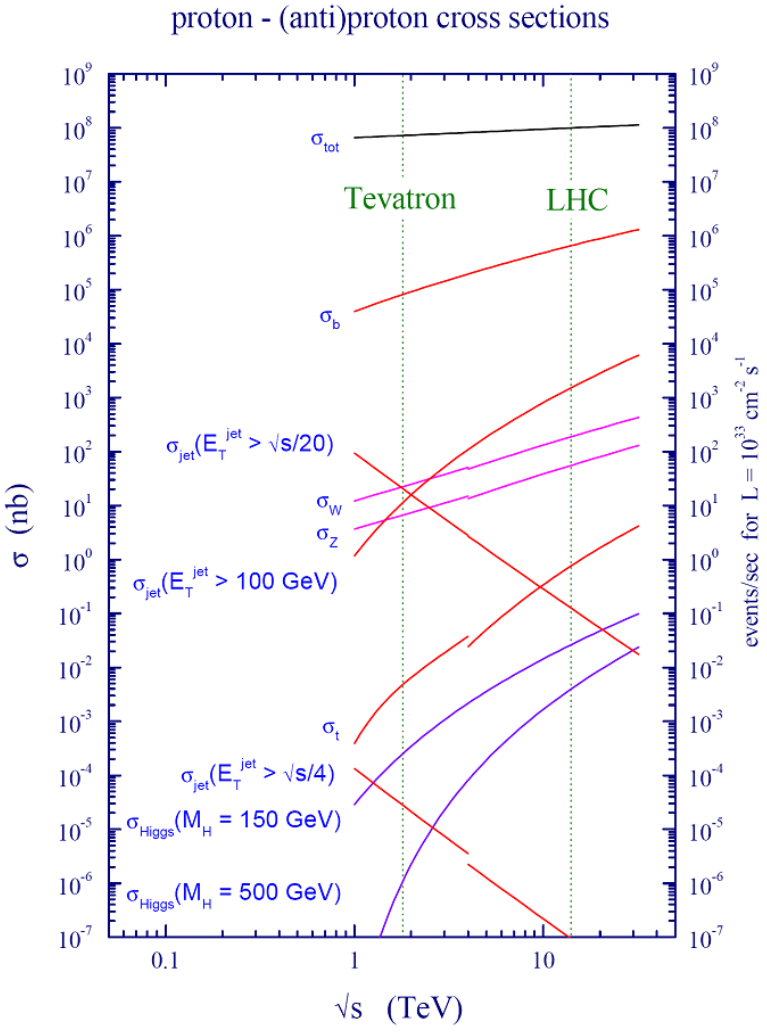

Figure 8.5: Projection of various production cross sections form the Tevatron to the LHC. The single boson production is enhanced by a factor of 10, the diboson production cross section is therefore expected to be at least 100 times larger at the LHC.

Part II

Silicon module production and detector control system at the ATLAS SemiConductor Tracker

Chapter 9

The ATLAS detector

The *Large Hadron Collider (LHC)* at CERN will extend the frontiers of particle physics with its unprecedented high energy and luminosity. Inside the LHC, bunches of up to 10^{11} protons (p) will collide 40 million times per second to provide 14 TeV proton-proton collisions at a design luminosity of 10^{34} cm^{-2}s^{-1}. The LHC will also collide heavy ions, in particular lead nuclei, at 5.5 TeV per nucleon pair, at a design luminosity of 10^{27} cm^{-2}s^{-1}.

The high interaction rates, radiation doses, particle multiplicity and energy, as well as the requirements for precision measurements have set new standards for the design of particle detectors. Two general purpose detectors, *ATLAS (A Toroidal LHC ApparatuS)* and *CMS (Compact Muon Solenoid)* have been built for probing pp collisions.

In this chapter an overview of the ATLAS detector is given. There is a wide range of documentation regarding the ATLAS detector (e.g. [51], [52], [53]), so only a brief overview will be given.

9.1 ATLAS Detector Overview

The detector concept has been developed considering a broad spectrum of detailed physics studies. The basic design criteria include:

- Fast and radiation-tolerant electronics and sensor elements, to deal with the experimental conditions of the LHC;

- High granularity of the detectors, to give the possibility to handle high particle fluxes and to reduce the influence of overlapping events;

- Multilayered tracking for heavy flavour tagging and high transverse momentum measurements at high luminosity;
- Precision electromagnetic calorimetry for electron and photon identification and measurements, and full-coverage hadronic calorimetry for accurate jet and missing transverse energy measurements;
- Muon spectrometry for good muon identification and high precision momentum measurement.

These considerations lead to the concept of the detector that is pictured in Figure 9.1. Its design provides large acceptance in pseudorapidity and full azimuthal angle (ϕ) coverage.

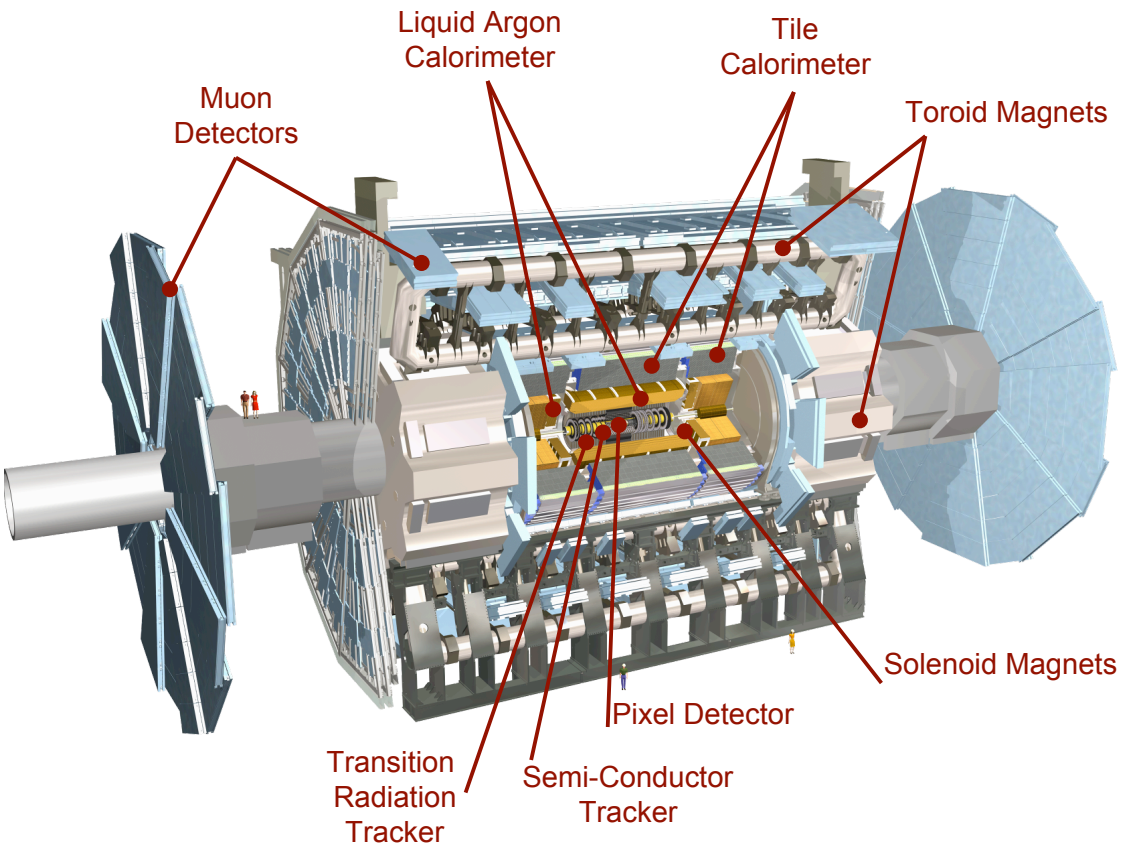

Figure 9.1: The ATLAS detector

ATLAS is the largest detector ever built for particle collider physics. Its diameter is 25 m, and its length 46 m. It weights approximately 7000 tons. Its size and complexity are required in order to cope with the high particle energy and multiplicity. The detector consists of 3 main sections. Located close to the beam axis, the tracking system employs pixel detectors, silicon microstrip modules and transition radiation straws, all within a 2 Tesla superconducting solenoid. The tracker is surrounded by the electromagnetic and hadronic calorimeters. In the outer part of the detector, 8 superconducting coils define an open toroidal magnetic field for muon detection.

9.2 Muon Systems

The shape and size of the ATLAS detector are defined by the toroid magnets (Figures 9.2 and 9.3), which surround the calorimeter. The muon chambers are immersed in the toroidal field. They are large-area gas-based detectors that provide measurements of the directions and momenta of high-energy muons which traverse the tracker and calorimeter. They provide a coverage of $|\eta| < 2.7$.

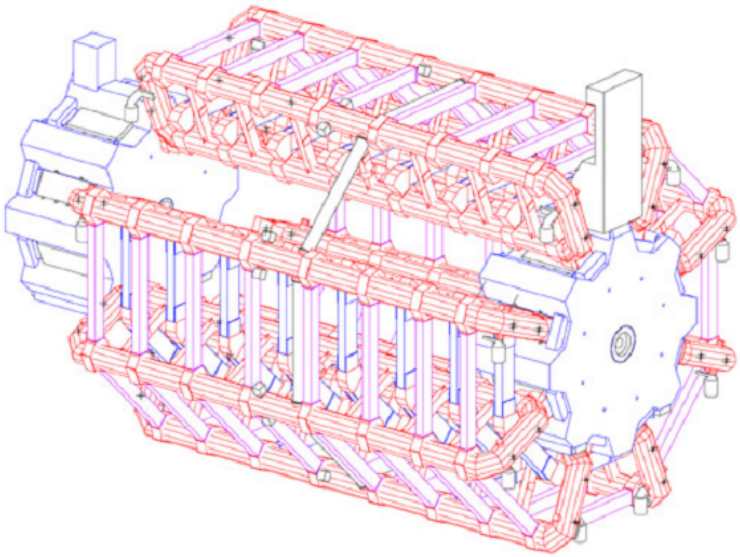

Figure 9.2: A drawing of the toroidal magnet system, that defines the muon system geometry.

The magnet system for the muon chambers is composed of eight superconducting air-coils in the barrel region and eight in each end-cap. The magnets generate a

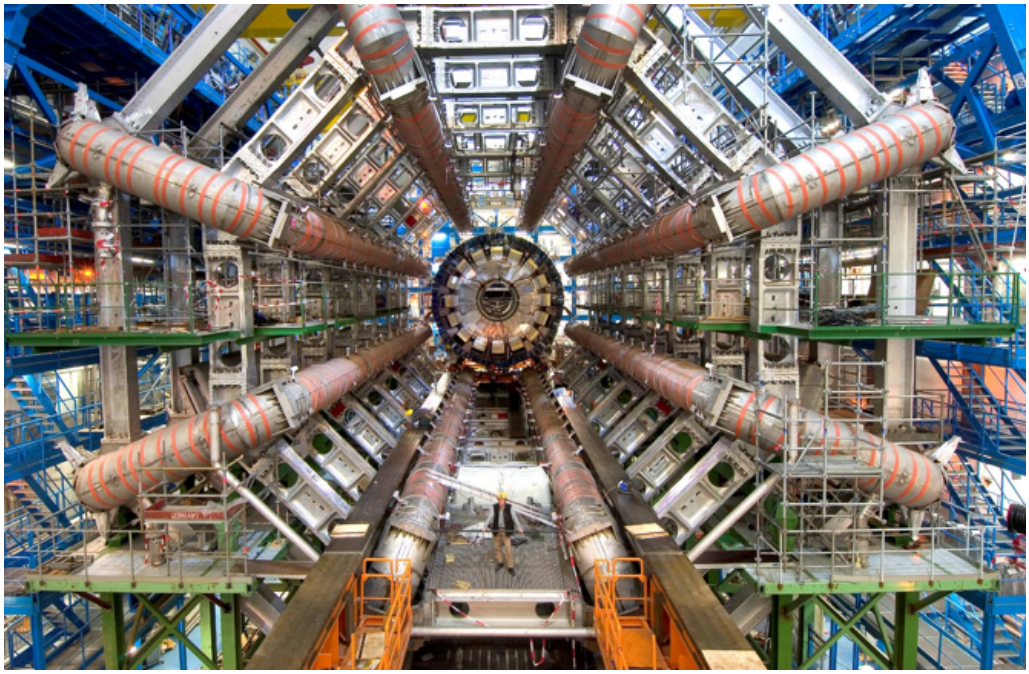

Figure 9.3: A photograph of the toroid magnets on place in the ATLAS pit.

magnetic field of up to 4 Tesla.

The muon spectrometer itself uses four different types of chambers: the Monitored Drift Tube (MDT) chambers, the Cathode Strip Chambers (CSC), the Resistive Plate Chambers (RPC) and the Thin Gap Chambers (TGC). The MDTs are used for precision tracking mesurements. They are located in both the barrel and the endcap regions and are supplemented by the CSCs in the very forward region. The RPCs (in the barrel region) and TGCs (in the forward region), arranged in stations located between the tracking chambers, provide the triggering.

The sheer size of the systems means that there are significant technical challenges related to the stability and alignment of the chambers and to the careful mapping of the detectors' magnetic fields over large volumes. The radiation levels for the muon chambers are much less severe than for the inner detectors or the calorimeters, but there are still concerns about aging of the systems and also the neutron radiation environment of the experimental halls where the detector sits. The design of the beam pipe and the shielding elements in the forward direction have been carefully optimized to reduce the neutron-induced background in the muon chambers.

9.3 Calorimetry

Good electron and photon identification, as well as position and direction measurements, are provided by a lead/liquid argon (LAr) sampling electromagnetic calorimeter with accordion shaped absorber plates in both barrel and endcap regions. The system's *accordion geometry* provides complete azimuthal symmetry, without cracks, and has been optimized for the high sampling rate environment of the LHC. The hadronic calorimeter, needed for accurate jet and missing transverse energy measurements, uses LAr sampling in the inner forward part and is surrounded by iron/scintillator sampling (Tiles) in the barrel and outer forward regions. The vertical tile geometry makes it easier to transfer the light out of the scintillator to photomultipliers and achieves good longitudinal segmentation.

A sketch of the ATLAS calorimeter system, that provides a coverage up to $|\eta| = 5$, is shown in Figure 9.4

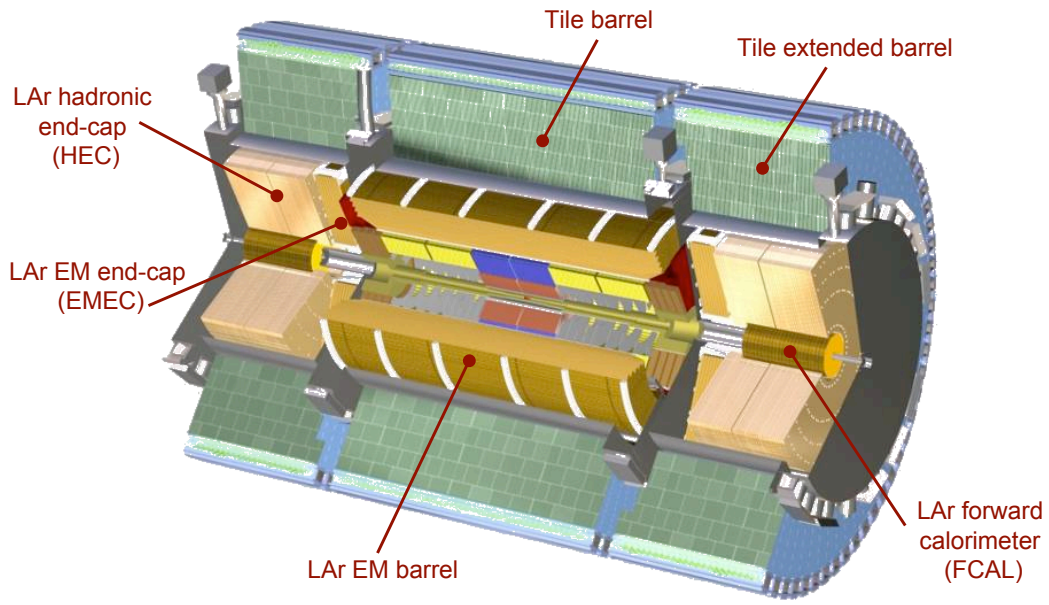

Figure 9.4: The ATLAS Calorimetry.

9.4 Tracking System

The tracking of ATLAS is provided by a multilayered Inner Detector (ID) placed within a 2 Tesla superconducting solenoid. It provides a coverage up to $|\eta| = 2.5$.

The design of the ID provides a good time and space resolution with the minimum possible material within the tracking volume.

The pixel detector is closest to the beam pipe. It consists of 3 barrels and 2 endcaps of 3 disks each, providing 3 tracking points. The proximity to the beam pipe and therefore the large amount of radiation makes this detector one of the most challenging parts of the ATLAS experiment.

The pixel detector is surrounded by the *SemiConductor Tracker (SCT)*, a detector that consists of more than 4000 double layered silicon strip detectors and therefore more than 6 million readout channels. The strip detectors are arranged in 4 coaxial barrels and 2 endcaps of 9 disks each, providing 4 space points per track. The SCT will be described in further detail in Section 10.1.

The TRT is the outer tracking layer. It employs individual drift tubes (straws) arranged in a barrel and two endcaps, providing continuous tracking (36 tracking points). It is built in modules with radii from 56 to 107 cm. The two endcaps have 18 wheels each.

A drawing of the ATLAS detector tracking system can be seen in Figure 9.5

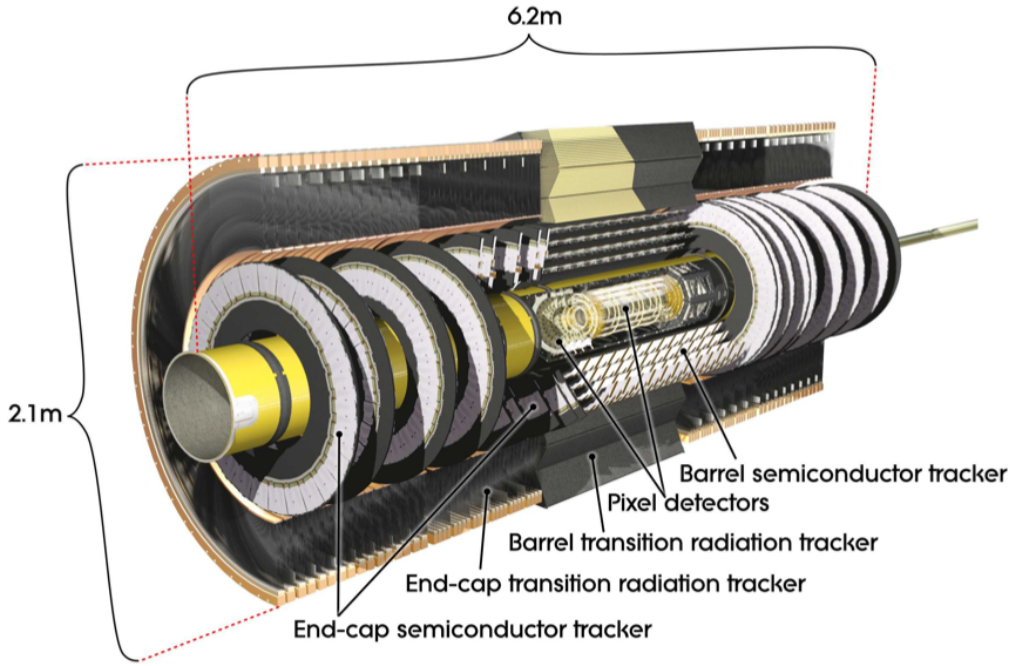

Figure 9.5: The ATLAS Inner Detector; a cut-away view.

9.5 Triggering

At design luminosity, the LHC will create 10^9 proton-proton events per second, but data storage and processing capabilities are such that data from only about 100-200 carefully selected events per second (each of them accompanied by an average of 25 overlapping proton-proton events in the same bunch crossing) can be recorded offline for complete analysis. Hence, there is a need for a trigger system to select only the most important physics signatures and achieve a rejection factor of nearly 10^7.

The ATLAS trigger is designed in three levels. The Level 1 uses information from the calorimeters and the muon detectors. Its input rate is the LHC bunch crossing (frequency of 40 MHz). The latency necessary to decide whether accept of reject an event is 2.5 μs and is obtained with pipelines at the sub-detectors level. The acceptance rate of the Level 1 trigger is 75 kHz (upgradable to 100 kHz). The Level 1 trigger identifies regions of interest for the event and passes the information coming from all the interested sub-detectors, to the Level 2. The Level 2 is built with farms of PCs and its acceptance rate is approximately 1 kHz with a latency of 10 ms. The events accepted by the Level 2 are processed and passed to the Event Filter representing the Level 3 trigger, which applies more sophisticated algorithms and calibrations to make a decision on acceptance or rejection of an event. The final ATLAS acceptance rate is about 100 Hz.

9.6 Summary

An overview of the ATLAS detector has been given in this chapter. In order for the expectations to be met regarding the ATLAS detector performance, dedicated and collaborative efforts have been made at many University and Laboratory facilities for the construction of the various detector components. In the following chapter, a description of the silicon tracker is given and the production of its building blocks at the University of Geneva assembly facility is summarized.

Chapter 10

The SemiConductor Tracker (SCT)

In this chapter, the *SemiConductor Tracker (SCT)* is described, together with the silicon modules, the building blocks of the SCT. A large fraction of the SCT modules has been produced at the University of Geneva and the production procedure is summarized.

10.1 The SCT

10.1.1 Description and Geometry

The SCT is designed to provide eight precision measurements per track in the intermediate radial range of the tracking system (between the innermost pixel layers and the outer TRT detector). It provides momentum and vertex measurements with high precision, given by the high granularity of the detector sensors.

The detector contains 61 m^2 of silicon detectors, making it an order of magnitude larger in surface area than previous generations of silicon microstrip detectors. The barrel region provides coverage up to $|\eta| = 1.4$ and the forward region covers $1.4 < |\eta| < 2.5$. The spacial resolution is 17 μm in $r - \phi$ and 580 μm in z. Tracks can be distinguished if separated by more than ≈ 200 μm.

The silicon microstrip modules are the building blocks of the SCT. The SCT consists of 4088 silicon modules, with a total of 6.3 million readout channels. They are arranged in 4 co-axial carbon-fiber barrels and 2 endcaps of 9 disks each (Figure 10.1). The four barrels are placed at radii of 30.0, 37.3, 44.7 and 52.0 cm and they are linked together. The endcap disks contain up to three rings of modules. All disks in an endcap are interconnected by a space-frame.

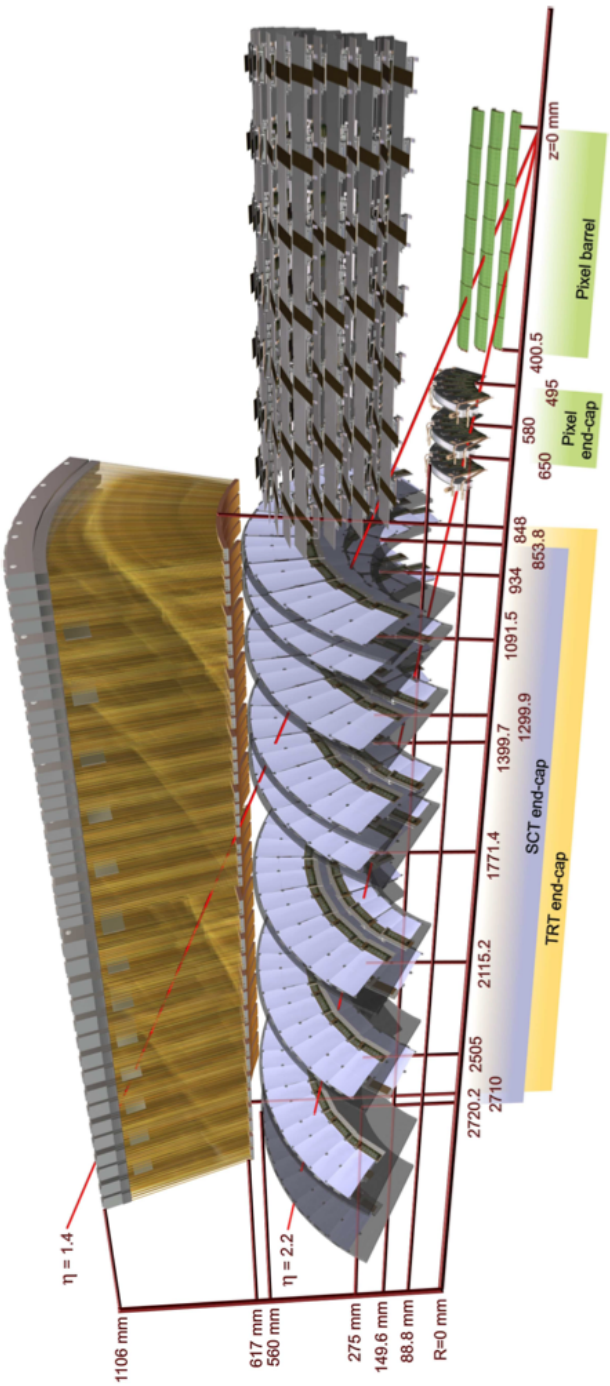

Figure 10.1: The ATLAS Semi Conductor Tracker (SCT), consisting of 4 co-axial barrel layers and 2 endcaps of 9 disks each.

Most modules consist of 4 silicon sensors[1] assembled in 2 daisy chained pairs that are glued back-to-back with a small stereo angle (40 mrad) and bonded to the Front End (FE) electronics hybrid. Each module has 1536 readout channels. The binary readout architecture is a cost-effective implementation meeting the performance requirements is resolution, signal-to-noise and speed [54]. Optical communication has been chosen to minimize the electrical pickup and to reduce the material. The modules are designed to operate at a temperature of -7°C, implying the need for coolant temperatures of about -25°C and associated thermal enclosures. An extremely light evaporative cooling system (coolant C_3F_8) is used [58].

The very intensive radiational environment in which the SCT modules will be operating has been a big challenge for meeting the specifications. The heavy irradiation has been taken into account in the design and choice of the material. Both detectors and electronics have been irradiated to the level expected for ten years of LHC operation and have been shown to function within specifications.

10.1.2 Silicon detectors: *Why*? and *How*?

The semiconductors

Semiconductor devices[2] are increasingly used in technology since the first junction device (transistor) was invented in 1947. Silicon, a very cheap material to find and elaborate, is the most commonly used material for creating semiconductors commercially.

The semiconductors are very similar to insulators. At room temperature there is no electrical conduction without the presence of an external field. However, the semiconductors have much smaller band-gap (difference in energy between the valence band and the conduction band), allowing movement of electric current through the material in the presence of an external field (Figure 10.2).

In the *intrinsic* semiconductors, where there are no impurities, the number of charge carriers is determined by the properties of the material and the electron density depends on the temperature. The electrical properties of semiconductors are modified by introducing impurities (*doping*). The *extrinsic* semiconductor can be either $n-type$ material, in which case a *donor* donates electrons in the conduction band, or $p-type$ material, in which case an *acceptor* accepts an electron to create

[1] Because of the endcap geometry some modules need to be shorter and therefore they consist of two rather than four sensors, still glued back to back.

[2] For this section, the Reference [55] was mainly used. Other sources of information include Reference [56].

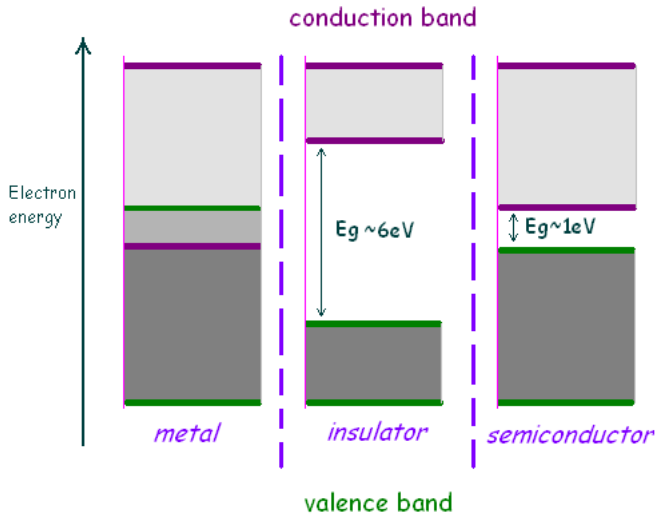

Figure 10.2: The different types of material, according to their electrical conductivity. Typical values of band gaps energies are given.

a covalent bond (resulting in a *hole* in the semiconductor's valence band). Silicon is doped with *Arsenic* (As) to get n-type silicon or with *Boron* (B) to get p-type silicon (Figure 10.3).

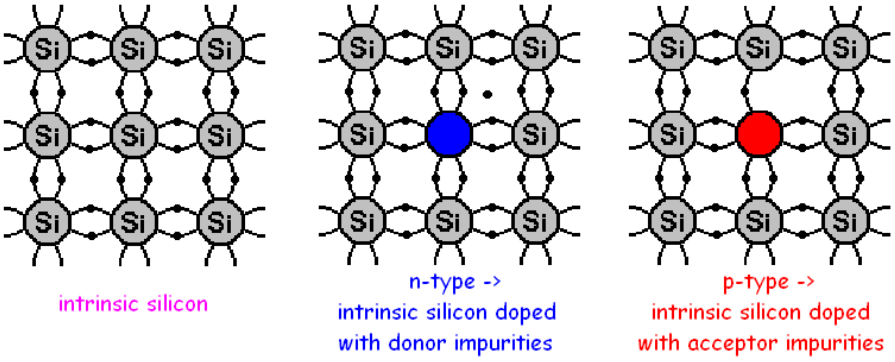

Figure 10.3: Intrinsic and extrinsic silicon.

Extrinsic semiconductor properties

One of the main characteristics of the carriers (electrons and holes) is the *mobility*, a measure of how strongly the motion of the electron or hole can be influenced by the applied field. Two phenomena are taking place inside the crystal; the

lattice scattering, thermal vibrations that result in energy transfer between the carriers and the lattice, depends mainly on the temperature, while the *impurity scattering*, charge carriers traveling past ionized impurities, depends on the impurity concentration. In heavily doped samples, where the impurity scattering dominates, the mobility increases with increasing temperature, while the opposite happens in lightly doped samples. The mobility and the carrier concentration inside a sample define the *resistivity* of the sample.

At thermal equilibrium, the carrier concentration follows the "mass action law": $n \cdot p = constant$. n or p carriers may dominate, but their product is constant, at a given temperature. This law is invalid in non-equilibrium; in state of non-equilibrium, carriers are injected by induced photons or thermal vibrations and recombination of the injected minority carriers takes place. This is a continuous process taking place until equilibrium is reached.

$p-n$ junction

All p-type and n-type materials are relatively conducting materials, however the junction between them is non-conducting, when there is no external field applied to it. Around the junction, holes will leave the p-side and electrons will leave the n-side, they will recombine and form negative space charge near the p-side and positive space charge near the n-side, that results in an electric field $\mathcal{E}$. This electric field will generate further carrier mobility, towards the opposite direction. At equilibrium, the diffusion of the carriers (initiated by the difference in the carrier concentration) counter-balances the drift due to the field $\mathcal{E}$, generating a space-charge region, called *depletion* region. Outside the depletion region, the material is neutral.

The depletion region can be increased or decreased by applying an external field to the $p-n$ junction. A *forward-biased* $p-n$ junction (the external, applied field and the built-in field $\mathcal{E}$ have opposite directions) decreases the depletion region. A *reverse-biased* $p-n$ junction increases the depletion region.

Junction devices as Particle Detectors

The properties of the silicon and the $p-n$ junction are exploited in making detectors. Silicon is characterized by a small band-gap (1.12 eV at room temperature) and the energy for creating an electron-hole pair inside the active volume of the detector is only 3.6 eV[3]. The density of silicon is high (2.33 gr/cm^3) and the energy loss

[3]Note that the ionization energy in gases is approximately 30 eV.

for minimum ionizing particles as high as 3.8 MeV/cm, therefore thin detectors can still produce large signals. The charge can be rapidly collected because of the high mobility, so the detectors can efficiently be used in high rate environments. Other characteristics, like their rigidity, that makes them self-supporting structures or their easy integration to the electronics, make silicon detectors a widely used type of detectors for collider physics.

The principle of operation of a silicon strip detector is shown in Figure 10.4. The types of impurities reported in this figure are specific to the ATLAS SCT detectors, that will be described below. Variations exist and depend on the specifications that the detector has to meet.

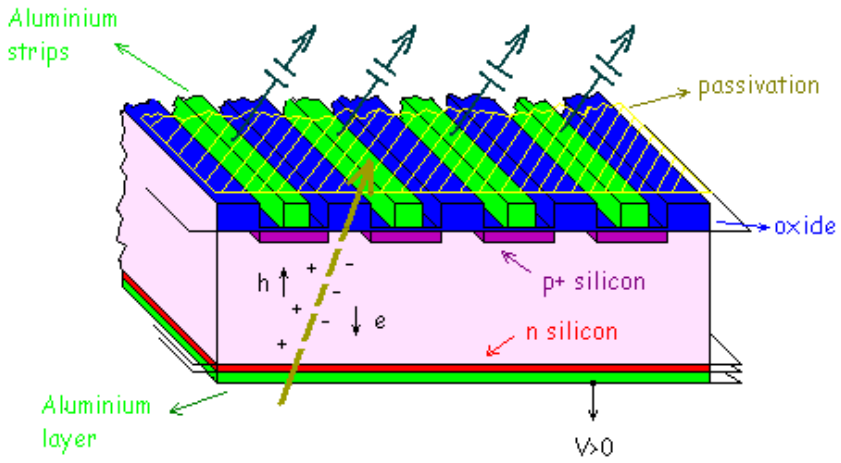

Figure 10.4: Schematics of a silicon microstrip detector. The thickness is typically ≈300 μm. The depletion capacitance usually ≈0.1 pF.

The detector consists of a bulk material doped with donors (n-type silicon). A heavily doped layer of n-type material provides the Ohmic contact to the aluminum electrode, on one side. p^+-type[4] implants are added on the other side, an oxidation layer (SiO_2) to ensure the device stability and metal (aluminum) strips. The device is biased in reverse mode, resulting in a large depletion region. The silicon detector is biased through poly-silicon resistors that connect the implants to a nominal bias voltage (Figure 10.5).

When a charged particle traverses the detector, electron-hole pairs are generated. The holes drift towards the p-implants and the aluminum strips, that are AC coupled to the read-out electronics. The AC coupling is implemented in the oxide layer

[4]Heavily doped p-type silicon

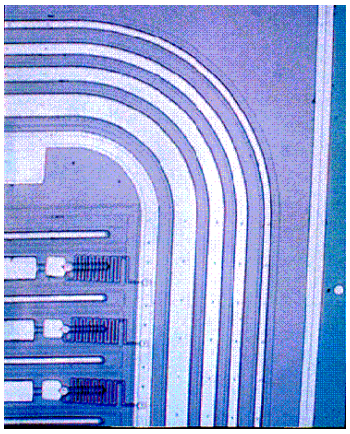

Figure 10.5: The snake-like forms of the poly-silicon resistor provide approximately 1 MΩ resistance.

between the strips and the p-implants. The charge associated with each strip gives spacial information. In a binary read-out, the precision of the measurement depends on the *pitch* (the distance between two strips). The binary readout has been chosen as a cost-effective solution that meets the requirements for resolution and speed. The resolution of the detector depends on the pitch p and is defined as

$$< \Delta\chi^2 >= \frac{1}{p}\int_{-p/2}^{p/2} \chi^2 d\chi = \frac{p^2}{12}$$

A detector with a pitch of 80 μm has a resolution $\sqrt{< \Delta\chi^2 >} \approx 23$ μm.

Radiation tolerance of the silicon sensors

The particles from the collisions in the center of ATLAS interact with the material of the silicon detector to create the detectable signals. The signal we detect comes from interaction of the particles with the electron cloud of silicon. However, the particles also interact with the nuclei in the lattice, generating permanent material changes, often of detrimental nature. The resulting *radiation damage* depends strongly on the type of the radiation. Electrons create isolated, point defects in the crystal, while protons interact with coulomb scattering and nuclear scattering creating both point and cluster defects.

The defect complexes (either point or cluster defects) act as recombination and generation centers in the depletion region, significantly increasing the reverse-bias current (dark current). They may also act as trapping centers, re-emiting particles

with some time delay and resulting in reduction of the signal. The charge density in the depletion region may also be affected, requiring increased bias voltage to make the detector fully sensitive.

The SCT silicon detectors have been tested in a radiation environment. They are expected to survive 10 years of LHC data taking. The unavoidable property changes are expected to need bias voltage adjustments in order for the detector to be fully operational. The operating voltages will be between 250 and 450 V, depending on the sensor position on the barrels or endcaps (the distance and direction from the interaction point), while the detectors will initially operate at 150 V [57].

10.1.3 SCT Silicon Modules

A total of 15912 silicon sensors are employed by the SCT detector. The thickness of the sensors is 285 μm, a compromise between the required signal collection and the simplicity of fabrication. The strip pitch was determined by the required digitizing precision, granularity, particle occupancy and noise performance. A pitch of 80 μm with two $\approx$6 cm long daisy-chained sensors was chosen for the rectangular barrel sensors. Radial strips with mean pitch of $\approx$80 μm were chosen for the trapezoidal end-cap sensors. Each sensor consists of 768 active strips of $\approx$12 cm of total length, plus two strips at the bias potential to define the sensor edge.

The sensors are the principle building blocks of the SCT modules. Each silicon module, belonging to the barrel or the endcap, has similar structure; it consists of silicon sensors glued in pairs back to back on a support structure that also ensures that the thermal and electrical conductivity requirements are met. The *Front End (FE)* electronics are directly placed on the module, in the form of an electrical circuit mounted on a kapton support (*hybrid*). In all modules, the azimuthal angle ϕ (essential for momentum measurement) is measured with high precision. The barrel modules provide a measurement in the z coordinate and the end-cap modules provide a measurement in the radial distance R. A third measurement is provided by the sensor position. The nominal resolution of the silicon modules is 17 μm in $r-\phi$ and 580 μm in z or r.

There are four different types of modules: the *barrel modules*, and three types of *end-cap modules*. The barrel modules are rectangular, made of 4 sensors that are glued back to back in two pairs, with the hybrid glued between the pairs, in the middle of the module (Figure 10.6). The end-cap modules have different geometries that are determined by the place of the module in the end-cap disks. Each disk,

1.2 m in diameter, employs 132 modules arranged in 3 rings; the *outer* ring (52 modules), the *middle* ring and the *inner* ring (40 modules each). The modules on the disks overlap to minimize gaps. The outer and middle ring modules consist of 4 sensors glued back to back in pairs, while the inner ring modules are smaller, with only one pair of sensors glued back to back (Figure 10.7). The hybrid is glued in the edge of the module as shown in the figure. The exact dimensions of the silicon sensors that are used for the various types of modules are listed in Table 10.1.

Module type	Sensor Length (mm)	Active module length (mm)	Strip pitch (μm)
Barrel	63.960	126.09	80.0
End-cap Inner	61.060	59.1	56.9-69.2
End-cap Middle	65.085 54.435	115.61	69.9-83.0 83.4-94.2
End-cap Outer	65.540 57.515	119.14	70.9-81.1 81.5-90.4

Table 10.1: Exact dimensions of the SCT barrel and end-cap sensors. The tolerance in all sensor lengths is ± 25 μm. The pitch accuracy is at the level of ± 1 μm.

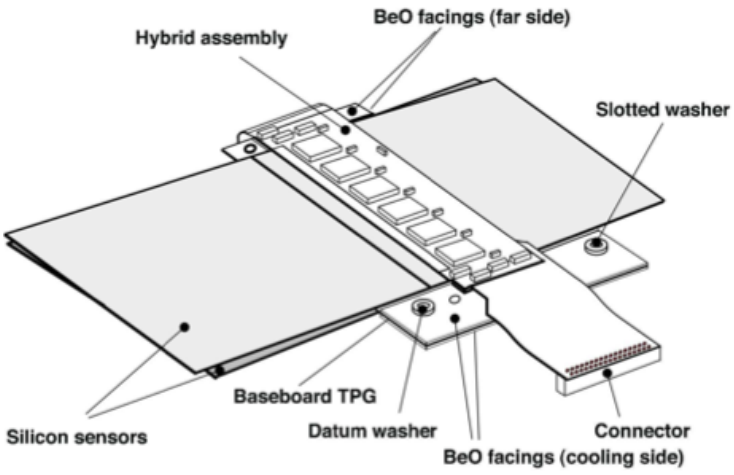

Figure 10.6: Barrel module layout

Each of the electronics hybrids consists of 12 *Application Specific Integrate Circuits (ASICs)* that are built in radiation hard technology and called ABCD3T [59]. A diagram of the FE electronics sequence is shown in Figure 10.8. It consists of an analog and a digital part.

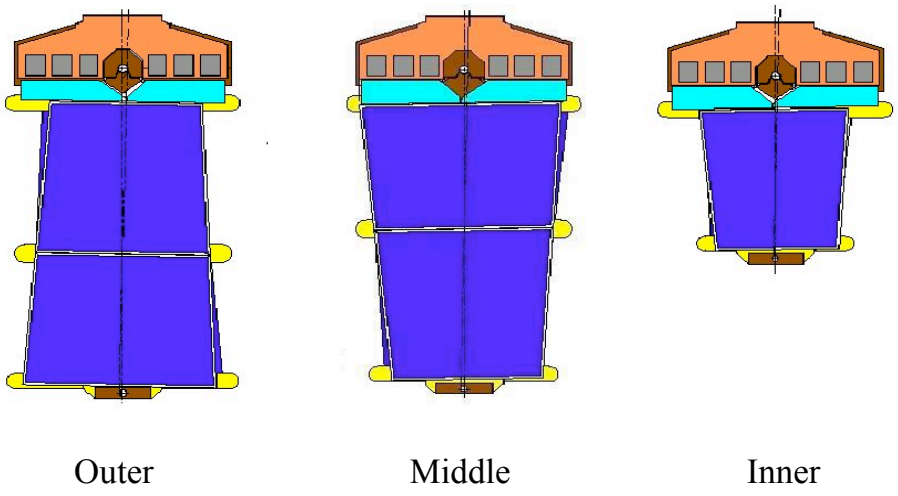

Figure 10.7: Forward module layout.

For each of the 128 input channels of each chip, an amplifier-shaper-discriminator sequence is replicated. The discriminator gives in the output binary information. The channel gives a logical zero or one, according to below or above a threshold charge collection, respectively. The digital information is fed into a FIFO pipeline, 132 cell long. The pipeline provides the required latency by the Level 1 trigger decision time. The chip implements the zero suppression and the encoding of the event to be read out at the Level 1 accept signal. The electrical signal coming from the readout chips are converted to optical pulses with specific ships called 'opto-links'. The first ASIC on each side of the module is connected to the optical link; at Level 1 accept signal the other five send their data to the master and the master passes the data to the optical link. In case of failure of one ASIC, there is the possibility of bypassing it without interrupting the readout chain. If one of the two master chips fail, the other one is used for reading out the whole module.

10.2 End-cap module production

The production of the barrel and end-cap modules took place in various sites around the world. It has been a collaborative effort that was completed in late 2005. Fully assembled barrel and end-cap modules can be seen in Figure 10.9.

A large fraction of the end-cap modules (655 *outer* modules out of the total 1976 end-cap modules) has been assembled and tested at the University of Geneva

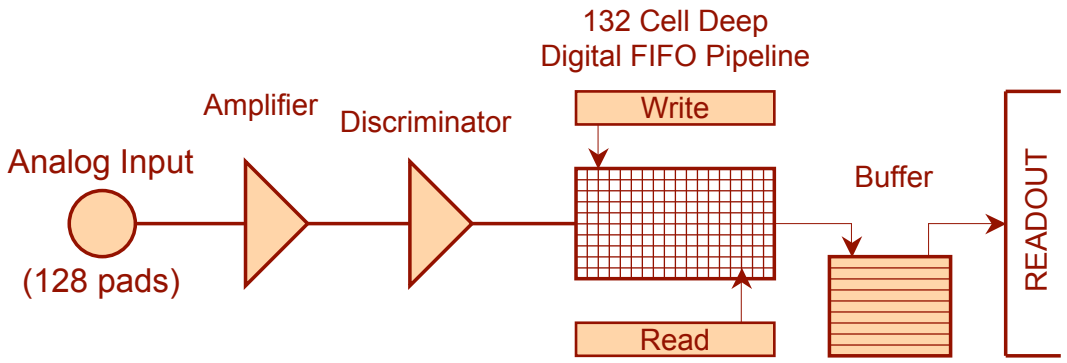

Figure 10.8: Diagram of the SCT FE electronics (ABCD3T chip).

assembly facility. The quality assurance was completed at CERN and the modules were shipped to NIKHEF and the University of Liverpool for assembly onto the endcap disks. All disks have been completed (Figure 10.10) and mounted in the endcaps. The end-cap assembly is fully completed.

The build tolerance of the end-cap modules was very strict for the design accuracy to be achieved. The end-cap module mechanical specifications are listed in Table 10.2.

Parameter		Tolerance	Accuracy
Position back-to-back in plane	lateral	< 5 μm	± 1.6 μm
	longitudinal	< 10 μm	± 1.3 μm
Envelope (Thickness)		< 115 μm	± 15 μm
Module fixation points wr to center		< 20 μm	± 6 μm

Table 10.2: End-cap module mechanical build specifications.

A summary of the production and testing at the Geneva facility will be given here. More information can be found at [60] and [61].

10.2.1 Module Components

A sketch of an endcap module components is shown in Figure 10.11. Three are the main parts of the silicon modules:

1. *The silicon sensors*; the outer modules use four *Hamamatsu* sensors glued back to back in pairs.

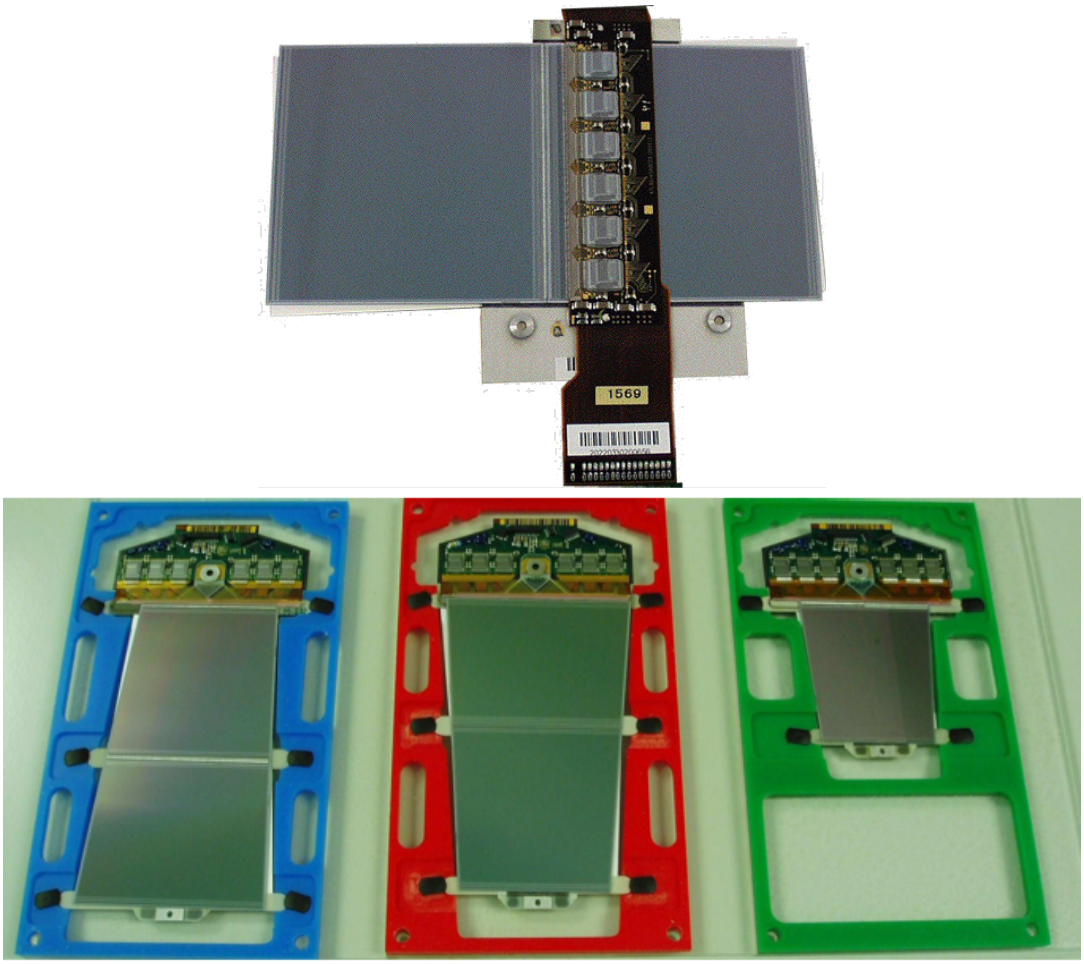

Figure 10.9: Barrel and end-cap modules fully assembled. The active length of the barrel and the outer and middle end-cap modules is ≈12 cm. The active length of the inner end-cap module is ≈6 cm.

2. *The spine*; it is the support structure for the sensors, but also ensures thermal conductivity.

3. *The electronics hybrid*; it includes the whole FE electronics chain (Level 1 trigger) of module.

Other mechanical parts of the modules include:

1. *The pad locator*; it is a precision locator that provides mounting precision when mounted on the disk.

2. *The far-end locator*; provides precision in the y direction.

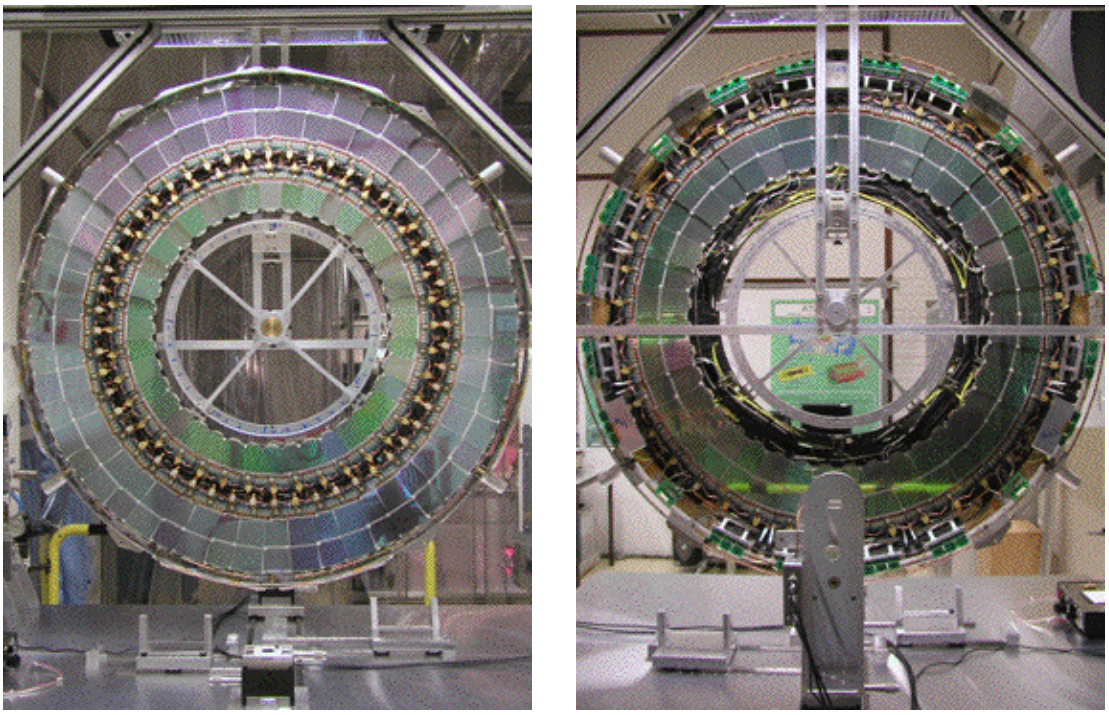

Figure 10.10: A fully assembled disk. The three rings with the modules mounted on it are shown in the pictures; the outer and inner modules on the front side (left picture) and the middle modules on the back side (right picture). Each of the disks is ≈1.2 m in diameter.

3. *The fanin*; it is a glass plate with metal tracks that provides metal conductivity between the silicon sensor pads and the pads of the readout chips. It also provides a mechanical connection between the hybrid and the sensors.

10.2.2 Module Production Overview

Single component testing

All the components of the modules were tested prior to assembly.

- The good electric behavior of the sensors was verified performing an I-V test. An exponential-like behavior in the I-V curve, or current above a certain threshold, indicated problematic sensors; problems occured mainly by broken sensor edges, scratches and surface contamination. The surface contamination could be corrected by cleaning the surface of the sensor (e.g. fluxing dry air). Sensors with unrepairable problems were not used in module production.

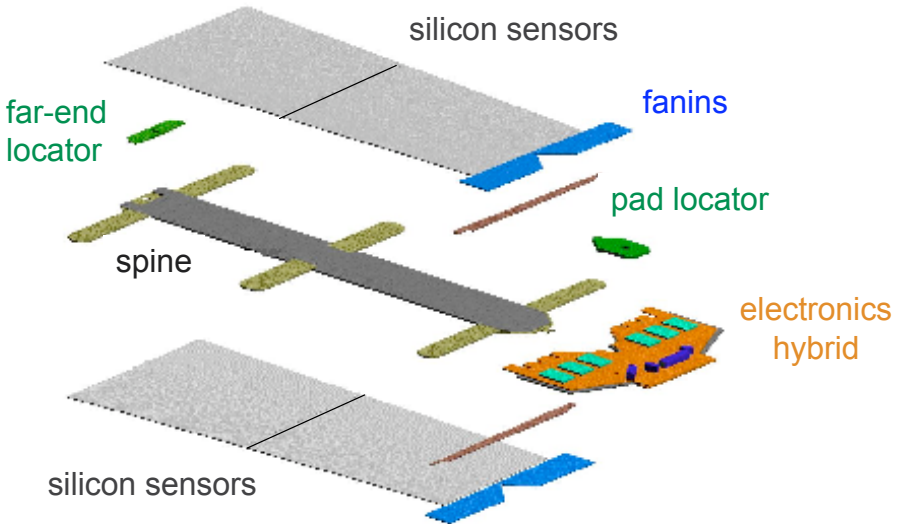

Figure 10.11: The SCT endcap module components.

- The electronics hybrids were visually inspected with a microscope to verify that the ASICs chips were properly bonded, and that there was no visual damage on their surface.

- The spine and fanins were visually inspected.

- The pad locators were visually inspected. Their quality and metrology was also checked.

Detector gluing on the spine

The sensors were glued back to back on the spine using an alignment device and a handling frame. Once the four sensors were glued on the spine, an I-V test was performed for each of the sensors, to verify their good electrical performance.

Hybrid gluing

Reference pins and a special handling frame were used for the hybrid alignment to the sensor-spine assembly. The fanin pieces were also aligned and transfered in the jig, where the gluing took place. The module was left overnight for glue curing. An I-V measurement for each sensor was made to verify that the last assembly step didn't affect it.

Wire Bonding

Wire bonding was performed in both sides of the module. The sensors were bonded to each other, and to the hybrid. This was a very delicate procedure therefore very precise machines were needed, but also very well trained people to operate them.

After the bonding took place, the total current of the module was measured in an I-V test (Figure 10.12).

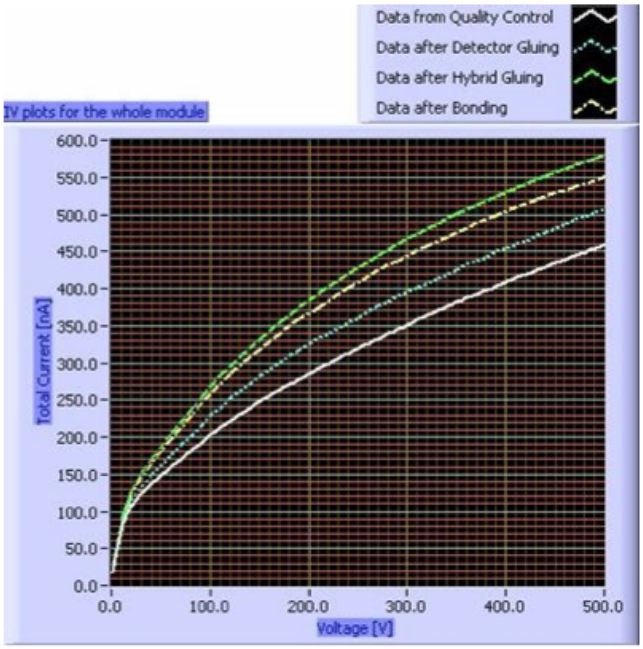

Figure 10.12: I-V curves of a typical module. The current of all four sensors is summed up to be compared with the final curve (after bonding) where all sensors are electrically connected.

The module was also undergoing a metrology test. The $x-y$ and the z profiles were measured. For the $x-y$ profile, several reference points and the distance between them were measured and had to be within particular specifications. For the z profile, 50 different points on each side of the module (Figure 10.13) were measured relative to a reference plane $z = 0$. All points had to be within the specifications (none should exceed a ± 115 μm envelope).

After assembly

Once the assembly was completed, the module was subjected to thermal cycling, to verify that operation over a range of temperatures did not change the mechanical

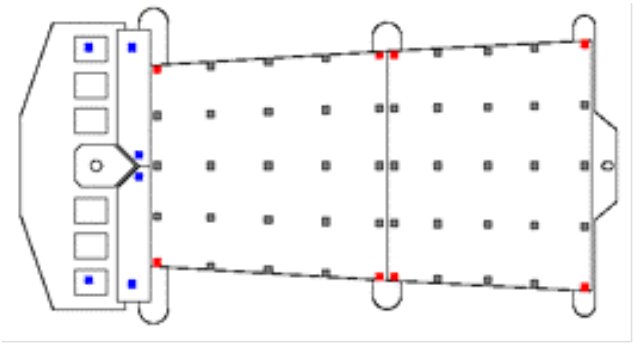

Figure 10.13: 50 points measured for the z profile. The measurements are done for both sides of the module.

precision of the module or the electrical functionality. After completion of a thermal cycling, a final metrology survey was taking place, and the profiles before and after the thermal cycling were compared.

The electrical and readout specifications of each module were also verified. A dedicated series of quality assurance tests was performed, and these were described in the following section. A module ready for electrical testing in a dedicated box is pictured in Figure 10.14

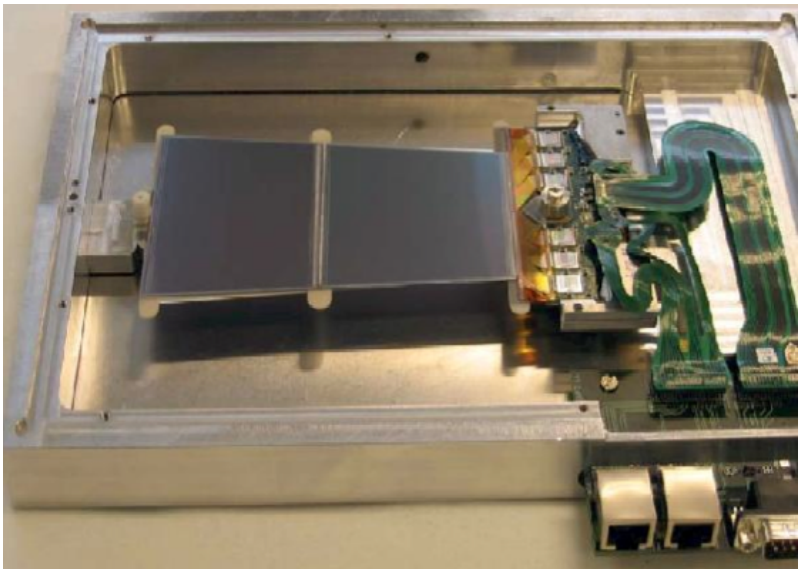

Figure 10.14: A module fully assembled inside a dedicated box for electrical testing.

10.2.3 Module Quality Assurance (QA)

Hardware

Custom VME cards were used for the readout of the modules. Even if the final readout of the modules is optical, these early measurements were performed using electrical links, that were bypassing the optical ones. The optical readout was tested electrically. The modules that were used in the readout chain are:

- The *CLOck And Control (CLOAC)*; the master module, that generates fast commands such as the L1 trigger.
- The *SLOw command Generator (SLOG)*; it distributes the clock and fast signals from the CLOC to up to 12 modules.
- The *ATLAS End-cap Read-Out (AERO)*; it provides the electrical interface for up to 6 End-Cap modules. The data communication is done through the optical data receiver and transmitters, place on the hybrid.
- The *Multichannel Semiconductor Tracker ABCD Readout Device (MuSTARD)*; it receives data from up to 6 modules, decodes the event and creates histograms.
- The *SCTLV* module; provides low voltage for up to two modules and reads out the NTC thermistor mounted on the hybrid.
- The *SCTHV* module; provides the high voltage (detector bias) for up to four modules.

The VME crate was interfaced to a PC running a data acquisition package, called *SCTDAQ*.

The modules were tested within a dedicated aluminum test box. It has mechanical supports for holding the module steady. The electrical connections were made via custom kapton tapes (pictured in Figure 10.11). The cooling of the modules during operation, was achieved using a chiller that circulates a mixture of cooled ethanol and distilled water through the test boxes. Nitrogen flow through the boxes ensured that the dew point remains at a safe level of $< 40\%$.

Module electrical specifications and functional tests

A set of tests was made to verify:

- The operation of the module up to 500V bias voltage;
- Signal linearity better than 5%;
- Signal peaking time < 20 ns;
- Channel gain 50 mV/fC;
- *Equivalent Noise Charge (ENC)* noise < 1900 *electrons*[5];
- Noise occupancy $< 5 \times 10^{-4}$ for a discriminator threshold of 1 fC;
- Time walk ≤ 16 ns and bunch crossing resolution better than 99%.

In order to verify these specifications and identify defects or failures, a sequence of tests was performed. The tests were automated with SCTDAQ and they were categorized in *digital* and *analog*.

The purpose of the digital tests was to verify the good function of the chips. They were:

- *Stream Delay*: it adjusted the relative phase between each input data stream and the system clock.
- *Hard Reset*: it verified that the Clock, Command and Hard Reset signals were received correctly to the chips. It identified severe failures or bad connections.
- *Redundancy test*: it identified modules with faulty command reception or addressing errors.
- *Full Bypass test*: it exercised the data passing links between the chips on the hybrid. Links that did no work were recorded as defects. They could be identified as being due to a missing wirebond and in such case repairable.
- *Pipeline test*: pipeline defects were identified. The pipeline was checked with all channels enabled for dead cells and dead channels, and with all channels disabled for stuck cells or stuck channels. Modules that had a large number of dead or stuck cells or channels were rejected.

[5]The ENC noise is an expression of the noise in terms of electrons. The ENC is the standard deviation of the assumed gaussian noise distribution in units of electron charge. The noise occupancy is required to be below $5{\times}10^{-4}$. Setting the 3.3σ threshold to the expected operating value of 1 fC implies an ENC of 0.3 fC or 1900 electrons.

The analog tests were used to characterize the response of the front-end chips to an injected charge. The first analog test needed to be performed was the *Strobe Delay* test, that checked the response of the electronics to the charge injection pulse. The *three-point gain* was the main analog test performed at the Geneva facilities. Threshold scans were taken for three injected charges to allow a quick measurement of gain, noise and the discriminator offset. Pathological channels were characterized as *faulty* if its detection efficiency was low but not zero, and *lost* if the defect resulted in a zero efficiency. The maximum number of defective channels should not exceed 1% per module. Modules with problems were potentially repairable.

Further tests (analog mainly) were performed in the CERN facility, where the modules are transfered to the extended and final testing.

Module production quality

During assembly, the modules were classified into 5 categories:

- *Good*: all electrical and mechanical specifications are satisfied;
- *Pass*: Fail one of the metrology tests by no more than 50%;
- *Fail*: Fail one or more electrical and/or mechanical specifications without possibility of rework;
- *Abort at Phase 1*: Assembly was aborted before the hybrid was glued because of problems during spine gluing;
- *Hold*: During production, problematic modules that could be reworked were classified in this category. After rework, the modules were classified in one of the first three categories.

The overall results of the module production are summarized in the diagram of Figure 10.15. Out of the 634 *good* and *pass* modules assembled and tested in Geneva, 4 modules subsequently failed at CERN during the full electrical characterization or for visual defects such as ceramic cracks or the existence of glue on the hybrid capacitors.

The *good* and *pass* modules had an average ENC module noise of 1620±74 electrons (with the specifications giving a maximum ENC noise at 1900 electrons) and an average noise occupancy of $(4.7\pm3.0)\times10^{-5}$ (according to the specifications this value should be less than 5×10^{-4}). The mean leakage current at 150 V bias

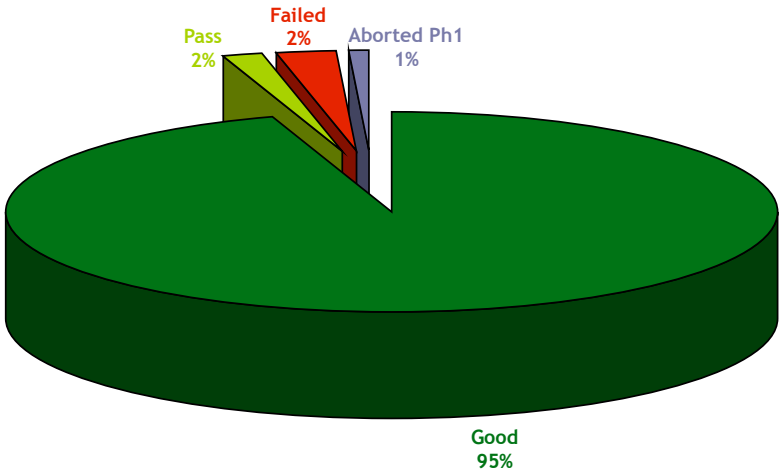

Figure 10.15: Overall statistics of the module production at the University of Geneva.

is estimated to be 360±70 nA and at 350 V bias, 500±70 nA (according to the specifications the leakage current limit is set higher than 1 μA). The quality of the modules that were delivered for assembly was well within both the electrical and the mechanical specifications.

Typical module failures included operator errors, tooling errors of component defects. Understanding the errors and learning from them at the beginning of the module production was of prime importance for the good quality modules delivered by the University of Geneva to the SCT collaboration and ATLAS.

10.3 Summary

In this chapter, the ATLAS SemiConductor Tracker (SCT) is described and the silicon module production at the University of Geneva is presented. The production lasted for about two years. About 1/3 of the total number of end-cap modules have been produced at the University of Geneva facility. 97% of the produced modules have been within the specification and delivered to the SCT collaboration. Following assembly, the modules were transported to the CERN testing facility for extended testing and then to the assembly sites, Liverpool and NIKHEF, for assembly in the endcap disks.

Chapter 11

The Detector Control System for the SCT Assembly Phase

Each of the 4088 SCT modules (60 m^2 silicon surface) requires several power lines for the electronics hybrid and silicon sensors, plus 3 fibers for the optical readout. Each of the electrical lines is individually controlled and monitored. The reliable operation of the cooling system is mandatory for the stable detector operation. A total number of almost one thousand sensors, placed at various points through the SCT, provide information on the humidity, temperature and pressure. The coherent and safe operation of the SCT during commissioning and subsequent operation is an essential task of the Detector Control System (DCS). The main building blocks of the SCT DCS, the cooling system, the power supplies and the environmental system, are described in this chapter. The DCS was initially tested during the SCT assembly phase. Results from the initial testing are therefore also presented.

11.1 The ATLAS DCS

11.1.1 Scope of the ATLAS DCS

The large number of parameters to be monitored and controlled demands a robust and secure Detector Control System (DCS) to ensure electrical operation of the modules as well as reliability under the extreme environmental conditions. The ATLAS DCS supervises the full slow control of the experiment and provides hardware and software tools for monitoring, interlocks and controls. It provides communication between all the subdetectors and interaction between ATLAS and the LHC accelerator, as well as other external services such as cooling, ventilation and safety systems. The overall control of ATLAS includes the monitoring and control of the

detector hardware and the related infrastructure, as well as the supervision of the software involved in the event readout, this latter task being provided by the Data Acquisition (DAQ) system. The two systems (DCS and DAQ) are independent but their interaction is essential; the DCS is a vital component for the reliable and safe operation of the detector, and for the data taking ([62], [63]).

11.1.2 The LHC and ATLAS DCS Organization

All ATLAS detectors use a common DCS architecture and share the same utilities to develop their DCS systems. A Joint Controls Project (JCOP) [64] at CERN addresses common points of control. It is within this framework that the SCT DCS has been developed. The DCS consists of a distributed Back-End (BE) system running on PCs and Front-End (FE) systems ranging from simple elements like temperature sensors to complex controllers. For the LHC needs, the BE is implemented with PVSS II [65], a commercial Supervisory Control and Data Acquisition system (SCADA). It is a powerful and flexible package that provides easy communication between the PC and the hardware, allowing the developer to create a Graphical User Interface for the monitoring and control of the latter. The building blocks of each PVSS project are datapoints, each of which corresponds to a hardware unit or to a monitored parameter. Datapoints are the upper level of a tree structure and can be built into functional objects. This type of structure makes the project development flexible, comprehensive and maintainable. The organization of the DCS is hierarchical and simulates the hardware structure of the experiment. DCS consists of independent partitions that can be operated in standalone or integrated mode. The Finite State Machine (FSM), a tool written in SMI++ and developed under the JCOP framework, handles the states and transitions of the different partitions, by means of commands and messages [66]. The essential FE component used for the ATLAS DCS is the ELMB (Embedded Local Monitor Board), developed for standard analog and digital I/O (Figure 11.1). It is radiation hard, has low power consumption and can either be embedded into a custom motherboard or used in standalone mode [67]. The ELMB communicates with the BE system via the CAN (Controller Area Network) field bus [68], using a high level protocol, CANopen. The CAN interface [69] card that has been chosen (Kvaser card), gives the possibility to have 4 different CAN buses connected and readout simultaneously by one PC-slot. An OPC (Object linking and embedding for Process Control) server [70], developed at CERN, provides the configuration software to allow easy monitoring of the

ELMB.

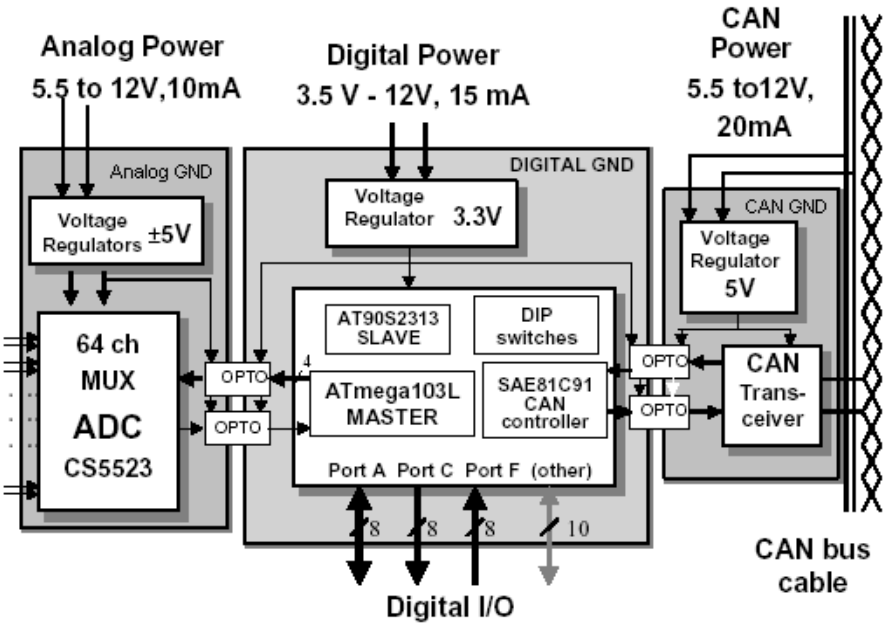

Figure 11.1: Simplified diagram of the ELMB. It has digital and analogue channels for input and output. The main purpose of the ELMB is the conversion of the analogue information from the connected sensors into digital information that is provided to the DCS via CANbus.

11.2 SCT DCS Hardware Description

The SCT hardware is naturally divided in groups depending on its function, namely the cooling system, the environmental system and the power supplies [71].

11.2.1 The Cooling System

The radiation-induced leakage current and doping change affecting the depletion voltage of the silicon modules depends on the operating temperature of the SCT modules. The operating temperature of the SCT varies from +15°C, during startup and commissioning, to -7°C, during operation in the ATLAS pit. Thermal stability of better than 2°C and a tolerance to thermal shocks are two issues that have to be ensured for all the operations [72].

An evaporative fluorcarbon cooling system has been chosen for both the SCT and

the pixel detector. The coolant is C_3F_8, a non-flammable, non-conductive and radiation resistant liquid. The temperature can be tuned by a change in the operating pressure.

The control of the cooling processes (starting up, operation and shutting down) and the monitoring of the main cooling parameters (pressure and concentration of the cooling fluid) are performed by a Programmable Logical Controller (PLC). DCS has monitoring functions.

11.2.2 The Power Supplies (PS)

The silicon modules mounted on the SCT detector are powered by the High Voltage (HV) and Low Voltage (LV) power supplies. Each LV card [73] controls 4 electrically independent LV channels. It outputs logical signals for the FE electronics of the modules (RESET and clock SELECT) and 4 different voltages: the analog (Vcc) and digital (Vdd) voltages for the readout chips as well as VCSEL and PIN bias voltages for the optical communication of the module. Two thermistors mounted on each barrel module and one thermistor mounted on each endcap module are read out through the LV cards. Each HV card controls 8 electrically independent HV channels, providing bias voltage to the detector modules (Figure 11.2) [74]. Typical values for the most important parameters supplied via the LV and HV cards are shown in Table 11.1.

Parameter	Voltage (Volts)		Current	
HV	150	max 500	300nA	max 5mA
Analogue LV	3.5	max 10	900mA	max 1300mA
Digital LV	4	max 10	570mA	max 1300mA
VCSEL	1.6 - 6.6	max 9.6	4mA	max 10mA
PIN	5 - 10	max 13	0.5mA	max 2.5mA

Table 11.1: Typical values for PS parameters.

The control and monitoring of the LV and HV cards relies on the Crate Controller (CC), the ELMB based interface between the PS modules and the higher levels of the DCS system. The ELMB used in the CC is custom programmed.

Four Power Packs (PP) are placed in each rack providing redundant powering to four PS crates.

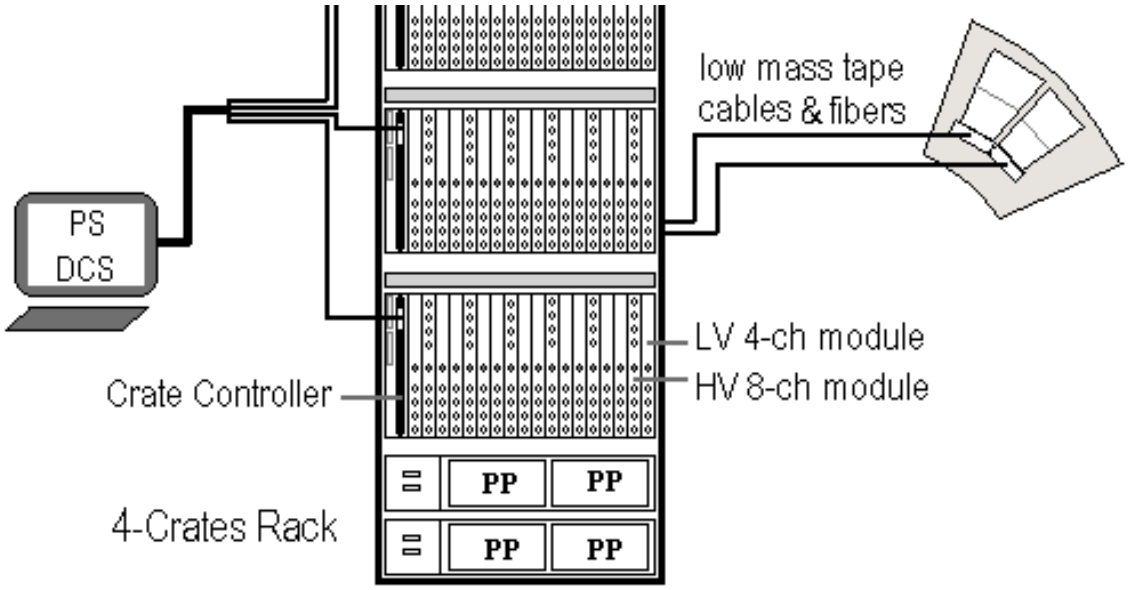

Figure 11.2: Layout of one power supply rack. Two of the four crates in a rack can be seen in the drawing.

11.2.3 The SCT Environmental System

The detector environmental system deals with the monitoring of the environmental sensors placed on the barrels and endcaps of the SCT. These are temperature and humidity sensors located at appropriate positions to provide information about the following parameters:

- the temperature close to the outlets of the cooling pipes (Figure 11.3);
- the temperature near the edge of the barrels, to give information about possible deformations in the shape of the support structures;
- the air temperature inside the detector; and
- the humidity inside the detector.

Temperature sensors

Resistance Temperature Detector (RTD) sensors, and more precisely NTC (Negative Temperature Co-efficient) thermistors, are used for the temperature monitoring. A schematic layout of the thermistors is illustrated in Figure 11.4. In this Figure, the adapters used in the ELMB, developed for the NTC sensors, are also illustrated. The

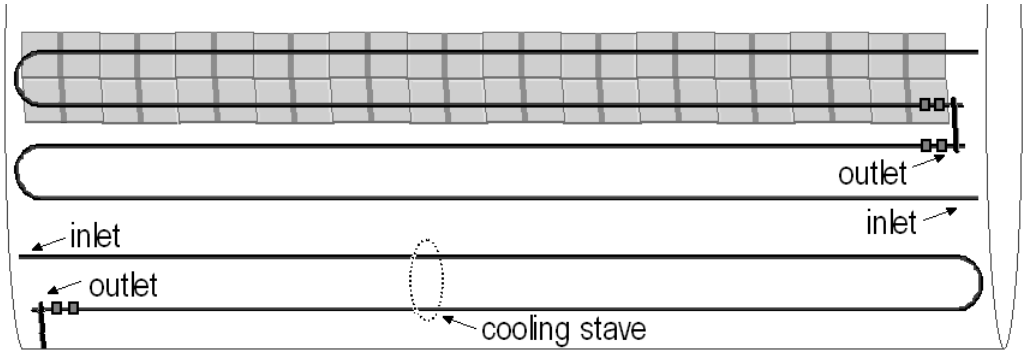

Figure 11.3: Schematic diagram of a cooling loop. The inlet and outlet of each cooling stave (half cooling loop) are shown. On each cooling stave, 24 modules are mounted. For redundancy, two temperature sensors are placed near each cooling outlet.

reference voltage, V_{ref} , is generated with the help of a stable precision operational amplifier from the same reference voltage as is used by the ADC. The calculation for the resistance of the sensor is given by the formula:

$$R(T) = \frac{V_{Ch} \times R_a}{2.5 - V_{Ch}}$$

where V_{Ch} the voltage measured by the channel and R_a the value of the resistor on the adapter.

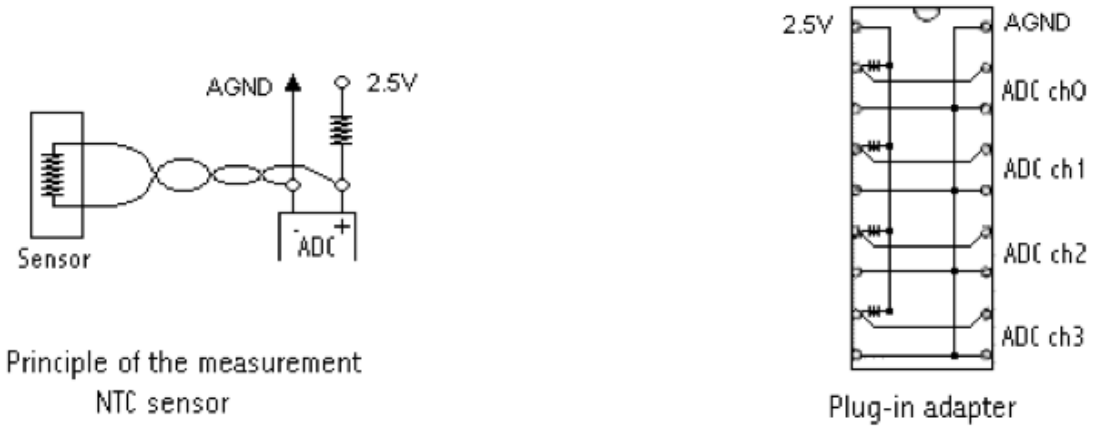

Figure 11.4: Temperature sensor - NTC.

The temperature can be extracted by the formula:

$$T = \frac{1}{A + B\ln(R(T)) + C[\ln(R(T))]^3}$$

where A, B and C coefficients given by the manufacturer of the sensor.

For each of these sensors, 1 ELMB channel is used since only two wires (and therefore 1 channel) are needed for them to function.

Humidity Sensors

The radiation-hard Xeritron sensors are used for the humidity monitoring [75]. A schematic layout of the sensor is given in Figure 11.5. For each sensor, there are 6 wires in 3 twisted pairs (and therefore 3 channels are needed in the ELMB). 1 of them is used to power the sensor. The rest give the readout voltages. The relative humidity is given by the formula:

$$RH = A \times \frac{V_1}{V_1 + V_2} + B$$

where V_1 and V_2 the voltages as shown in the figure.

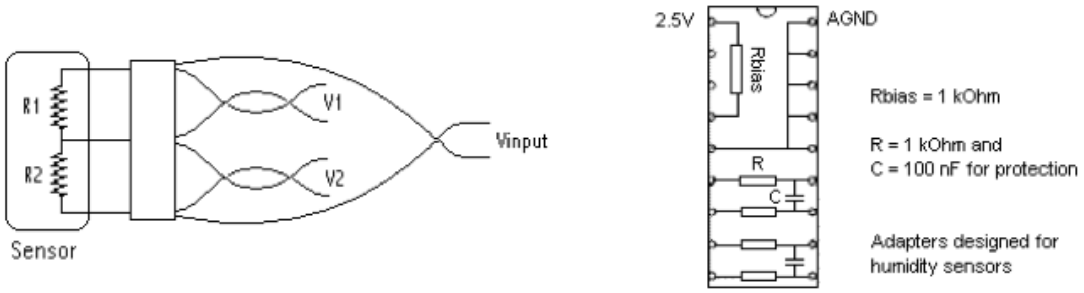

Figure 11.5: Humidity Sensor.

Thermal enclosure

To separate the cold SCT volume from the transition radiation straws detector operating at room temperature, the SCT will be surrounded by a thermal enclosure and maintained in a dry, cold nitrogen atmosphere. For the assembly phase, a temporary thermal enclosure dedicated to single barrel acceptance tests has been built, allowing the barrel to be placed in a dry environment and under controlled

environmental con- ditions. Humidity, differential pressure and temperature sensors are installed. A flow meter measures the dry air flow into the enclosure.

Interlocks

All the environmental sensors are connected to ELMBs and monitored by software. For the temperature sensors on the cooling pipes, there is an additional hardware interlock. The ELMBs used for the monitoring of these sensors are not embedded in the standard motherboard but in motherboard cards mounted in the Building Block Interlock Monitoring (BBIM) crates, where the Interlock Boxes (IBOXes) are also mounted [76]. Each sensor is connected in parallel to the ELMB and the IBOX. The IBOX, designed within the ATLAS pixel collaboration, is a board that allows setting a threshold to the input voltage and acts as a discriminator resulting two logic states at the output of the IBOX. Therefore, if the cooling temperature exceeds a predefined value, the output of the IBOX triggers the Interlock Matrix (IMatrix) [77]. The IMatrix provides the hardware mapping between the temperature sensors in a cooling stave and the corresponding to the modules mounted in this stave, PS cards. The mapping is im- plemented in a Complex Programmable Logic Device (IspMACH5000VG, LC5768VG from Lattice Semiconductor), programmed with VHDL to switch off the affected power supplies in case of high temperature trigger. A System Interlock Card (SIC), mounted in each crate, distributes the signals from the interlocks to the LV and HV cards via the backplane. A diagram of the monitoring and interlock chain of the temperature sensors on the cooling pipes is shown in Figure 11.6.

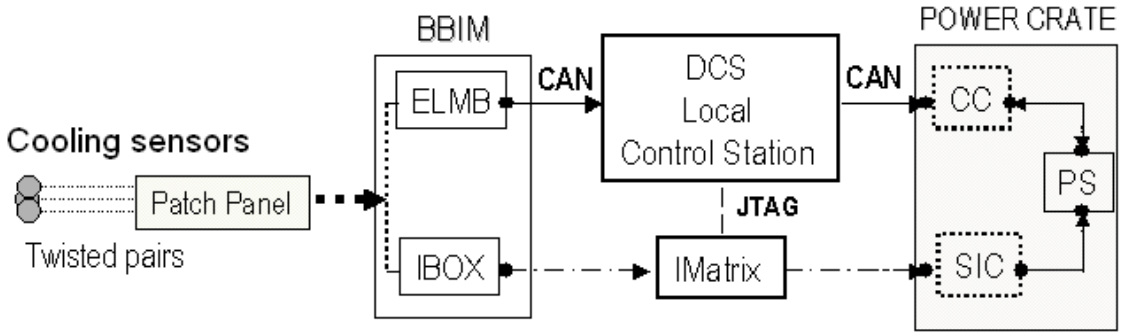

Figure 11.6: Environmental Cooling DCS overview. Each cooling sensor is software (ELMB) and hardware (IBOX) interlocked.

11.2.4 SCT DCS Software Description

All the hardware connected to the SCT detector is under DCS supervision. The different groups of this hardware define the DCS software building blocks. Three main projects have been developed: the Cooling, the Environmental and the Power Supply Projects.

DCS BE Structure

The SCT DCS BE system is a part of the ATLAS distributed BE system. The structure is hierarchical, with the Atlas Global Control Station (GCS) at its head, controlling the whole experiment. The Subdetector Control Stations (SCS) coordinate the subdetectors. The base of the hierarchy consists of the subsystems for each subdetector, called Local Control Stations (LCS). The SCT LCSs are the environmental system and the power supply system. The cooling system is common to both SCT and Pixels and belongs to the Inner Detector SCS. The LCSs are the part of the system that the user can interact with, sending commands and viewing its status at the lowest possible level.

The SCT DCS Projects

Physically, the LCSs correspond to the PCs where the monitoring and control projects are installed. The projects are distributed, giving the possibility of exchanging datapoints, and therefore information. The large number of parameters to be monitored or controlled demands the use of databases presently in text file format where all the information about the systems is stored and from which changes are loaded. PVSS archiving tools are used for storing the running conditions. In the future, the ATLAS conditions database, based on Oracle [78], will be used for that purpose.

Cooling DCS

Monitoring of the operations of the cooling circuit is provided. Warnings and alarms are communicated to the PS project. This DCS project is common for Pixels and SCT and provides only monitoring.

Power Supply DCS

Through the crate controller, about 1500 parameters are read out for each crate, and all these parameters have to be monitored and controlled by the PS DCS project.

The GUI developed for that project can be used for actions on the crates (i.e. SWITCH ON/OFF) and for monitoring of the LV and HV parameters of the SCT modules, such as input voltage, current and hybrid temperature. Warnings and alarms are implemented. If a warning or alarm occurs in any of the other DCS subsystems, safety actions are taken by the PS, such as ramping down the voltage of the modules. Some more functionality (module current readouts, masking on or off crate modules) has been added where needed. The Power Supplies can be in 3 basic states: On, Off and Standby. The database of the project is very large and gives information about the safe, warning and alarm ranges of each state and parameter. The PS DCS and the DAQ share the database. The communication between the two systems (DAQ and DCS) is achieved by the DDC (DAQ and DCS Communication) project. It provides bi-directional exchange of data between the two systems, such as states and parameters, transmission of DCS alarms to the DAQ and the ability for the DAQ to issue commands to the DCS [79].

Environmental DCS

The environmental DCS project handles all the environmental sensors in the detector itself and in the thermal enclosure. In order to avoid condensation during the cooling process, the dew point temperature is calculated using the air temperature and the humidity values with the formulas described below:

$$dew\ point = \frac{-\ln\frac{P_d}{C_1} \times C_3}{\ln\frac{P_d}{C_1} - C_2}$$

where

$$\begin{array}{ll} p_d = p_s \times \phi & p_d = \text{partial water pressure (mbar)} \\ p_s = C_1 \times exp\frac{C_2 T}{C_3 + T} & p_s = \text{saturated water pressure (mbar)} \\ \phi = \frac{H}{100} & H = \text{relative humidity in \%} \end{array}$$

Alarms are created and propagated to the PS project if the monitored parameters are outside the safe range. The detector environmental project uses a configuration file that provides the mapping of the physical position of the sensors on the detector to the ELMB channels. The mapping of the cooling sensors is also used by the Cooling DCS project. A summary of the DCS BE structure with all the DCS software components is presented in Figure 11.7.

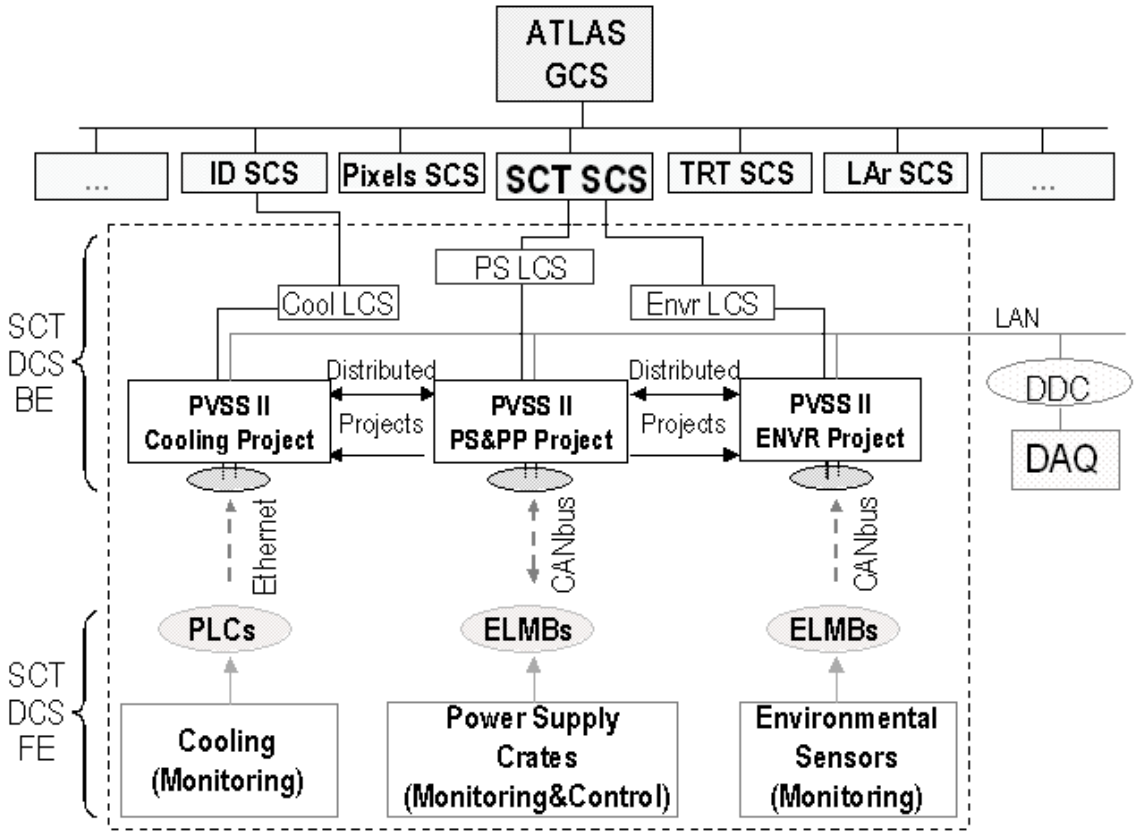

Figure 11.7: SCT DCS structure (framed area) - BE hierarchical levels and principle FE units. The SCT supervisor is the PS projects, in the present implementation.

11.2.5 Finite State Machine (FSM)

The FSM interconnects and supervises all DCS projects. One FSM branch is installed and running in each PVSS project, all of them being accessed, supervised and summarized, in the present implementation, by the PS FSM. The state of each project gives information about the current running condition of the project. A project can be in three different states: READY, NOT READY and ERROR, with bi-directional transitions between them, apart from the transition READY to ERROR. If a project is in the state READY, it can provide reliable information about the status of the system, which can be OK, ALARM, WARNING and NOT PHYSICAL. The states and status are summarized in the FSM of each project and propagated to the upper levels of the DCS hierarchy. The safety and reliability requirements during operation, as well as the experience obtained during the system tests and the module assembly, determined the definition of the DCS alarms as well

as the corresponding actions to be taken in such cases. Table 11.2 summarizes the alarm definitions and the corresponding actions.

Case of	Action
$T_{cool} < T_{Dewpoint} + 10°C$	Flush dry air
$T_{cool} < T_{Dewpoint} + 5°C$	Switch off LV/HV
$T_{air} > 30°C$	Switch off LV/HV
$T_{mech} < -10°C \mid\mid T_{mech} > 30°C$	Switch off LV/HV
$I_{bias} > I_{alarm}$	Switch off HV
$T_{module} > T_{alarm}$	Switch off LV/HV
Off state HV> 20 V	Switch off HV
Off state LV output ON	Switch off LV
CC/HV/LV communication loss	Reset Communication
Any Fatal from Cooling and CIC	Switch off LV/HV prevent from ramping on.
Communication loss between projects	Pop up messages operator to reestablish communication. Interlock to ensure safety.

Table 11.2: Alarm definitions and corresponding actions.

11.3 DCS tests during the SCT assembly

The DCS functionalities have been tested and used at several SCT assembly sites. The performance of the DCS system has been checked for the PS project. In the case of a problem, such as an increase in hybrid temperatures indicative of a problem with the cooling system, it is desired to ramp down the power within 10 seconds. The CC will take at most 6 seconds after each readout to initiate a controlled shutdown of a problematic channel, hence the time interval between two successive readouts is set to 4 seconds such that shutdown takes place within the allowed time. In each readout about 1500 messages are transported through the CANbus and is has been measured that these messages are separated in the CANbus by a time interval of 0.9 ms. According to the ATLAS DCS requirements, the maximum CANbus occupancy during operation should not be larger than 60%, to prevent situations of overloaded CANbus in cases of emergency. Therefore, a maximum of 11 crates on each CANbus is allowed, when reading out every 4 seconds. Ethernet communication is used between the different DCS projects. Therefore, the alarm messages sent to the PS project by the other projects are received immediately.

11.3.1 SCT DCS in the ATLAS Combined Test Beam

A DCS chain including Environmental and Power Supply systems was set up for the ATLAS SCT test beam. Two temperature sensors on the cooling pipe, two air temperature sensors and two humidity sensors were monitored successfully by a simplified environmental project. Eight silicon modules were powered by a crate that was controlled and monitored by the PS project. The dependence of the leakage current as a function of the bias voltage (IV curve) for one silicon module using data from the PS project is shown in Figure 11.8.

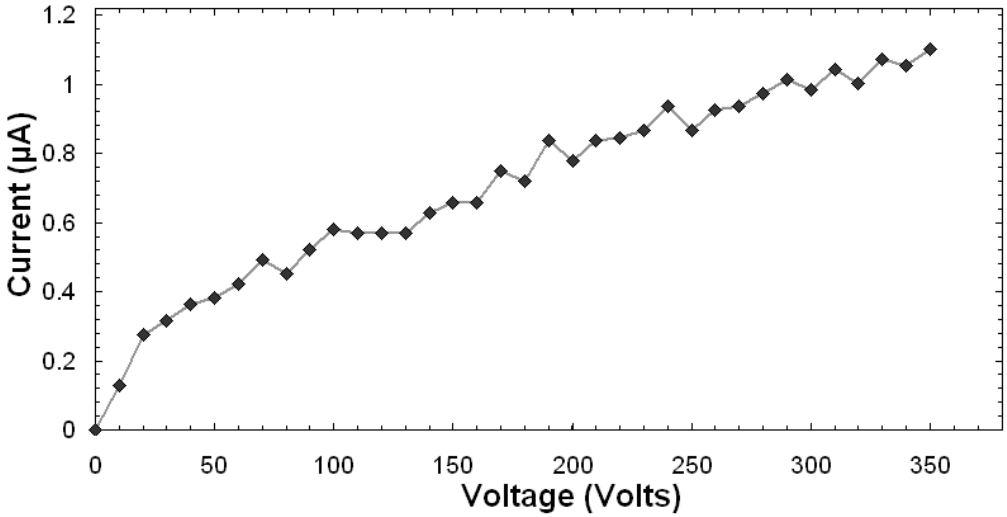

Figure 11.8: IV curves of one module used in the ATLAS SCT test beam, with data taken by the PS project. The intrinsic precision in the HV cards for the current readout is 50 nA corresponding to 5 ADC counts.

11.3.2 DCS Tests during Barrel Assembly

At the SCT assembly sites, acceptance tests with working DAQ and DCS systems are being performed. At Oxford University, the assembly of the innermost barrel layer has been completed. All DCS functionalities, as well as the DDC, have been tested and verified to work satisfying the safety requirements. DCS data have been stored using both the PVSS and the DAQ archiving tools, propagated through the DDC. Figure 11.9 shows the distribution of the module temperature along a cooling stave, for a cold run (coolant temperature $\approx 2°C$) and a warm run (coolant temperature $\approx 15°C$). The temperatures of the 24 modules are stable along a cooling stave.

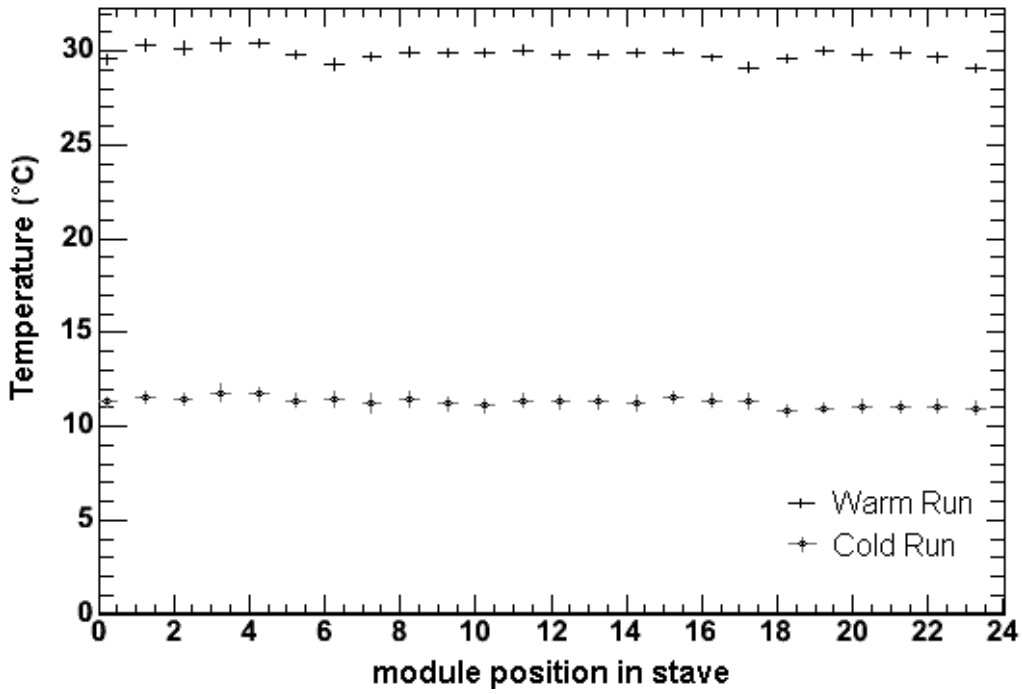

Figure 11.9: Temperature profile along a cooling stave. For the warm run, the mean temperature is 30.1°C, (RMS variation 1.0°C) and for the cold run the mean temperature is 11.6°C (RMS variation 1.5°C).

11.3.3 DCS and Performance Tests during the SCT Integration Phase

The final SCT assembly site was at CERN, where a dedicated facility, the so-called *SR-1 area*, for the Inner Detector assembly and integration was prepared.

Barrel sector testing

A barrel sector with 15 modules was initially tested. The stability of all the DCS projects could be verified, using a full DCS chain running continuously for several days. The PS DCS was successfully ramping on and off the power supplies and provides stable monitoring of the module currents (Figure 11.10). The evaporative cooling was functioning correctly. In Figure 11.11, the thermal enclosure temperatures as well as the temperatures in the outlet of the cooling stave are shown for one run of the barrel. The cooling procedure is shown: the temperature falls from $\approx 24°C$ to $\approx 12°C$, and even after the modules are powered, the temperature remains practically stable; at the end of the run the temperature of the cooling pipes

rises again to the room temperature. A successful monitoring of the main PS DCS parameters is also provided by the DAQ GUI, through the DDC. Summary panels show the module temperatures, as well as the analogue and digital voltages and currents.

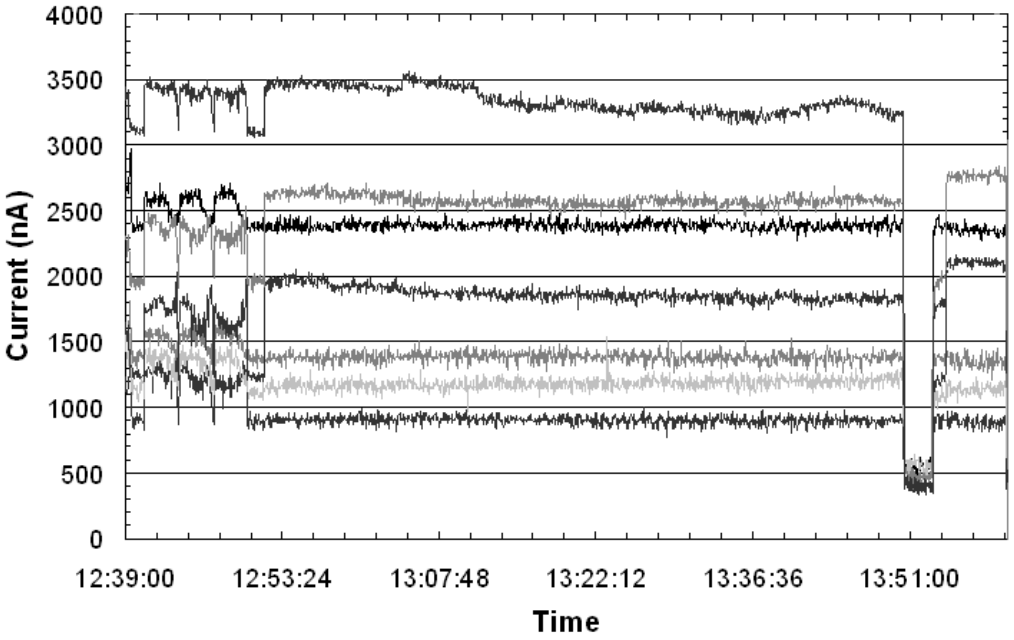

Figure 11.10: Current readouts for 7 modules, during a run of the barrel sector. The monitoring of the currents is stable. Current fluctuations are recorded, according to the operations performed by the DAQ.

Acceptance tests and performance

Acceptance tests have been performed on the barrels uppon arrival at CERN, at the *SR-1* area. Module cooling, power supplies and readout (analog and digital) have be checked. The goal of these tests is to verify that each barrel functions properly after transportation and before final four-barrel assembly. For these tests, approximately 700 cables and 2400 fibers had been tested and installed inside the temporary thermal enclosure [80].

In the CERN assembly facility, for single barrel acceptance tests up to 15 PS crates have be used simultaneously, while for full barrel tests, 44 crates have been fully occupied. The number of barrel environmental sensors to be monitored is shown in Table 11.3. Extensive tests have proven the stable running of the DCS components but also the good performance of the SCT barrel modules.

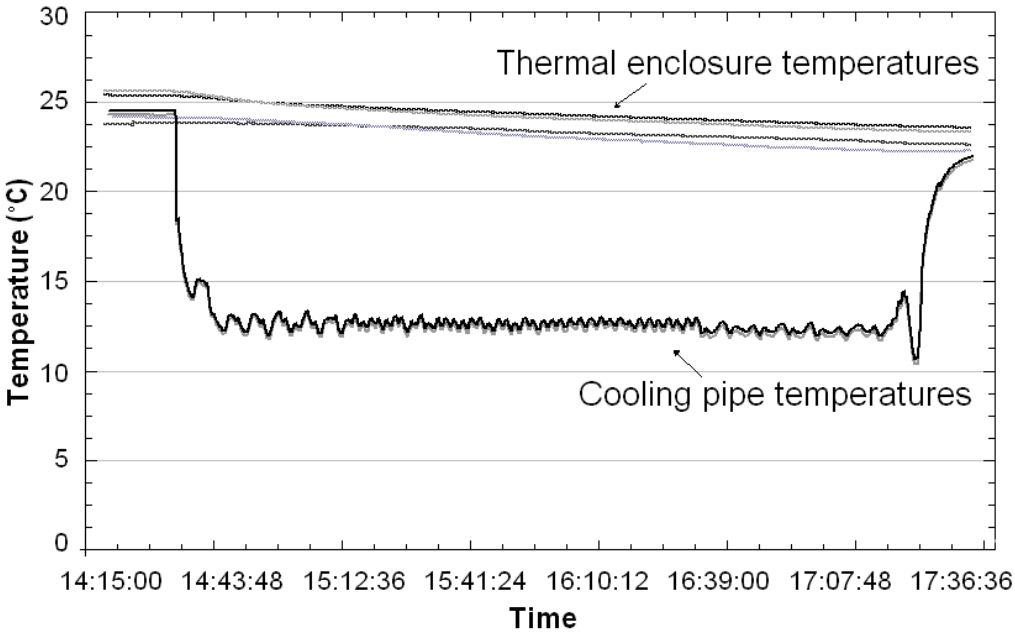

Figure 11.11: Temperature readout during a barrel sector run. Temporal evolution of the temperatures on cooling pipes and thermal enclosure temperatures are shown.

SCT Component	Cooling Temp	Mech Temp	Air Temp	Humidity	Total
Barrel 3	36	9	32	3	80
Barrel 4	46	9	32	4	91
Barrel 5	52	9	32	4	101
Barrel 6	60	9	32	4	111
Total Barrel	192	36	128	15	371

Table 11.3: Number of environmental sensors in the barrels.

Humidity, air temperature and mechanical structure temperature behavior

Monitoring of the environmental conditions around the detector is of prime importance for the avoidance of condensation and electronic breakdown of both silicon sensors and electronics.

During the SCT assembly the humidity was monitored both in the test enclusure, by non-radiation hard humidity sensors and the the radiation hard Xeritron sensors mount on the SCT mechanical structure. The Xeritron sensors show a much slower response to changes of the humidity, with respect to the sensors on the enclosure.

Figure 11.12 shows the humidity trend recorded by the Xeritron sensors after dry air was flushed inside the thermal enclosure. The response to increasing humidity, as can be seen from the same Figure, is very good. The sensors show a small temperature dependence; the dips in the curves of Figure 11.12 correspond to the changes in temperatures of the SCT induced by turning the power on or off or by clocking the modules.

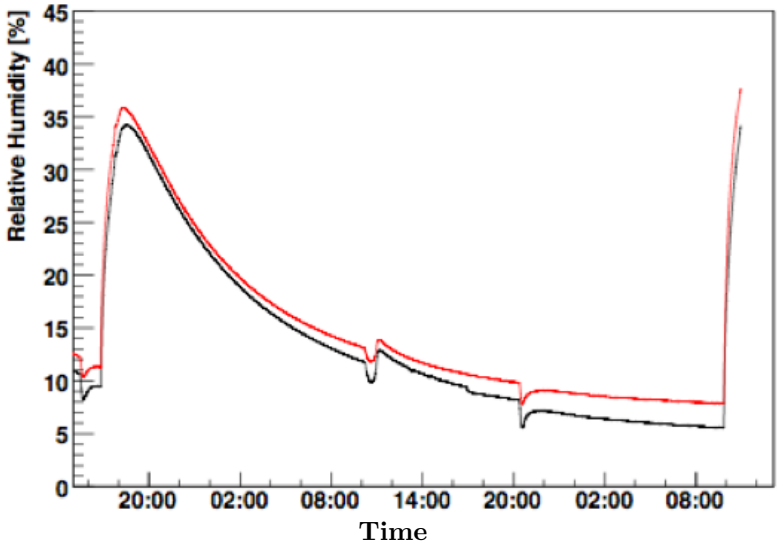

Figure 11.12: Relative humidity readings form the two Xeritron sensors mount on the detector structure, during reception testing of the Barrel 3.

The mechanical structure temperature and the air temperature close to the barrels were monitored with the NTC sensors mounted on the barrel structure. The enviromental temperatures have been rising when the module power was ramped up and were decreasing when the power was ramped down. The air temperatures showed a larger fluctuation with respect to the mechanical temperatures, which had a stable behaviour within a $5°C$ margin.

Cooling pipe temperatures behaviour

During a cooling cycle the most visible variations were noticed in the cooling pipe temperatures, as these are more closely related to the modules. Figure 11.13 shows all the environmental cooling pipe temperatures on barrel 3 as measured by the environmental project during a reception testing at CERN (April 7th, 2005). One

should notice that the temperature of the cooling pipes during these tests is $\approx 14°C$, that is a temperature much higher than the aimed operational temparature of the SCT ($-7°C$). The full cooling cycle is visible with the start up of the cooling, followed by the ramping up of the modules power and the inverse sequence for the end of run. At around 17h00, one can notice a small dip for all sensors. This corresponds to a change in back pressure settings on all pipes connected to this barrel. The individual sensors show an acceptable level of stability throughout the whole run and the spread of the temperatures is low.

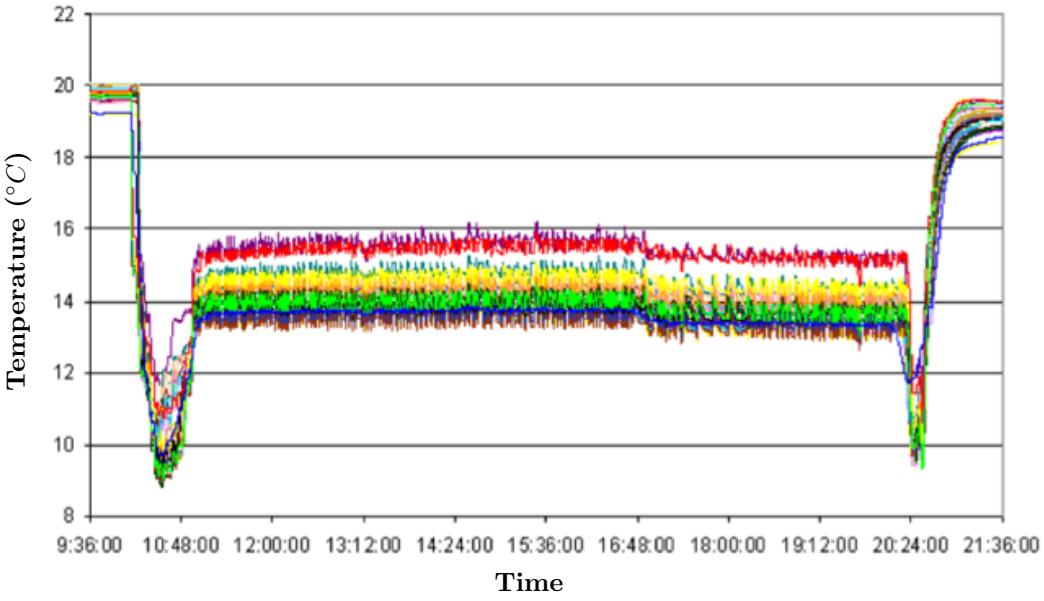

Figure 11.13: Evaporative cooling cycle as measured by the environmental cooling pipe temperature sensors on Barrel 3.

Module temperature and noise behavior

The performance of the SCT barrel modules has been tested during the barrel acceptance tests. The good thermal and electrical behavior has been verified with various tests.

Figure 11.14 shows the temperature of the modules along a barrel 3 cooling stave during acceptance tests performed on April 7th, 2005 . Module 0 is always the first module after the inlet and Module 23 is the last before the outlet. In the plot, the profile of the temperature variations along the cooling stave is shown.

Fitting the trend with a first degree polynomial, one can see that the temperature increases along the cooling stave. This is an expected effect, since the evaporative cooling tuning is not performing in an optimal way in "warm" operation (cooling pipe temperatures much higher than the SCT aim operational temperatures).

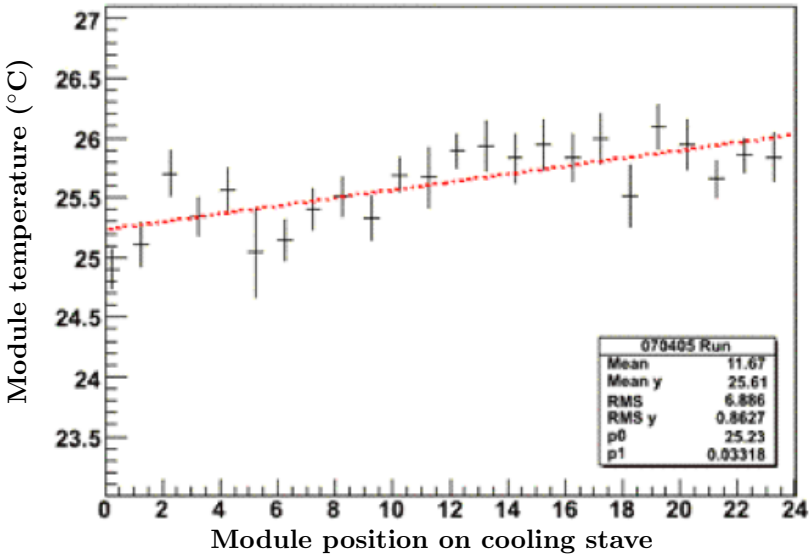

Figure 11.14: Hybrid temperatures along a cooling stave (24 modules from inlet to outlet).

The modules are found to have a good uniformity of temperatures around the barrel [81].

The noise measured in the modules when biased is expected to be highly correlated with the temperature. Plotting the ENC noise of the module along the cooling pipe (Figure 11.15) we observe a trend that follows the temperature variations.

It is interesting to see the variations of the noise per chip, in the module; the chips in the edges have lower noise than the chips on the middle, due to cross-talk. This effect seems to be give bigger variations in the ENC noise than the temperature variations (Figure 11.16).

11.4 Current Status

The status of the SCT as of February 2008 is summarized in this section.

The SCT barrels have been fully integrated and inserted within the TRT. Testing

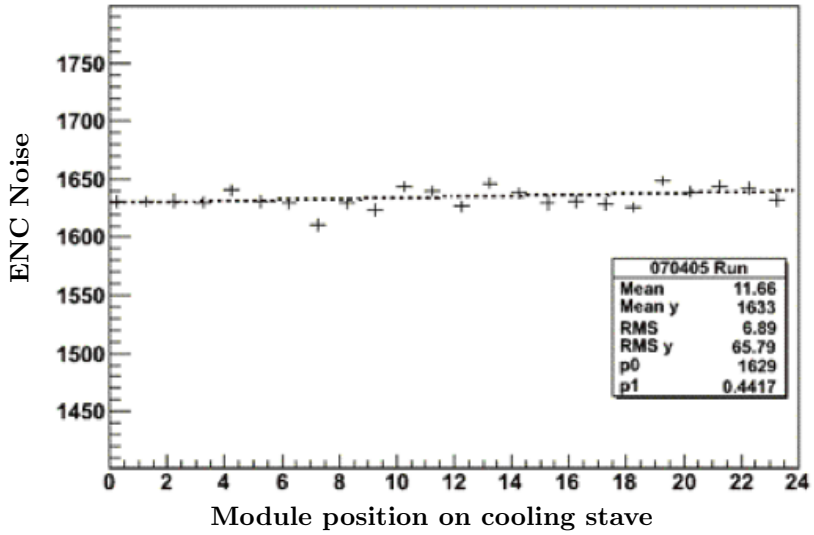

Figure 11.15: Mean hybrid ENC noise along a cooling stave (24 modules from inlet to outlet).

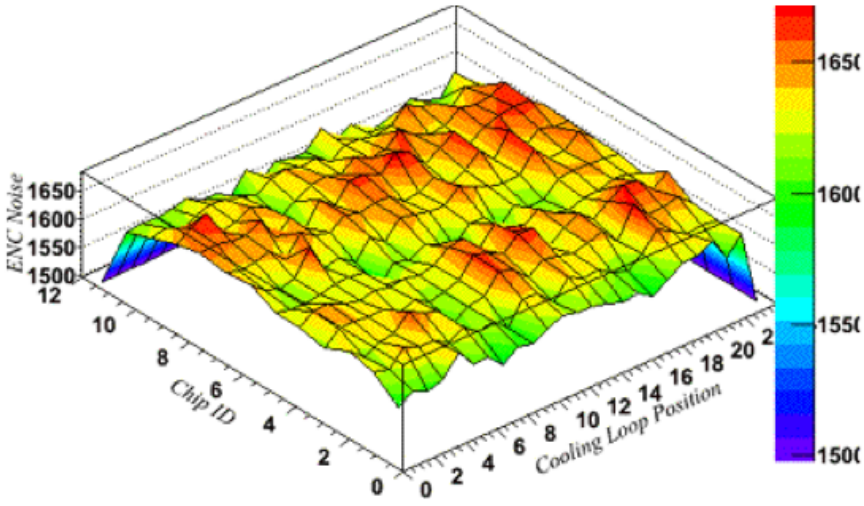

Figure 11.16: Mean hybrid ENC noise along the cooling pipe position and the chip posiiton. The chips that are placed in the middle of the hybrid - chips 2 and 3 for link 0 (module upper side) and chips 8 and 9 for link 1 (module lower side).

of the TRT and SCT integrated barrel system has taken place in the *SR-1* area and the barrels have been lowered in the ATLAS collision area.

For the SCT barrels in their final position, the environmental monitoring measure 735 temperature and humidity sensors across the detector. The monitored cooling pipe temperatures trigger the hardware interlock, protecting the SCT modules if a cooling problem occurs.

The SCT barrel modules and the DCS system have been extensively tested and their performance is verified to fulfill the requirements. The final DCS system is an extension of the DCS system used for the assembly phase. Therefore, the experience gained during the SCT reception tests has been of prime importance for a reliable and fast final DCS system design, that will ensure the safe operation of the detector during data taking.

11.5 Summary

The complexity and fragility of the SCT detector and its infrastructure demand an extremely stable DCS that will ensure the safe operation of the silicon modules. The software and hardware components of the SCT DCS building blocks (the power supplies, the cooling and the environmental systems) for the SCT commissioning phase have been prepared and tested. The DCS satisfied the required performance and the safety specifications and has been successfully extended into the final operational DCS system for the SCT detector.

Bibliography

[1] http://particleadventure.org/other/history/smt.html.

[2] *Review of Particle Physics*, W.-M.Yao et al, Journal of Physics G 33. 1 (2006).

[3] *Quarks and Leptons: An introductory Course in Modern Particle Physics*, F. Halzen and A.D. Martin, Wiley Editions.

[4] *Electroweak Interactions, An Introduction to the Physics of Quarks and Leptons*, Peter Renton, Cambridge University Press.

[5] *An update on vector boson pair production at hadron colliders*, J.M. Campbell and R.K. Ellis, Theory Department, Fermilab, hep-ph/9905386, May 1999.

[6] *Low energy effects of new interactions in the electroweak boson sector*, K. Hagiwara et al., Physical Review D, Vol.48, Num.5, 1 September 1993.

[7] *Study of Trilinear Gauge-Boson Couplings at the Tevatron Collider*, John Ellison and Jose Wudka, Annu. Rev. Nucl. Part. Sci. 1998. 48:33-80.

[8] M. Neubauer, for the CDF and D0 Collaborations, arXiv:hep-ex/0605066v2, 2006.

[9] Measurement of WZ Production in $WZ \to \ell\ell\ell\nu$ using 2 fb^{-1} of $p\bar{p}$ Collisions at $\sqrt{s} = 1.96$ TeV, public web-page, Shih-Chieh Hsu, Elliot Lipeles, Mark Neubauer, Matt Norman, Rami Vanguri, Frank Wurthwein.

[10] *Diboson physics at CDF*, A. Sfyrla [CDF Run II Collaboration], FERMILAB-CONF-07-548-E(2007), *Presented at International Europhysics Conference on High Energy Physics (EPS-HEP2007), Manchester, England, 19-25 Jul 2007.*

[11] *Limits on Amomalous Triple Gauge Couplings in* $p\bar{p}$ *Collisions at* $\sqrt{s} = 1.96$ *TeV*, arXiv:0705.2247v2 [hep-ex] 31 Aug 2007.

[12] *A Combination of Preliminary Electroweak Measurements and Constraints on the Standard Model*, The LEP COllaborations, hep-ex/0511027.

[13] Run II Handbook, Fermilab Beams Division.

[14] Rookie Books, Fermilab Beams Division:
http://www-bdnew.fnal.gov/operations/rookie_books/rbooks.html

[15] The Linac Rookie Book, v2.1 (June 13, 2006):
http://www-bdnew.fnal.gov/operations/rookie_books/LINAC_v2.pdf

[16] The Booster Rookie Book, v3.1 (June 26, 2006):
http://www-bdnew.fnal.gov/operations/rookie_books/Booster_V3_1.pdf

[17] The Main Injector Rookie Book, v1.0 (September 29, 2006):
http://www-bdnew.fnal.gov/operations/rookie_books/Main_Injector_v1.pdf

[18] The Antiproton Source, v1.1 (July 14, 2006):
http://www-bdnew.fnal.gov/operations/rookie_books/Pbar_V1_1.pdf

[19] The CDF II Detector Technical Design Report, The CDF Collaboration, FERMILAB-Pub-96/390-E.

[20] *The CDF Run II Luminosity monitor*, D. Acosta et al., Nucl. Instrum. and Methods A461, 540 (2001).

[21] CDF Note 7446, *Luminosity Uncertainty for Run 2 up until August 2004*, S. Jindiarini et al., 2005.

[22] CDF Note 2038, *Conceptual Design of a Deadtimeless Trigger for the CDF Trigger Upgrade*, H. Frisch et al., Univ. of Chicago, M. Campbell, Univ. of Michigan.

[23] CDF Note 6992, *The COT Pattern Recognition Algorithm and Offline Code*, Chris Hays et al.

[24] *Determination of the Jet Energy Scale at the Collider Detector at Fermilab*, A. Bhatti et al., Nucl.Instrum.Meth. A566(2006) 375-412, arXiv:hep-ex/0510047v1.

[25] *Generic Jet Energy Corrections at CDF*, Jet Energy and Corrections Public Web Page, Conveners: Monica D'Onofrio, Kenichi Hatakeyama, Andrew Mehta.

[26] CDF Note 8100, *Limits on the $WW + WZ$ boson decaying to lepton, $\not\!\!E_T$ plus jets at Run II using* $350/pb$, J.Sjolin, Oxford University.

[27] *Measurement of the W+jet cross section at CDF*, Andrea Messina, proceeding of the 36th International Symposium on Multiparticle Dynamics (ISMD 2006).

[28] CDF Note 6681, *Measurements of sigma* B(W→enu), sigma * B(Z→ee) and the ratio R using CDF Run II Data*, D.Amidei et al.

[29] CDF Note 6711, *Measurements of sigma* B(W→ μν), sigma * B(Z→ μμ) and the ratio R using CDF Run II Data*, D.Amidei et al.

[30] CDF Note 8614, *Electron ID Efficiency and Scale Factors for Winter 2007 Analyses*, D. Hare, E. Halkiadakis, T. Spreitzer.

[31] CDF Note 7939, *Trigger Efficiencies for the High ET Central Electrons in Gen6*, Veronique Boisvert.

[32] CDF Note 6866 *Determination of the Run II COT Tracking Efficiency using the W-No-Track Sample*, J.Thom et al.

[33] CDF Note 8010 *COT Tracking Efficiency*, Jonathan Efron, Julia Thom.

[34] CDF Note 6636, *QCD background estimation to $W \rightarrow e\nu + jets$ events*, A.Messina, S.Sarkar, INFN, Rome.

[35] CDF Note 8538, *Lepton ID for Multilepton Diboson Analyses*, E.Lipeles, M.Neubauer, S.C.Hsu, F.Wurthwein, University of California, San Diego.

[36] *PYTHIA 6.4, Physics and Manual*, T. Sjostrand, S. Mrenna and P. Skands, hep-ph/0603175.

[37] http://projects.hepforge.org/pythia6/.

[38] ALPGEN webpage:
http://mlm.home.cern.ch/mlm/alpgen/

[39] *ALPGEN, a generator for hard multiparton processes in hadronic collisions*, M. Mangano et al., hep-ph/0206293.

[40] CDF statistics committee webpage:
http://www-cdf.fnal.gov/physics/statistics/recommendations/selection.html

[41] JETNET 3.0:
http://www.thep.lu.se/public_html/jetnet_30_manual/jetnet_30_manual.html

[42] CDF Note 5434, *A Root Interface to JETNET*, C. Ciobanu et al., The Ohio State University.

[43] *Statistical Data Analysis, Chapter 9.3: Confidence interval for a Gaussian distributed estimator*, Glen Cowan, Oxford Science Publications.

[44] *What is systematics?*, Giovanni Punzi, February 9, 2001.

[45] CDF Note 7856, *Jet Energy Resolution*, F. Canelli, K. Hatakeyama, J. Adelman, E. Brubaker, 2005.

[46] Joint Physics ISR/FSR Uncertainties webpage:
http://www-cdf.fnal.gov/internal/physics/joint_physics/agenda/20050527-minutes.html

[47] CDF Note 8564, *Calibration of H1 Algorithm Improved Jet*, Andrew Mehta, 19 October 2006.

[48] *Top Mass Measurement at CMS*, Markus Duda, presented at the "Physics at LHC" Conference, Krakow, Poland, July 3-8, 2006.

[49] *Gluon-induced WW background to Higgs boson searches at the LHC*, arXiv:hep-ph/0503094v1, 10 Mar 2005.

[50] *Hard Interactions of Quarks and Gluons: a Primer for LHC Physics*, arXiv:hep-ph/0611148v1, 10 Nov 2006.

[51] ATLAS Detector and Physics Performance Technical Design Report LHCC 99-14/15.

[52] *The ATLAS Experiment at the CERN Large Hadron Collider*, ATLAS Collaboration, to be published in JINST.

[53] *Detector Challenges at the LHC*, Steinar Stapnes, Nature Insight, Reprinted of Vol. 448, No 7151, 19 July 2007.

[54] *The ATLAS semiconductor tracker end-cap module*, A. Abdesselam *et al.* [ATLAS Collaboration], Nucl. Instrum. Meth. A **575** (2007) 353.

[55] *Semiconductor Detectors for Particle Physics*, T.J.V. Bowcock, University of Liverpool (Notes from graduate slectures at EPFL):
http://hep.ph.liv.ac.uk/ tjvb/notes26.pdf

[56] *Semiconductor Devices*, S.M. Sze, J.M.Wiley.

[57] *Irradiation of ATLAS SCT Modules and Detectors in 2002*, P.J. Dervan et al., ATLAS Internal Note, ATL-INDET-2003-001.

[58] *ATLAS Inner Detector Technical Design Report*, ATLAS Inner Detector Community, CERN/LHCC/97-17, April 1997.

[59] *Design and performance of the ABCD3TA ASIC for readout of silicon strip detectors in the ATLAS semiconductor tracker*, F. Campabadal et al., Nucl. Instrum. Meth. A552:292-328, 2005.

[60] *Endcap Module Production for the ATLAS Silicon Tracker (SCT) at CERN and the University of Geneva*, M. Chamizo Llatas et al., DPNC, University of Geneva and PH Department, CERN, ATL-INDET-PUB-2006-006(2006).

[61] S. Moed's Ph.D. Thesis, 2007:
http://dpnc.unige.ch/THESE_MOED.ps

[62] *The Detector Control System For The Atlas Semiconductor Tracker Assembly Phase*, A. Sfyrla et al., IEEE Trans. Nucl. Sci. 52, 938 (2005).

[63] H. Boterenbrood et al., Design and Implementation of the ATLAS Detector Control System, IEEE Trans. Nucl. Sci., vol. 51, issue 3, pp. 495-501, June 2004.

[64] Joint Controls Project:
http://itco.web.cern.ch/itco/Projects-Services/JCOP/

[65] PVSS II (Prozessvisualisierungs- und Steuerungs-System), ETM, Austria:
http://www.pvss.com/

[66] C. Gaspar, Partitioning, Automation and Error Recovery in the Control and Monitoring System of an LHC Experiment, Proceedings of the International

Conference on Computing in High Energy and Nuclear Physics, September 2001, Beijing, P.R.China

[67] B. Hallgren et al., The Embedded Local Monitor Board (ELMB) in the LHC Front-end I/O Control System., presented at the 7th Workshop on Electronics for LHC Experiments, Stockholm, Sweden, September 10-14, 2001.

[68] CAN bus system:
http://www.can-cia.org/

[69] The KVASER CAN interface is the chosen product:
http://www.kvaser.com/

[70] OPC Foundation:
http://www.opcfoundation.org/

[71] A. Abdesselam et al., The Detector Control System of the ATLAS SemiConductor Tracker during Macro-Assembly and Integration, JINST A88 (2007) 888 [NOT YET PUBLISHED].

[72] M. Olcese et al., Inner Detector Evaporative Cooling System, ATLAS Internal Note, ATLAS-IC-ES-0006.

[73] J. Stastny, SCT LV3 Card Manual, ATLAS Note, ATL-INDET-2004-005.

[74] E. Gornicki, S. Koperny, SCT High Voltage Power Supply, ATLAS Internal Note, ATL-IS-ES-0084.

[75] R. Brenner et al., Evaluation of radiation hard humidity probes, submitted to the Journal of Testing and Evaluation.

[76] P. Kind et al., Pixel PP3 Patch Panels Design, ATLAS Internal Note, ATL-IP-ES-0075.

[77] N. Bingefors, R. Brenner, ATLAS SCT DCS Interlock Matrix, ATLAS Internal Note, ATL-IS-EN-0029.

[78] Oracle Database:
http://www.oracle.com/database/index.html

[79] H Burckhart et al., Communication between Trigger/DAQ and DCS in ATLAS, presented at CHEP'01: COMPUTING IN HIGH ENERGY AND NUCLEAR PHYSICS, September 3 - 7, 2001, Beijing, China.

[80] Two ATLAS Internal Notes summarize the cable and fiber tests and results: ATL-IC-TP-0001 and ATL-IC-TP-0004.

[81] G. Viehhauser, B. Mikulc, A. Sfyrla and A. Robichaud-Veronneau, Temperature behavior and uniformity of the SCT barrels during assembly and reception testing, ATL-INDET-PUB-2006-00, 2006.

Acknowledgments

The work presented in this thesis would have not been possible without the help and support of many people.

First of all, I would like to thank my advisor, Allan Clark, for giving me the opportunity to do this Ph.D. working in two experiments and in two continents, and for allowing me to follow my interests for research in both ATLAS and CDF.

On ATLAS, I had the chance to work at CERN with the SR-1 crew. Many thanks go to Pamela Ferrari, who introduced me to the DCS community and to Heinz Pernegger for his guidance, advice and discussions. Thanks to Bettina Mikulec, it was nice and fun working with her! Many thanks go to all the people participating in the SCT integration for creating such a nice collaborative environment: Sofia Chouridou, Pepe Bernabeu, Dave Robinson, just to name some of them.

When I was not in the SR-1 building, I would mostly be in the Geneva clean room. I would like to thank Didier Ferrère, Marteen Weber and all the other students, postdocs and technicians who participated in the module production for creating a nice working environment that made the shift hours less unbearable!

I spent the last two years of my Ph.D. at Fermilab. These two years have been very hard and wonderful at the same time! CDF has been a very warm and welcoming environment. I would like to thank all the nice people I met in the CDF control room being a CO and an Ace, the people that keep CDF alive!

Working on my analysis, I met a very collaborative environment. Special thanks go to Elliot Lipeles and Mark Neubauer, for their great help, for patiently answering my questions and teaching me how to do a physics analysis. I thank Shih-Chieh Hsu for teaching me the CDF software and for his great help since the first days that I was at Fermilab. A lot of people helped me in various phases in my analysis, and I deeply thank them all: Chris Neu, for helping me understanding the software

and principles of the Neural Network I used; Monica d'Onofrio, for being always available for jets questions and advice; Tom Junk and Louis Lyons for their help in statistics issues; Peter Renton, the Electroweak conveners, Eva Halkiadakis and Eric James, Regis Lefevre, Bernd Stelzer, some of the people with whom I had very useful and fruitful discussions for various issues, while I was working on my analysis.

Working on the diamonds project was a great experience too! Many thanks to Rick Tesarek, for being a very good teacher and also to Ricardo Eusebi, Peter Dong and Rainer Wallny, for making the work within the diamonds group real fun!

I would like to thank the University of Geneva students and postdocs (Chiara Casella, Mauro Donega, Till Hoffman, Andrée Robichaud, Raphael Schroeter, Mario Campanelli) for creating a nice environment to work, even if I didn't directly work with them. I had the chance to share the Geneva house at Fermilab with some of them, and this was fun!

Many thanks also to Catherine, who helped me deal with all the bureaucratic nightmare while being in Geneva but more importantly when I was at Fermilab.

I can't omit thanking my friends for making the last four years being from the best years of my life! Dimitris, my good friend in Athens and now in Geneva; Bianca and her owner (and the *vieux du Salève*); Niels and the hiking friends, with whom I shared great weekends in the mountains around Geneva; Giuseppe, Paolo and the CDF italian family that adopted me with love and the *Roma house* (aka *Paolo's*) for hosting it; GDL (*sweetie!*), always full of energy and charm; himself, Ilija, Emily, the Chicagoan lab-rats, that reminded us the existence of this great city; Roberto, always up for a run or a nice discussion; the two greeks at CDF, Giannis and Giorgos; Khaldoun, with the hope that soon we'll have a coffee not at midnight and not in B0; the running friends at Fermilab; I hope my life will always be full of such nice people surrounding me!

Last but not least, I would like to thank GP, for his great patience, for having done my Fermilab life smiley, and for keeping on doing it more smiley! Grazie! :-)

I owe what I have achieved thus far in my life to my mother and my sister. There are no words to express how I feel about them and no words to thank them, so I dedicate this thesis to them!